HAL open science

Quantification and characterization of epicardial adipose tissue in MRI

Pierre Daudé

▶ To cite this version:

Pierre Daudé. Quantification and characterization of epicardial adipose tissue in MRI. Medical Imaging. Aix Marseille Université (AMU), Marseille, FRA., 2022. English. NNT : 2022AIXM0333 . tel-04026893

HAL Id: tel-04026893

https://theses.hal.science/tel-04026893

Submitted on 13 Mar 2023

HAL is a multi-disciplinary open access archive for the deposit and dissemination of scientific research documents, whether they are published or not. The documents may come from teaching and research institutions in France or abroad, or from public or private research centers.

L'archive ouverte pluridisciplinaire **HAL**, est destinée au dépôt et à la diffusion de documents scientifiques de niveau recherche, publiés ou non, émanant des établissements d'enseignement et de recherche français ou étrangers, des laboratoires publics ou privés.

Distributed under a Creative Commons Attribution - NonCommercial - NoDerivatives 4.0 International License

NNT/NL : 0000AIXM0000/000ED000

THÈSE DE DOCTORAT

Soutenue à Aix-Marseille Université
le 25 octobre 2022 par

Pierre Daudé

Quantification du tissu adipeux épicardique à haut champ par IRM-Dixon, pour le phénotypage de la cardiomyopathie diabétique

Discipline
Physique et sciences de la matière

Spécialité
Biophysique

École doctorale
ED 352 – PHYSIQUE ET SCIENCES DE LA MATIERE

Laboratoire/Partenaires de recherche
CRMBM, UMR CNRS 7339, Centre de Résonance Magnétique Biologique et Médicale, Marseille, France

Composition du jury

Freddy ODILLE — Rapporteur
IADI INSERM U1254, Université de Lorraine, Nancy, France

Dimitrios KARAMPINOS — Rapporteur
Department of Diagnostic and Interventional Radiology, Technical University of Munich, Munich, Germany

Bénédicte GABORIT — Examinatrice
C2VN, Aix-Marseille Univ, Marseille, France

Matthias STUBER — Président du jury
Center for Biomedical Imaging, Lausanne, Switzerland

Sylviane CONFORT-GOUNY — Directrice de thèse
CRMBM, Aix-Marseille Univ, Marseille, France

Stanislas RAPACCHI — Co-directeur de thèse
CRMBM, Aix-Marseille Univ, Marseille, France

CRMBM-CEMEREM UMR 7339

Affidavit

I, undersigned, Pierre Daudé, hereby declare that the work presented in this manuscript is my own work, carried out under the scientific direction of Sylviane Confort-Gouny and Stanislas Rapacchi, in accordance with the principles of honesty, integrity and responsibility inherent to the research mission. The research work and the writing of this manuscript have been carried out in compliance with both the French national charter for Research Integrity and the Aix-Marseille University charter on the fight against plagiarism.

This work has not been submitted previously either in this country or in another country in the same or in a similar version to any other examination body.

Place Marseille, date 8 juillet 2022

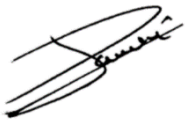

Cette œuvre est mise à disposition selon les termes de la Licence Creative Commons Attribution - Pas d'Utilisation Commerciale - Pas de Modification 4.0 International.

Liste de publications et participation aux conférences

- Liste des publications[1] réalisées dans le cadre du projet de thèse :

1. **Daudé P**, Ancel P, Confort Gouny S, Jacquier A, Kober F, Dutour A, et al. Deep-Learning Segmentation of Epicardial Adipose Tissue Using Four-Chamber Cardiac Magnetic Resonance Imaging. Diagnostics. 2022 Jan 6;12(1):126.
2. **Daudé P**, Roussel T, Viout P, Troalen T, Guye M, Kober F, et al. Comparative Review of Algorithms and Methods for proton-density fat fraction (PDFF) quantification. (in preparation for resubmission in Magnetic Resonance in Medicine)
3. **Daudé P**, Troalen T, Mackowiak ALC, Royer E, Piccini D, Yerly J, et al. Trajectory correction enables Free running cardiac Dixon for proton-density fat fraction quantification at 3T. (in preparation for submission in Journal of Cardiovascular Magnetic Resonance)

- Participation aux conférences[2] et écoles d'été au cours de la période de thèse :

1. **Daudé P**, Kober F, Confort-Gouny S, Bernard M, Rapacchi S. Comparative Review of Algorithm and Method for proton-density fat fraction (PDFF) quantification. In: Proceedings [Internet]. Virtual Meeting; 2021. p. Poster. (MRI Together : A global workshop on Open Science and Reproducible MR Research, December 2021). Available from: https://mritogether.github.io/files/abstracts/daude.pdf

[1] Cette liste comprend les articles publiés, les articles soumis à publication et les articles en préparation ainsi que les livres, chapitres de livre et/ou toutes formes de valorisation des résultats des travaux propres à la discipline du projet de thèse. La référence aux publications doit suivre les règles standards de bibliographie et doit être conforme à la charte des publications d'AMU.

[2] Le terme « conférence » est générique. Il désigne à la fois « conférence », « congrès », « workshop », « colloques », « rencontres nationales et/ou internationales » … etc.

Indiquer si vous avez fait une présentation orale ou sous forme de poster.

2. **Daudé P**, Ancel P, Confort-Gouny S, Gaborit B, Rapacchi S. Segmentation par deep learning du tissu adipeux épicardique sur ciné 4-chambres, comparaison avec son volume total,. In: Abstracts. Lyon; 2021. p. 60. (5e congres de la Société Française de Résonance Magnétique en Biologie et Médecine,Sept 27-29).

3. **Daudé P**, Ancel P, Confort-Gouny S, Dutour A, Gaborit B, Rapacchi S. Deep-Learning segmentation of epicardial fat using 4-chambers Cardiac MRI, comparison with total epicardial fat volume. In: Proceedings. Virtual Meeting; 2021. p. Poster. (2021 ISMRM & SMRT Annual Meeting & Exhibition,May 15-20).

4. **Daudé P**, Ancel P, Confort-Gouny S, Gaborit B, Rapacchi S. Deep-Learning segmentation of epicardial fat using 4-chambers Cardiac MRI, comparison with total epicardial fat volume. In: Proceedings. Virtual Meeting; 2021. p. Poster. (SCMR Virtual Scientific Sessions, Feb 17-20).

5. **Daudé P**, Troalen T, Mackowiak ALC, Piccini D, Yerly J, Pfeuffer J, et al. Trajectory correction enables Free running cardiac Dixon at 3T. In London, UK; 2022. p. Poster. (2022 ISMRM-ESMRMB & ISMRT 31st Annual Meeting, 07-12 May).

6. **Daudé P**, Kober F, Confort Gouny S, Bernard M, Rapacchi S. Comparative Review of Algorithms and Methods for proton-density fat fraction (PDFF) quantification. In London, UK; 2022. p. Oral. (2022 ISMRM-ESMRMB & ISMRT 31st Annual Meeting, 07-12 May).

Résumé

Un meilleur phénotypage des patients obèses ou diabétiques à risque pourrait éviter de nombreux décès dus aux complications cardiométaboliques. La graisse joue un rôle central dans les maladies métaboliques et sonder la graisse cardiaque suscite donc un intérêt croissant pour détecter et prévenir les complications cardiovasculaires. Plus précisément, le tissu adipeux épicardique (EAT), dépôt de graisse attaché au cœur, dont l'accumulation anormale a été liée à une augmentation du risque cardiovasculaire. Récemment, il a été montré que l'activité métabolique de l'EAT amplifie ou réduit la dégradation cardiovasculaire.

L'imagerie par résonance magnétique (IRM) cardiaque permet de visualiser l'EAT même sur un protocole standard, mais celui-ci a souvent été négligé ou même atténué. Inversement, l'objectif de cette thèse était de développer l'imagerie de l'EAT en IRM cardiaque afin de quantifier son accumulation et de caractériser ce tissu à l'aide de métriques innovantes.

Nous avons implémenté une segmentation automatique par apprentissage profond de l'accumulation de l'EAT sur des images cardiaques standards. Cet outil permettrait une détection rapide de la surcharge d'EAT chez les patients à risque et a montré une confiance de 71% pour le bon classement de cette quantité dans son quartile d'EAT.

Ensuite, nous avons développé l'imagerie eau-graisse pour analyser l'EAT grâce à la fraction de graisse en densité de proton (PDFF) et la vitesse de relaxation transversale effective (R_2*). Ces métriques permettent d'identifier la couleur caractéristique de la graisse (blanche, brune), renseignant ainsi sur son activité métabolique. Cependant, le mouvement cardio-respiratoire, l'accumulation rapide de phases entre la graisse et l'eau à haut champ (3T) sont autant d'obstacles à la mesure précise et hautement résolue de ces paramètres quantitatifs. Ainsi, l'ensemble du pipeline d'imagerie eau-graisse (également appelé Dixon) a été revu.

Les algorithmes Dixon estimant les cartes quantitatives PDFF et R_2* ont été comparés de façon standardisée grâce à une infrastructure programmé en deux languages. Cela a permis de sélectionner l'algorithme le plus fiable et précis qui s'est avéré être la méthode

IDEAL-CE (Iterative Decomposition of water and fat with Echo Asymmetry and Least square estimation with constrained extension).

Cette étude a aussi révélé que le mauvais calibrage du spectre de graisse multi-pics utilisé dans le modèle de Dixon induisait un biais de PDFF et R_2*. Dans une étude préliminaire, nous avons exploré la composition en acides gras d'échantillons ex-vivo d'EAT humains en utilisant la spectroscopie par résonance magnétique. Une fois cette étude terminée, un étalonnage plus fiable du spectre d'EAT pourrait être fourni pour l'imagerie eau-graisse.

Pour surmonter le mouvement cardio-respiratoire, le Free-Running, approche à haute résolution auto-navigués dans les cycles cardio-respiratoires, combinée à une reconstruction multidimensionnelle de type Compressed Sensing, a été adapté à l'imagerie eau-graisse multi-échos.

En multi-échos, le gradient bipolaire, plus efficace que le monopolaire, s'est révélé être très sensible à l'erreur de phase due aux imperfections spécifiques du système. La correction de la trajectoire dans l'espace k grâce à la fonction de réponse impulsionnelle du gradient a été intégrée pour en permettre son utilisation. Elle a permis de restaurer la qualité de l'image et d'obtenir une précision de PDFF de 1,23%.

En réunissant ces avancées techniques dans un pipeline complet de Dixon, une quantification précise et hautement résolue du PDFF et du R_2* a été obtenue. Ainsi, dans notre cohorte de sujets sains, l'EAT avait une fraction graisseuse plus faible (80,36±7,10%) que la graisse sous-cutanée (92,49±4,25%).

Cette thèse ouvre la voie à l'imagerie quantitative de l'EAT, se présentant comme un outil prometteur pour la caractérisation in-vivo de l'EAT afin de mieux comprendre son rôle dans les complications cardiovasculaires.

Mots clés : tissu adipeux épicardique, séparation eau/graisse, imagerie Free-Running Dixon, segmentation par apprentissage profond, spectre de graisse.

Abstract

In the last decades, our society has seen an increased prevalence of obesity and diabetes, linked with a rising concern for cardiometabolic complications. Fat is central in metabolic diseases and probing cardiac fat has thus received a growing interest to detect and prevent cardiovascular complications. Specifically, epicardial adipose tissue (EAT), fat depot attached to the heart, abnormal accumulation has been linked to an increase of cardiovascular risk. Recently, evidence also showed that depending on its metabolic activity could either amplify or reduce cardiovascular degradation.

Cardiac Magnetic Resonance Imaging (MRI) is up to quantify and characterize in-vivo EAT throughout its evolution. However, even if EAT is visible on standard cardiac MRI protocol, it has often been overlooked or even purposedly dimmed. Inversely, the aim of this thesis was to develop epicardial fat imaging in cardiac MRI to quantify its accumulation and characterize this tissue using innovative metrics.

We developed a rapid automatic segmentation of EAT overload on standard cardiac images. Using deep learning method, EAT area is quantified on four chamber cine acquired in clinical routine. This tool would provide a rapid detection of overload EAT in at-risk patient and showed a confidence of 71% to correctly classify it in its EAT quartile quantity.

When it is relevant, we aimed at proposing a specific acquisition to investigate more in depth this fat. Chemical shift imaging enables to characterize fat with Proton Density Fat Fraction (PDFF), biomarker of adiposity and effective transverse relaxation rate (R_2*) biomarker of iron overload. These metrics showed to identify color features of fat (white, brown), which informs about its metabolic activity. However, cardio-respiratory motion, rapid phase accrual between fat and water at high field strength (3T) are all obstacles for high-resolution and precise measurement of these quantitative parameters. Thus, the entire fat-water imaging (also called Dixon) pipeline has been reviewed to overcome these technical barriers.

First, fat-water signal separation algorithms that estimate PDFF and R_2* quantitative maps from acquired images were benchmarked using a bi-language toolbox. This standardized comparison helped to select the most reliable and precise algorithm which

proved to be the Iterative Decomposition of water and fat with Echo Asymmetry and Least square estimation method with constrained extension.

Second, it also revealed that the miscalibration of the a priori known multi-peaks fat spectrum used in the Dixon model induced PDFF and R_2* bias. Therefore, in a preliminary study, we explored the fatty acid composition of human EAT samples using ex-vivo Magnetic Resonance Spectroscopy. After completion of this study, a more reliable EAT spectrum calibration could be provided for fat-water imaging.

Third, to overcome cardio-respiratory motion, the Free-Running framework, a high-end approach for high-resolution cardiac imaging with fully cardio-respiratory self-gating, combined with a multidimensional Compressed Sensing reconstruction, was adapted for multi-echo fat-water imaging. However, the bipolar gradient multi-echo mode, more efficient than the monopolar mode, proved to be highly sensitive to phase error due to system-specific imperfections.

Fourth, the k-space trajectory correction using Gradient Impulse Response Function was integrated to enable bipolar readout gradient mode. It restored image quality and enabled a PDFF precision of 1.23%.

Finally, by bringing together those technical advancements in a complete Dixon pipeline, high resolution precise PDFF and R_2* quantification was achieved. Thus, in our healthy cohort, epicardial fat had a lower fat fraction (80.36±7.10%) than the subcutaneous fat (92.49±4.25%).

This thesis lays ground to EAT quantitative imaging, standing as a promising tool for in-vivo characterization of EAT to better understand its role in cardiovascular degradation.

Keywords : epicardial adipose tissue, water/fat imaging, Free-Running chemical shift Dixon imaging, deep learning segmentation, fat spectrum

Table of Contents

Affidavit **1**

Liste de publications et participation aux conférences **2**

Résumé **4**

Abstract **6**

Table of Contents **8**

Résumé détaillé **12**

A. Evaluation quantitative de l'accumulation de graisse épicardique sur des images de routine d'IRM cardiaque 15

B. Imagerie de précision de la graisses grâce à l'imagerie eau-graisse 18

C. Caractérisation ex vivo du TAE par RMN 22

D. Caractérisation in vivo du TAE par imagerie DIXON 24

Introduction **28**

Chapter 1 : Clinical and scientific context of epicardial adipose tissue **30**

1.1 Epicardial adipose tissue 30

1.1.1 Anatomy and Physiology 30

1.1.2 Epicardial fat composition 31

1.1.3 Role of epicardial adipose tissue in cardiovascular diseases 32

1.2 Epicardial fat characterization 33

1.2.1 Molecular and Cellular characteristics 33

1.2.2 Gas Chromatography 34

1.2.3 Magnetic Resonance Spectroscopy 36

1.3 Epicardial fat in Radiology 39

1.3.1 Epicardial fat quantification in cardiac MRI 39

1.3.2 Model-based water/fat separation by chemical shift imaging 41

1.3.3 Chemical-shift encoded imaging acquisition strategies 46

1.4 Artificial intelligence dedicated to epicardial fat segmentation 47

Chapter 2 : Quantitative evaluation of epicardial fat overload from routine cardiac MRI **50**

2.1 Synthesis 50

2.2 Introduction 53
2.3 Materials and Methods 55
2.3.1 Study Population 55
2.3.2 MRI acquisition 56
2.3.3 EAT segmentation 56
2.3.4 Network architecture 57
2.3.5 Training 58
2.3.6 Evaluation metrics 59
2.3.7 Statistical analysis 60
2.4 Results 60
2.5 Discussion 66
2.5.1 Four-chamber-view intrapericardial fat area is a relevant measure of EAT 66
2.5.2 A specific database with possible extensions 67
2.5.3 The challenge of EAT segmentation 68
2.5.4 Comparing FCNs performances 68
2.5.5 Performances across quartiles 69
2.6 Conclusions 69
2.7 Supportive Information 70
Chapter 3 : Fat precision imaging using CSE imaging 72
3.1 Synthesis 72
3.2 Introduction 76
3.1 Materials and Methods 77
3.1.1 Open-source algorithms 77
3.1.2 Algorithm standardization 78
3.1.3 Monte Carlo simulation 80
3.1.4 Acquisition parameter: echo spacing 80
3.1.5 Fat spectrum library 81
3.1.6 In vitro: fat-water phantom 81
3.1.7 In vivo imaging 82
3.1.8 Evaluation metrics and statistical analysis 83
3.2 Results 83
3.2.1 Numerical simulations 83

3.2.2 In vitro experiments 87
3.2.3 In vivo experiments 89
3.2.4 Influence of the spectrum model 90
3.3 Discussion 92
3.3.1 Open-source framework and reproducibility research 92
3.3.2 Numerical simulations 92
3.3.3 In vitro experiments 93
3.3.4 In vivo experiments 93
3.3.5 Influence of the spectrum model 94
3.3.6 Algorithms running time 94
3.3.7 Choices of open-source algorithms 94
3.3.8 Possible extensions and new challenges 95
3.4 Conclusions 95
3.5 Supportive Information 96
Chapter 4 : Ex Vivo EAT characterization using MRS 101
4.1 Synthesis 101
4.2 Introduction 103
4.3 Methods 103
4.3.1 Ex vivo Human samples 103
4.3.2 MR and MRS protocol 103
4.3.3 MRS data processing 104
4.4 Results 105
4.5 Discussion 108
4.6 Conclusions 108
Chapter 5 : In vivo EAT characterization using CSE imaging 110
5.1 Synthesis 110
5.2 Introduction 113
5.3 Materials and Methods 114
5.3.1 MRI acquisition 114
5.3.2 In vitro: fat water phantom 114
5.3.3 Numerical Simulation 115
5.3.4 Study Population 115
5.3.1 GIRF measurement 115

5.3.2 Image Reconstruction and Quantitative fat-water mapping 116
5.3.3 Evaluation metrics and statistical analysis 118
5.4 Results 118
5.4.1 GIRF measurement results 118
5.4.2 Echo spacing scheme 119
5.4.3 Numerical simulations 119
5.4.4 In-vitro experiments 122
5.4.1 In-vivo experiments 122
5.5 Discussion 127
5.6 Conclusions 129
General Conclusion and Discussion 130
Bibliography 135
List of Abbreviations and Symbols 156
List of Figures 159
List of Tables 164

Résumé détaillé

Au cours des dernières décennies, notre société a connu une prévalence accrue de l'obésité et du diabète, liée à une préoccupation croissante pour les complications cardio-métaboliques. La graisse joue un rôle central dans les maladies métaboliques et le sondage de la graisse cardiaque a donc reçu un intérêt croissant pour détecter et prévenir les complications cardiovasculaires. La communauté scientifique et clinique s'est intéressée plus particulièrement au tissu adipeux épicardique (EAT) qui est une graisse viscérale située entre le cœur et le péricarde, en contact direct avec le myocarde.

L'EAT a un rôle multifacette dans la physiologie cardiaque, prévenant de la lipotoxicité cardiaque, il sert à la fois de réservoir à énergie ou de thermorégulateur. Aussi l'EAT est dit "beige", phénotype intermédiaire entre les deux familles de graisses, graisses de stockage blanches et graisses de thermogénèse brunes ; la 'couleur' de l'EAT pouvant varier selon des facteurs génétiques ou environnementaux. Cependant, dans des conditions pathologiques, l'EAT passe d'un rôle cardio-protecteur à un substrat inflammatoire, favorisant le développement de maladies cardiovasculaires telles que la maladie coronarienne, la fibrillation atriale et l'insuffisance cardiaque.

Différentes modalités d'imagerie ont été identifiées pour quantifier la surcharge en EAT puisque son accumulation anormale a été liée à une augmentation du risque cardiovasculaire. L'échocardiographie transthoracique, modalité de premier plan en cardiologie, a été utilisée pour mesurer l'épaisseur de l'EAT sur la paroi du ventricule droit. Cependant, cette mesure seulement de distance a été utilisée pour estimer le volume de l'EAT ce qui limite fortement la précision de cette méthode car l'EAT est distribué de manière irrégulière autour du cœur. L'imagerie par tomodensitométrie (TDM) cardiaque est devenue la méthode d'imagerie de référence pour la quantification du volume de l'EAT. Dans des études plus récentes, des méthodes semi-automatiques et d'apprentissage profond ont été développées pour réaliser la segmentation de cette graisse. Cependant, l'exigence d'une TDM cardiaque à haute résolution spatiale a conduit à l'utilisation de doses élevées de rayonnements ionisants, ce qui pourrait constituer un risque pour le suivi longitudinal des patients.

L'imagerie par résonance magnétique (IRM) cardiaque est un outil polyvalent qui permet de mesurer la fonction cardiaque, la morphologie, la perfusion en un seul examen. Cette modalité est également très sensible à la graisse cardiaque mais son observation reste souvent négligée ou même volontairement atténuée puisque l'EAT a longtemps été considéré comme un obstacle à la visualisation du myocarde et des artères coronaires. Lors d'un protocole standard, le volume de l'EAT peut être mesuré à partir d'une pile d'images ciné orientées en petit axe et couvrant l'ensemble du cœur. Cependant cette quantification est effectuée manuellement, ce qui est une opération longue et fastidieuse. En effet, le péricarde qui sépare l'EAT de la graisse paracardique n'est pas clairement visible sur les coupes petit-axe. Il se réduit souvent à une fine ligne qui peut être floutée à cause d'effets de volume partiels, surtout à l'apex. Au contraire, sur les vues en 4 cavités (4Ch), le péricarde est généralement moins affecté par ces effets de volume partiels, ce qui en permet une meilleure visualisation. Au début de cette thèse, seulement deux méthodes de segmentation automatique, ou semi-automatique, de l'EAT sur l'IRM cardiaque ont été présentées lors de conférences. Cependant, les deux études ont été démontrées sur moins de 15 sujets chacune et ne sont basées que sur une seule image ciné n'exploitant pas l'information temporel utile à la visualisation du péricarde.

Pour sonder plus spécifiquement la graisse en IRM, on peut utiliser une technique d'acquisition dédiée appelé Dixon. Celle-ci exploite les différences de fréquences de précession de l'eau et de la graisse afin de les identifier à une haute résolution spatiale. Elle nécessite l'acquisition de plusieurs images à différents temps d'écho (TE), pour que les signaux de la graisse et de l'eau accumulent différentes valeurs de phase, en fonction de leurs fréquences de précession. Les images de l'eau et de la graisse sont ensuite séparées grâce à des algorithmes avancés qui utilisent un modèle bio-physique avec comme a priori la connaissance du spectre RMN de la graisse. La fraction graisseuse en densité de protons (PDFF), rapport entre les protons de la graisse sur les protons de l'eau et de la graisse indicateur d'adiposité ou la vitesse de relaxation transversale effective (R_2*) informant de la surcharge de fer sont des biomarqueurs quantitatifs issus de cette technique. La précision de ces mesures est essentielle pour une utilisation en clinique de ces paramètres. Cependant une grande diversité d'algorithmes les calculant est apparue cette dernière décennie. Le dernier benchmark pour en évaluer leurs performances, un défi international, date déjà de 10 ans, et était uniquement basé sur des images en in-vivo. L'IRM cardiaque DIXON est un défi en raison des mouvements cardiaques et respiratoires,

avec en plus à 3T, une accumulation rapide et concomitante de phase entre l'eau et la graisse. Ces verrous techniques en empêchent son utilisation en routine clinique. En recherche, l'IRM cardiaque DIXON a déjà été développée afin d'obtenir une imagerie haute résolution de l'EAT mais au prix d'une précision insuffisante pour la quantification du PDFF et du R_2*.

Le modèle DIXON nécessite une connaissance a priori de la nature des tissus graisseux. La chromatographie gazeuse est la technique de référence afin de connaitre la composition et le profile en acides gras composants les triglycérides du tissu adipeux (saturés (SFA), insaturés (UFA), monoinsaturés (MUFA), polyinsaturés (PUFA)). La chromatographie étant invasive, celle-ci est moins adaptée à une étude longitudinale en in-vivo. Comme alternative non invasive, des approches par spectroscopie par résonance magnétique (SRM) ont été utilisées pour la quantification de ces catégories d'acides gras dans divers tissues adipeux mais jamais sur l'EAT. En effet, les acides gras peuvent être estimés par résonance magnétique car chaque proton d'hydrogène de la molécule de triglycéride contribue au signal SRM, ou RMN. La position de ces protons au sein de la molécule de triglycéride donne lieu à différentes fréquences de résonance dans le spectre RMN. Le modèle de ce spectre RMN a été simplifié en décrivant l'amplitude théorique de chaque pic des triglycérides avec seulement trois paramètres : le nombre de doubles liaisons (ndb), le nombre de doubles liaisons interrompues par du méthylène (nmidb) et la longueur de la chaîne (cl). La connaissance du spectre RMN de l'EAT apporterait des connaissances précieuses sur la composition de l'EAT, tant pour la physiologie que pour l'imagerie par IRM-DIXON.

Cette thèse a donc pour but de développer l'imagerie de la graisse épicardique en IRM cardiaque et s'articule autour d'un double objectif : 1/ le développement d'une évaluation rapide de l'EAT sur des images IRM standards afin de promouvoir cette graisse comme un élément diagnostique dans les complications cardiovasculaires ; 2/développer l'IRM cardiaque DIXON afin de sonder plus en profondeur cette graisse en assurant une haute résolution d'imagerie tout en renforçant la précision des paramètres quantitatifs calculés.

A. Evaluation quantitative de l'accumulation de graisse épicardique sur des images de routine d'IRM cardiaque

Contexte et motivation

Ces dernières années, l'EAT est de plus en plus reconnu comme un biomarqueur du risque de complication cardiovasculaire dans de multiples pathologies, notamment dans le diabète et l'obésité. Cependant, en IRM cardiaque, sa caractérisation reste fastidieuse et impraticable en clinique en raison de la résolution spatiale limitée pour l'identifier. Par conséquent, les méthodes de quantification de l'EAT par IRM n'en sont encore qu'à leur début par rapport à l'imagerie par tomodensitométrie cardiaque où des approches automatiques basées sur l'apprentissage profond ont déjà été bien développées. Afin de réduire cette lacune et de faciliter l'analyse de l'EAT en IRM, cette étude propose une quantification automatique de l'aire de l'EAT en 4 cavités en utilisant des réseaux auto-encodeurs (AE) multi-phases en ciné.

Méthodes et résultats

Une base de données rétrospective mono-centrique de 100 sujets (comprenant des sujets sains, des patients diabétiques de type 2 et des patients obèses non diabétiques), qui ont fait un examen d'IRM cardiaque à 3T incluant des images multi-coupes petit axe et un plan axial 4 cavités, a permis d'évaluer la performance des réseaux AE et la corrélation entre le volume total d'EAT et son aire en 4 cavités. U-Net et le réseau AE développé par Bai (noté FCNB) ont été optimisés par validation croisée à 4 blocs (n=80) et évalués sur une base de données indépendantes (n=20).

Notre base de données a montré une corrélation modérée entre le volume d'EAT et l'aire en 4 cavités (r = 0,77 et 0,74 pour la phase systolique et diastolique respectivement). Sur les données test, la performance des réseaux était équivalente au biais inter-observateurs (pour l'EAT : DSC_{Inter} = 0,76, $DSC_{U\text{-}Net}$ = 0,77, DSC_{FCNB} = 0,76) comme le montre la **Figure 0-1**. U-Net était mieux adapté à l'estimation de l'aire de l'EAT comparé au FCNB.

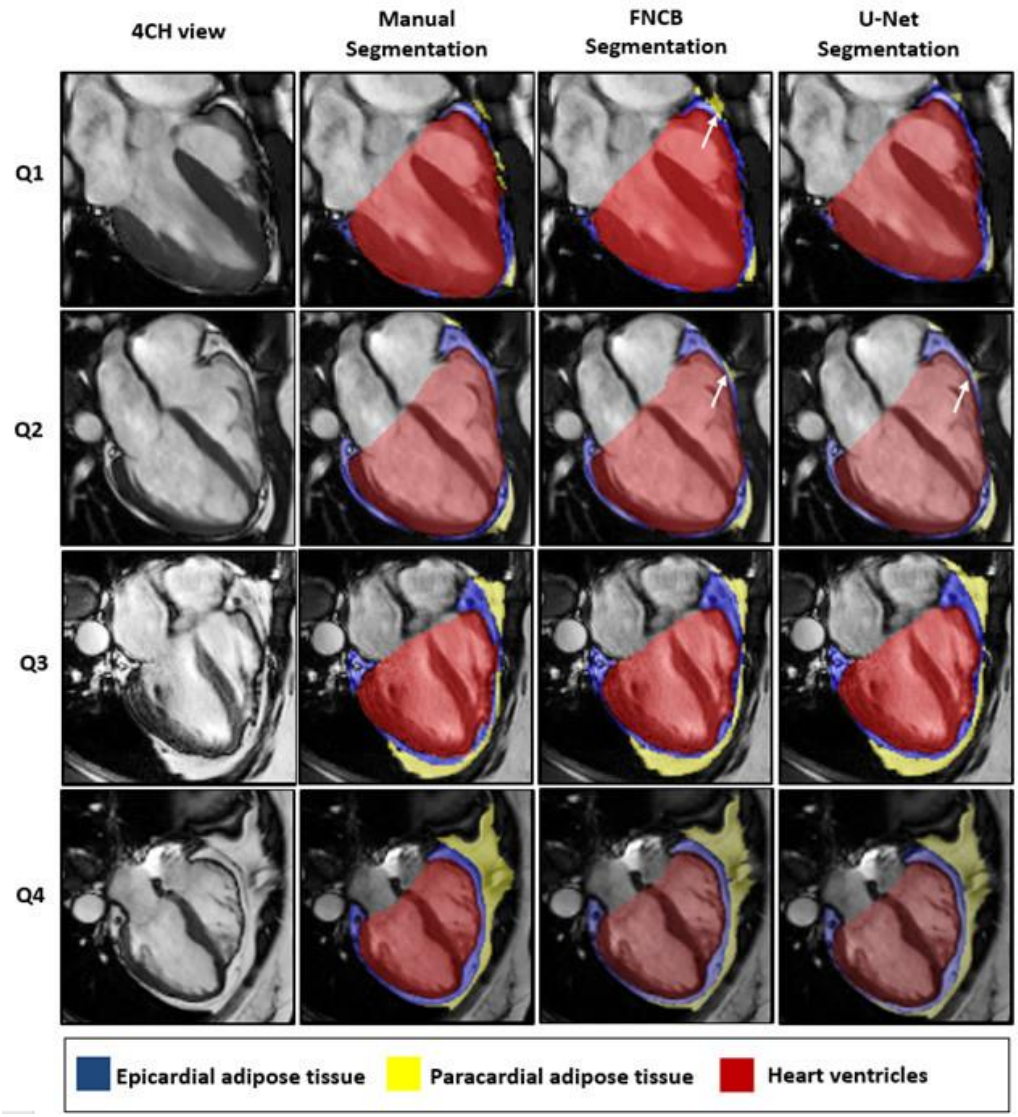

Figure 0-1 Résultats représentatifs de la segmentation pour chaque population définie par quartile d'EAT. Les flèches blanches indiquent les divergences entre les segmentations manuelle et automatique.

Conclusion, limites et perspectives

Ces travaux ont été acceptés comme article, s'intitulant Deep-Learning Segmentation of Epicardial Adipose Tissue Using Four-Chamber Cardiac Magnetic Resonance Imaging et publié dans Diagnostics le 29 décembre 2021. En plus de la publication, nous avons décidé de fournir une segmentation automatique open-source de l'aire de l'EAT qui offre la possibilité de l'évaluer quantitativement durant un protocole d'imagerie IRM cardiaque standard, permettant ainsi son investigation sur des études prospectives ou rétrospectives. Cependant, ces réseaux AE ont été entrainés et testés uniquement sur une base de données mono-centrique, ce qui a limité leur généralisation

à d'autres scanners et pathologies. De plus, ces approches ont montré des limites et l'aspect dynamique des images n'a pas été suffisamment exploité. Le développement de nouveaux types de réseaux AE basés sur des modules temporels tels que les « Convolutional Long Short Term Memory » (ConvLSTM) pourrait améliorer la précision de la segmentation automatique de cette graisse épicardique et être entraîné sur une base de données plus généralisée telle que la UK biobank. Afin de renforcer les modèles pour la routine clinique, l'augmentation des données basée sur des artefacts IRM réels et l'auto-évaluation automatique de la précision de ces réseaux via un score de qualité prédictif sont également des extensions importantes envisageable.

Après la détection de patients à risque, il serait intéressant de sonder le profil des acides gras de l'EAT grâce à une acquisition spécifique, car il a était constaté que ces profils lipidiques étaient différents entre des patients diabétiques et non diabétiques.

Contributions personnelles

Avant d'avoir utilisé les approches d'apprentissage profond montrées dans cette étude, j'ai d'abord exploré des algorithmes non supervisés basés sur le contour actif pour segmenter la graisse épicardique et paracardique. Cependant, cette approche n'a pas abouti en raison de résultats insatisfaisants et de trop nombreux paramètres à configurer. C'est pourquoi j'ai décidé d'étudier les réseaux AE en les entraînant et optimisant sur une base de données rétrospective que j'ai organisée pour faciliter le processus. J'ai effectué un examen approfondi de la littérature sur l' apprentissage profond. En parallèle, j'ai suivi une formation en ligne (MOOC, Stanford machine learning class) pour renforcer mes connaissances et être à jour en matière d'apprentissage profond. Une fois ma formation terminée, j'ai conçu les réseaux dédiés à cette étude, et j'ai utilisé la même base de données que celle que j'avais recueillie lors des expériences précédentes avec les contours actifs pour entraîner les deux réseaux AE sélectionnés. J'ai également effectué l'analyse statistique, préparé toutes les figures et rédigé l'article.

Enfin, une fois l'étude terminée et le manuscrit prêt à être soumis, j'ai intégré le U-Net optimisé dans un plugin FSLeyes pour faciliter sa mise à disposition à la communauté.

B. Imagerie de précision de la graisses grâce à l'imagerie eau-graisse

Contexte et motivation

La fraction graisseuse en densité de protons (PDFF) est un biomarqueur non invasif pour évaluer l'adiposité des tissus. Pour obtenir ce biomarqueur quantitatif, de nombreux algorithmes de séparation du signal eau-graisse ont été développés avec une diversité de méthodes et implémentés dans différents langages de programmation. Nous avions besoin de sélectionner l'un d'entre eux avec des critères basés sur la précision et la fiabilité pour traiter nos données IRM. Cependant, une décennie s'est écoulée depuis le dernier benchmark de ces algorithmes. En effet, lors du congrès « ISMRM Fat-Water MRI » en 2012, un défi a été organisé pour comparer ces algorithmes sur une multitude de jeux de données in-vivo et une boîte à outils MATLAB a été développée pour faciliter les comparaisons futures. Cependant, il était nécessaire de renouveler cette comparaison avec l'état de l'art des algorithmes open-source en utilisant des simulations numériques afin de les explorer, évaluer et valider. De plus, il y un besoin d'extension de cette boîte à outils pour qu'elle tienne en compte d'autres langages de programmation mais aussi la diversité des modèles de spectres de graisse. Ainsi, en accord avec les travaux portant sur la standardisation du PDFF, le but de cette étude était d'implémenter une boîte à outils numérique multi-langage pour aborder la performance dès l'algorithmes de séparation eau-graisse open-source.

Méthodes et résultats

Une boîte à outils open-source implémentée en MATLAB et Python a été développée pour évaluer les performances des méthodes récentes de séparation du signal eau-graisse. Des volumes synthétiques d'IRM eau-graisse ont été simulés avec l'entièreté de la gamme de PDFF (0- 100%), une large gamme de B_0 et variant selon le nombre de temps d'echos, leurs instants et le SNR. Pour la validation in vitro, un fantôme d'eau-graisse, façonné au laboratoire, a été acquis à 3T avec les mêmes paramètres d'acquisition que la simulation. Des données in-vivo challengeantes en termes de grande variation d' inhomogénéités du champ B_0, d'inter-écho important et de faible SNR ont également été acquises pour illustrer les performances des algorithmes.

La simulation Monte-Carlo et les expériences in-vitro ont mis en évidence que les algorithmes se sont avérés robustes contre les permutations eau/graisse et face aux grandes inhomogénéités du champ B_0 uniquement avec 5 échos et plus. Cependant, pour la quantification du PDFF avec 7 échos et un SNR=50, deux méthodes se sont révélées inexactes, tandis que deux autres ont fourni une précision du PDFF qui dépendait du schéma d'espacement des échos ($P<0,05$) et les quatre autres ont fourni des performances similaires avec un biais <0,15 comme le montre la **Figure 0-2**. Par ailleurs, Le choix du modèle de spectre de graisse a influencé la quantification du PDFF et sévèrement celle du R_2*.

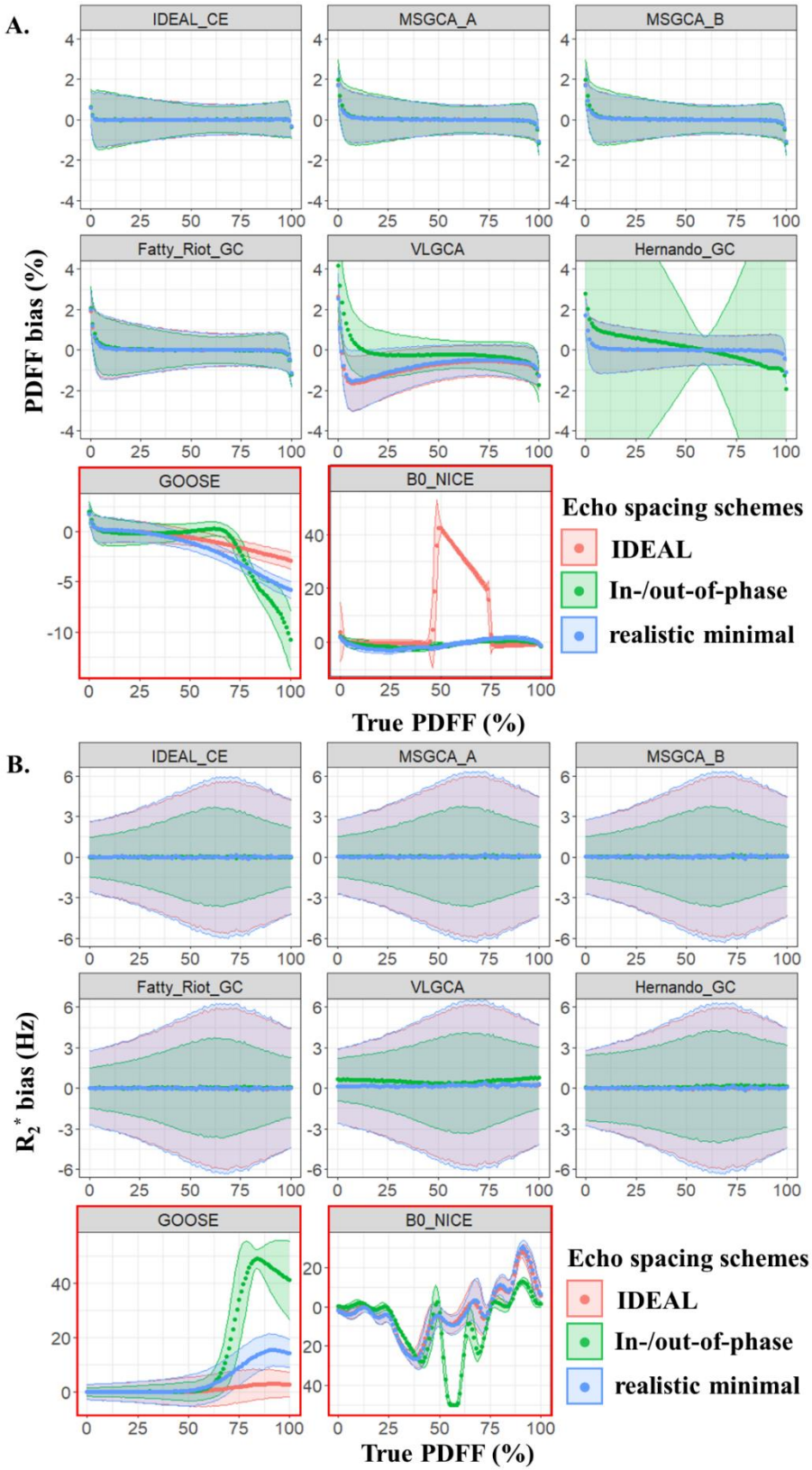

Figure 0-2 : Comparaison du biais PDFF (A) et R_2*. (B) de chaque algorithme sur des volumes synthétiques d'IRM-CSE avec NTE=7 et SNR=100. GOOSE et B0-NICE (en carré rouge) n'ont pas été étudiés plus avant en raison de résultats très biaisés.

Conclusion, limites et perspectives

Ce benchmark utilisant une boîte à outils open-source bi-langage offre la possibilité de mieux apprécier la précision et l'exactitude des algorithmes récents de séparation du signal eau-graisse pour la quantification du PDFF et du R_2*. Il pourrait également permettre d'optimiser les paramètres d'acquisition en prédisant les marges d'erreurs des algorithmes. Il aurait été intéressant d'avoir une plus grande diversité de méthodes qui soit basée sur les algorithmes commerciales, sur l'amplitude ou des algorithmes utilisant l''intelligence artificielle car ils sont de plus en plus présents dans ce domaine. Cette boîte à outils pourrait être grandement améliorée par des données in-vitro, in-vivo, multi-vendeurs et multi-champs afin de mieux valider les algorithmes. En outre, les algorithmes ont commencé à inclure le modèle de signal DIXON-MRI raffiné, conçu pour l'imagerie quantitative de paramètres liés à la composition lipidiques des tissus. Cette boîte à outils pourrait être donc étendue pour explorer la précision et la fiabilité de l'estimation de ces paramètres.

Contributions personnelles

À partir du benchmark organisé lors du congrès ISMRM Fat-Water MRI en 2012, j'ai donc réalisé une revue approfondie des algorithmes de séparation du signal eau-graisse. En parallèle, j'ai suivi un MOOC sur la recherche reproductible qui m'a sensibilisé sur les aspects avantageux de la recherche reproductible (processus de validation, métriques de comparaison, disponibilité du code) dans notre quête d'utilisation de l'algorithme "optimal". La diversité des processus de validation et des paramètres d'évaluation des performances des méthodes m'a encouragé à repenser et à développer un cadre pour une comparaison standardisée entre ces algorithmes. Inspiré par le format et la boîte à outils MATLAB de l'ISMRM 2012 utilisés pour le défi, j'ai mis en place une boîte à outils bi-langage (Python et MATLAB) open-source. Compte tenu de la variété des applications de l'imagerie eau-graisse, et de mes propres besoins en IRM de la graisse épicardique, j'ai inclus une bibliothèque exhaustive de spectres de graisse pour faciliter la calibration du modèle du signal. Pour une évaluation fiable et complète des algorithmes, j'ai réalisé les simulations numériques, participé à l'élaboration des échantillons in-vitro (deux lots, le 1er n'étant pas satisfaisant), acquis les données d'imagerie et de spectroscopie de ces échantillons, ainsi que les données in-vivo. Enfin, j'ai effectué l'analyse statistique, préparé toutes les figures et rédigé l'article qui a été soumis à Magnetic Resonance in Medicine. Il fut rejeté mais avec cependant des commentaires de revues encourageantes

qui nous invite à revoir la structure de l'étude en incluant plus d'algorithmes commerciaux ou basés seulement sur l'amplitude.

C. Caractérisation ex vivo de l'EAT par RMN

Contexte et motivation

Le benchmark des algorithmes de séparation d'eau-graisse a aussi révélé que la quantification du PDFF et du R_2* pourrait être biaisée en raison d'une mauvaise calibration du spectre multi-pic de graisse qui est modélisé dans le signal eau-graisse. Même si une diversité de spectres RMN de graisses humaines a été évaluée, le spectre RMN de l'EAT n'a pas encore été caractérisé dans la littérature. Ainsi, l'objectif de cette étude était d'explorer la signature RMN et le profil des acides gras de l'EAT dans des échantillons humains ex-vivo.

Méthodes et résultats

Neuf échantillons de tissu adipeux ex-vivo provenant de patients décédés ayant fait don de leur corps à la science (3 EAT, 4 VAT, 2 SAT) ont été acquis à 11,75T en utilisant la séquence STEAM. Les paramètres du modèle triglycéride (ndb, nmidb, cl) et la composition en acides gras (SFA, MUFA, PUFA) ont été calculés à l'aide d'un logiciel Python issu de notre laboratoire après quantification de la concentration relative des pics lipidiques (**Figure 0-3**).

Les résultats préliminaires sur la composition en acides gras suggèrent que les graisses épicardiques ont une teneur en SFA plus faible (31,57±12,61) et une teneur en MUFA plus élevée (54,97±14,03) par rapport à la graisse blanche commune : SAT (SFA: 49,34±4,96, MUFA 43,24±2,01 et VAT (SFA: 40,14±9,33, MUFA 43,49±7,74).

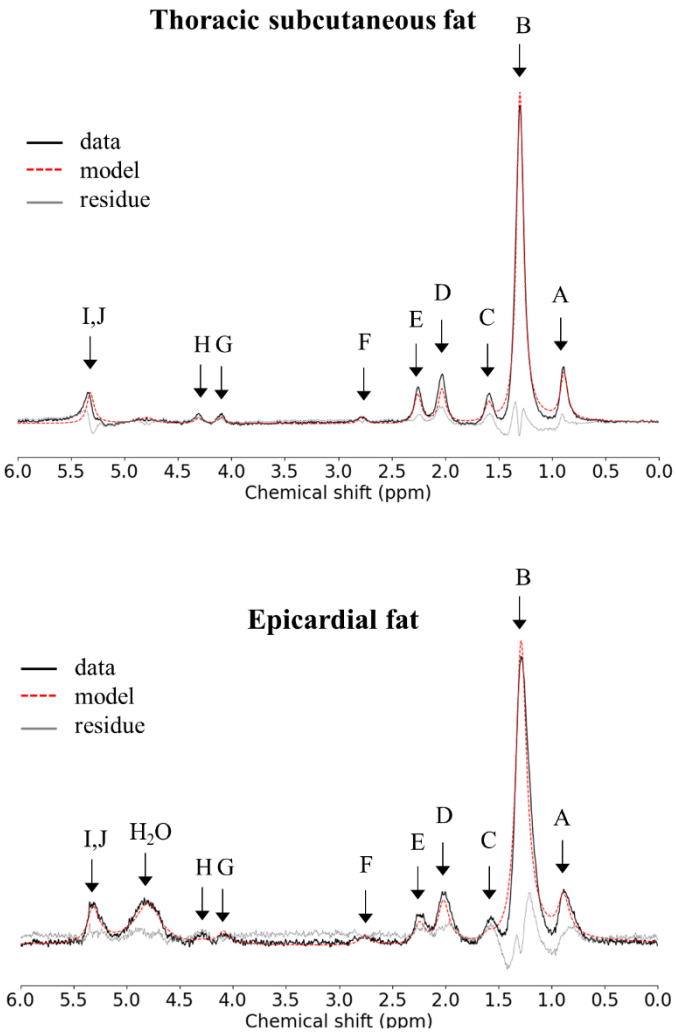

Figure 0-3: Exemples de spectres obtenus du même sujet avec la graisse sous-cutanée thoracique et la graisse épicardique. Les courbes noires représentent les spectres acquis avec la séquence STEAM. Le courbe d'ajustement (rouge) a été conçu pour quantifier l'eau (4,7 ppm) et le modèle des lipides. Le signal résiduel (gris) permet d'évaluer l'adéquation du modèle.

Conclusion, limites et perspectives

Dans cette étude sur des échantillons ex-vivo de graisses humaines, la signature RMN du tissu adipeux épicardique a été évaluée. Ces résultats préliminaires en termes de modèle de triglycérides et de composition en acides gras doivent être approfondis avec un échantillon de taille plus importante. Une confrontation de ces mesures avec l'analyse par chromatographie en phase gazeuse pourrait également apporter une perspective plus

claire à ces résultats. Cependant, après la réalisation complète de cette étude, une calibration plus fiable du spectre du tissu adipeux épicardique pourrait être fournie pour l'imagerie eau-graisse et ainsi réduire les biais de quantification PDFF et R_2* pour cette graisse spécifique.

Contributions personnelles

J'ai effectué un revue de littérature approfondie des caractérisations établies des tissus adipeux par chromatographie en phase gazeuse et par RMN. Cette étude a été vraiment menée grâce à un grand travail d'équipe: la collaboration avec le service d'endocrinologie de l'AP-HM pour la collection des échantillons ex-vivo qui a été cruciale, la préparation des échantillons, l'optimisation du protocole et des acquisitions à 11,75T ont toutes été réalisées avec l'aide de Joevin Sourdon et les interactions avec Tangi Roussel, qui a développé le logiciel Python, pour développer et mettre au point le traitement des spectres. J'ai participé à toutes ces étapes une fois les échantillons collectés et congelés par l'équipe d'endocrinologues : j'ai suivi toutes les expériences, j'ai ensuite réalisé le traitement des données de RMN, y compris les adaptations du code Python pour obtenir les paramètres souhaités, et j'ai préparé les tableaux et les figures correspondantes.

D. Caractérisation in vivo de l'EAT par imagerie DIXON

Contexte et motivation

L'IRM cardiaque DIXON a le potentiel de sonder l'accumulation et l'altération de la graisse cardiaque en cartographiant le PDFF et le R_2* L'imagerie DIXON 3D haute résolution est nécessaire pour détecter le péricarde, couche séparant la graisse épicardique de la graisse paracardique, qui est mieux visualisée au moment de la systole. L'IRM cardiaque DIXON est un défi en raison des mouvements cardiaques et respiratoires, avec en plus à 3T, une accumulation rapide de phase entre l'eau et la graisse concomitante avec un B_0 inhomogène. Pour surmonter cet obstacle, nous avons entamé une collaboration avec l'équipe de Matthias Stuber au CIBM CHUV-UNIL qui a développé une séquence « Free-Running » en respiration libre et auto-naviguée pour l'imagerie cardiaque à haute résolution, combinée à une reconstruction multidimensionnelle par « Compressed Sensing » à 1,5T.

Le but est d'obtenir une cartographie du PDFF et R_2* précise et fiable résolue au cours des cycles cardio-respiratoires. Durant le mouvement respiratoire et cardiaque, seuls les échos bipolaires permettaient d'obtenir un inter-écho suffisamment court mais souffraient de distorsions entre les échos pairs et impairs en raison des imperfections des gradients. L'objectif de ce travail était donc de proposer une IRM cardiaque DIXON à 3T à haute résolution pour la quantification du PDFF et du R_2*, en corrigeant la trajectoire dans l'espace k en utilisant la fonction de réponse impulsionnelle du gradient (GIRF)

Méthodes et résultats

L'IRM cardiaque Dixon en mode bipolaire avec 13 échos (TE1/ΔTE = 1,12/1,07ms) et en mode monopolaire avec 8 échos (TE1/ΔTE = 1,16/1,96ms) ont toutes les deux été acquises à 3T sur un fantôme eau/graisse, 10 volontaires sains et un patient diabétique. Les Dixon cardiaques bipolaires en mode Free-Running ont été reconstruites avec ou sans correction GIRF et ont été comparés aux Dixon monopolaires en in-vitro et in-vivo dans différentes régions d'intérêt.

Sans correction GIRF sur les Dixon bipolaires, des effets de flou et de halo sont apparus sur les échos pairs entraînant un biais de PDFF non négligeable de 4,90% in-vitro et de 23,49% dans les ventricules gauches de sujets sains alors qu'avec la correction GIRF, ces artefacts ont disparu avec une quantification précise du PDFF in vitro avec un biais moyen de 0,03% et plus réaliste in vivo avec des PDFF moyens de 0,78% et 0,84% dans les ventricules gauche et droit. En mode monopolaire, en raison d'un inter-écho important, des échanges eau-graisse étaient présents in-vitro et in-vivo avec une quantification moins précise avec des PDFF moyens de 2,35% et 2,53% dans les ventricules gauche et droit. Enfin, dans la cohorte de volontaires sains, la graisse épicardique avait une fraction graisseuse significativement ($P < 0,0001$) plus faible (80,36±7,10%) que la graisse sous-cutanée (92,49±4,25%).

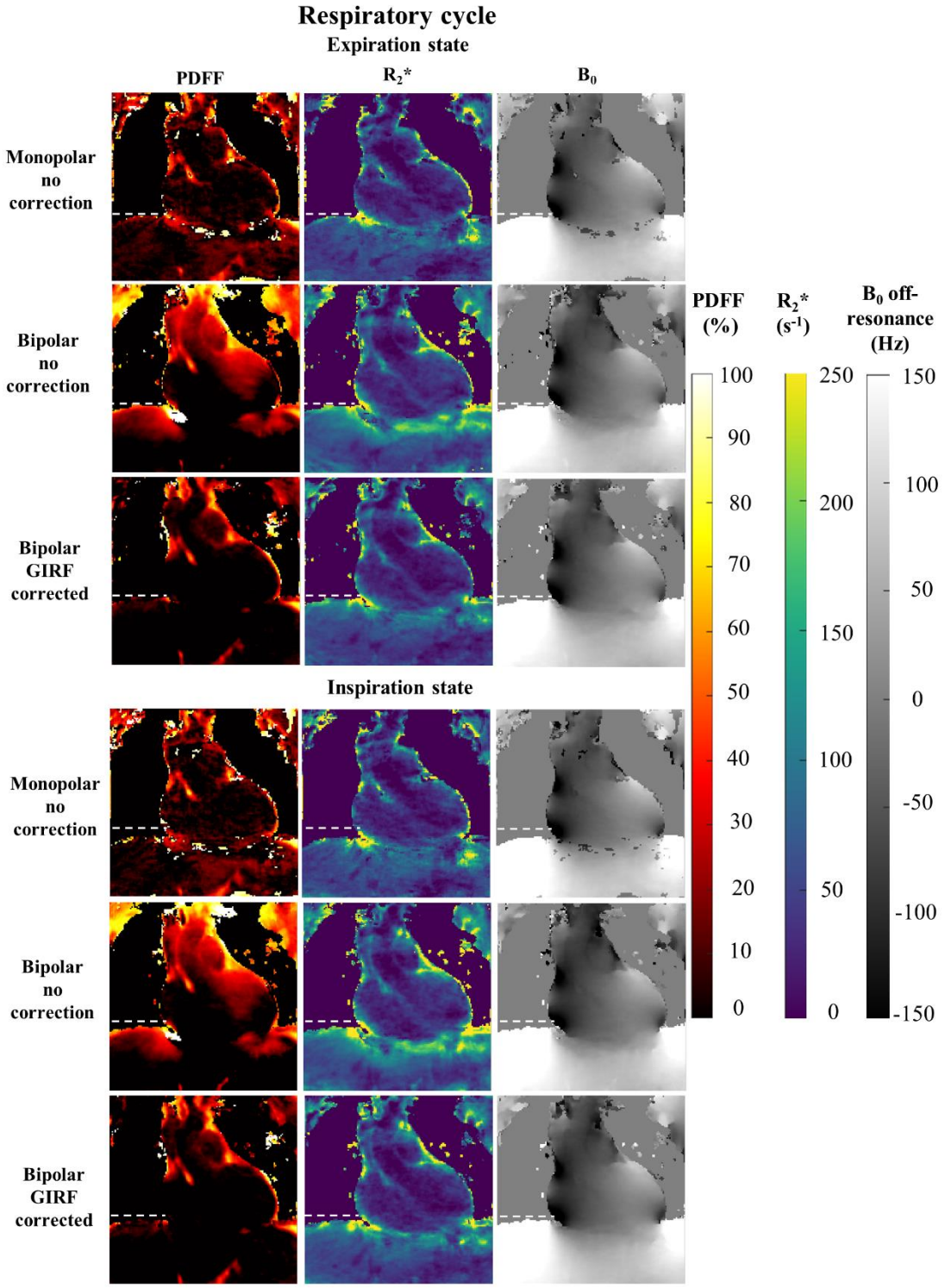

Figure 0-4 Au cours des différents états respiratoires, les cartes quantitatives de PDFF et R_2*, B_0 hors-résonance en vue coronale résultant de la correction monopolaire, bipolaire avec ou sans GIRF. La ligne blanche pointillée représente le niveau du diaphragme à l'état d'expiration.

Conclusion, limites et perspectives

Pour permettre un PDFF et un R_2* précis et à haute résolution, le Free-Running cardiaque Dixon à 3T s'est avéré nécessiter des échos bipolaires avec une correction de trajectoire de l'espace k réalisée avec le GIRF spécifique au système. Il aurait été intéressant d'explorer plus en détail la correction de trajectoire de l'espace k en ajoutant la valeur de correction des effets de gradient concomitants, comme cela est déjà fait à faible champ, mais aussi de l'appliquer à l'IRM monopolaire Free-Running Dixon. En outre, cette preuve de concept offre la possibilité d'étudier le PDFF et le R_2* du tissu adipeux épicardique ou, en outre, avec des temps d'écho suffisants, de caractériser la composition en acides gras dans les maladies métaboliques résolues dans les cycles cardiaques et respiratoires complets. En outre, il faciliterait l'émergence d'approches de quantification volumétrique automatique de la graisse cardiaque.

Contributions personnelles

Pour réaliser ce travail, nous avons commencé pendant ma thèse une collaboration avec l'équipe de Matthias Stuber au CIBM CHUV-UNIL. A cette fin, Davide Piccini nous a fourni la séquence WIP Free-Running qui permet d'acquérir des données multi-échos GRE free-running. Adele L.C Mackowiack a partagé son code de reconstruction d'images multi-échos en free-running (MATLAB). Ce pipeline de reconstruction devait être mis à jour avec l'ossature du code de reconstruction plus récent fourni par Jérôme Yerly, qui n'était pas adapté à la séquence multi-échos. J'ai fusionné, adapté et optimisé l'ensemble du pipeline de reconstruction Free-Running multi-écho pour répondre aux contraintes de mémoire de notre matériel et améliorer la qualité des images reconstruites. Pour la correction GIRF, nous avons également collaboré avec Josef Pfeuffer, de Siemens, grâce au soutien de Thomas Troalen. Josef a fourni la séquence de calibration, pour mesurer le GIRF de notre scanner, et le code MATLAB pour appliquer le GIRF dans une reconstruction spirale 2D. J'ai adapté ce code pour l'appliquer à des trajectoires 3D non cartésiennes et j'ai intégré la correction GIRF dans le pipeline de reconstruction. Cette intégration a représenté un certain temps puisque nous avons dû faire de la rétro-ingénierie de la simulation des gradient réalisés par la séquence. J'ai également acquis et reconstruit l'IRM DIXON in-vitro et in-vivo, effectué l'analyse statistique et préparé toutes les figures.

Introduction

Obesity and diabetes have become a scourge in our society. Mostly related to cardiac complications, many deaths of diabetic patients could be prevented by a better phenotyping of at-risk patients. The measurement of cardiac fat by MRI presents an emerging and promising diagnosis ahead of cardio-diabetic complications.

More than a decade of collaboration between the CRMBM and the endocrinology department of the AP-HM has shown that cardiac lipids accumulation is a major factor contributing to the development of cardiac complications. These findings have been confirmed and extended by a manifold of research worldwide. More specifically, epicardial adipose tissue (EAT), a fine deposit of fat on the surface of the heart muscle, secretes pro-inflammatory and prothrombotic adipocytokines that increase the risk of coronary heart disease(CHD). Abnormal accumulation of epicardial fat is a prognostic element but its evaluation, and even less its characterization, remain tedious and impractical in the clinics.

This thesis is deeply rooted in this collaboration and is very timely, as a renewed interest in imaging epicardial fat is emerging thanks to novel tools such as machine learning and high-resolution low-dose computed tomography. The primary hypothesis of this thesis is that the use of novel MRI techniques would allow to bring down these barriers that hamper the consideration of EAT in the clinics and exploit MRI for a refine analysis of cardiac fat accumulation.

This thesis, funded by the Mission for Transversal and Interdisciplinary Initiatives (MITI) program support by CNRS, was conducted at “Centre de Résonance Magnétique et Biologique et Médicale” (Aix-Marseille Univ, CNRS, CRMBM, Marseille, France) in the “cardiovascular system” team.

The manuscript is organized in five chapters. The first chapter introduces the basic knowledge of EAT physiology, imaging, characterization, and artificial intelligence

segmentation essential to the understanding of the original work done during this thesis which is described in the following chapters. The second chapter presents an automatic segmentation of epicardial adipose tissue on standard cardiac images leveraged using Fully Convolutional Networks (FCN). The 3rd, 4th and 5th summarize the different steps to achieve a precise and reliable Proton Density Fat Fraction (PDFF) and the effective transverse magnetization rate (R_2*) quantification of EAT. The third one then assesses precision performance of open-source fat-water signal separation algorithms using a bi-language toolbox developed to standardize the comparison. The fourth chapter explores the NMR signature of EAT for reducing PDFF and R_2^* quantification bias in fat-water imaging. Finally, the fifth chapter demonstrates a proof-of-concept of bipolar Free-Running Dixon MRI with precise PDFF and R_2* quantification leveraged by trajectory correction using gradient impulse response function (GIRF) method.

Chapter 1 : Clinical and scientific context of epicardial adipose tissue

1.1 Epicardial adipose tissue

1.1.1 Anatomy and Physiology

Epicardial adipose tissue (EAT) is a beige adipose tissue located between the heart and the visceral pericardium, in direct contact with the myocardium. It should be distinguished from the paracardial adipose tissue (PAT), which is external to the parietal pericardium. Thus, only EAT has access to the myocardium and its coronary circulation, potentially impacting the cardiac health. The pericardial fat is the combination of EAT and PAT, considering all fat surrounding the heart. It contributes up to 20% of the whole cardiac mass(1,2) but represents only 1% of the total fat mass(3).

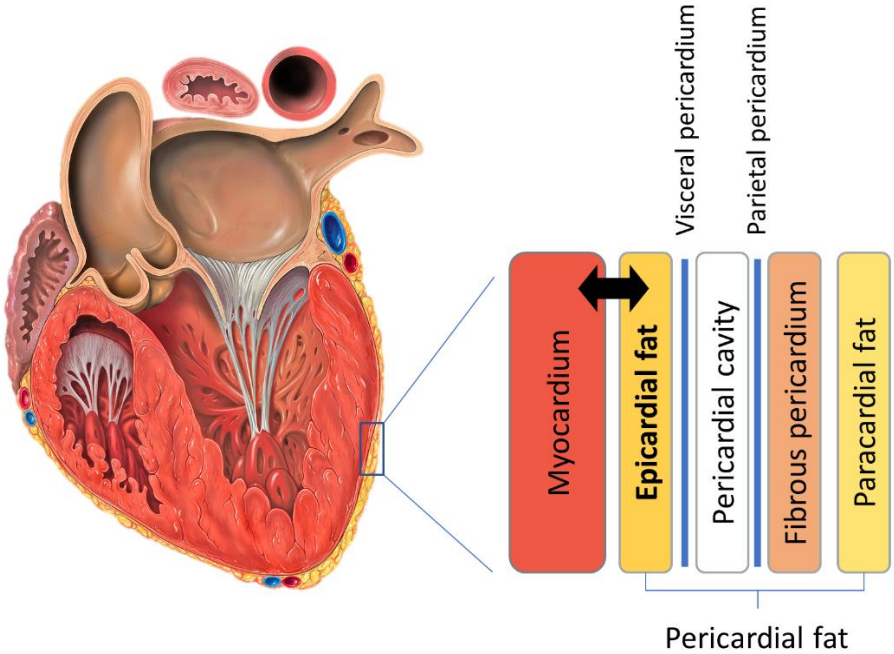

Figure 1-1 : The anatomy of epicardial adipose tissue (EAT). Epicardial fat, or EAT, is the only adipose tissue that has access to the myocardium. Since it is a metabolically active organ, it can deposit deleterious hormones in the coronary arteries. The separation between epicardial and paracardial fat is very subtle.

EAT has a multifaceted role in cardiac physiology (**Figure 1-2**). It acts as a local energy storage for the heart, but also protects against exposure to high levels of free fatty acids (FFA) and subsequent risks of lipotoxicity(4). Besides, EAT has a higher rate of lipogenesis and lipolysis compared to other fat depots(5). Its mechanical functions include protecting the coronary arteries against torsion induced by arterial pulse wave and cardiac contraction(6). Its beige features suggest that EAT can protect the heart against hypothermia(7). It is also an endocrine organ that secretes adiponectin which protects coronary circulation, inhibits oxidative stress and regulating inflammatory stimuli.

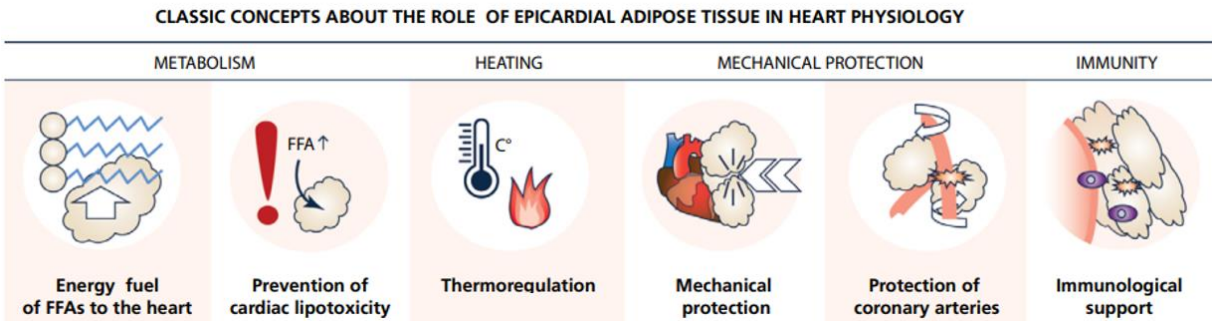

Figure 1-2 : The classic concepts about the role of epicardial adipose tissue in heart physiology. Adapted from (8)

1.1.2 Epicardial fat composition

Human adipose tissues, namely body fat, can be subdivided into two main types: white or brown adipose tissue. The primary function of white adipose tissue (WAT) is to be an energy storage, and hence, its adipocytes consist of a single large lipid droplet of triglycerides. WAT is widely distributed over all the body and depending on its location, it can be categorized as subcutaneous (SAT) or visceral fat (VAT). In addition to its lipid storage function, WAT is also an endocrine organ(9), secreting hormones, adipokines that impact whole-body metabolism.

In contrast, brown adipose tissue (BAT) main function is heat production through energy consumption. This non-shivering thermogenesis is achieved thanks to the uncoupling protein-1(UCP-1) (10), which is expressed in mitochondria of BAT.

In this context, epicardial adipose tissue is deemed beige (or brite) adipose tissue (BeAT)(11). BeAT is an intermediate phenotype with features of both WAT and BAT. Indeed, BeAT cells originate from WAT through a process called 'browning'. Eventually, they share classical characteristics of BAT such as high mitochondrial content and multilocular lipid droplets. The processes of browning or whitening remain a topic of active research, in particular for the browning of EAT(12).

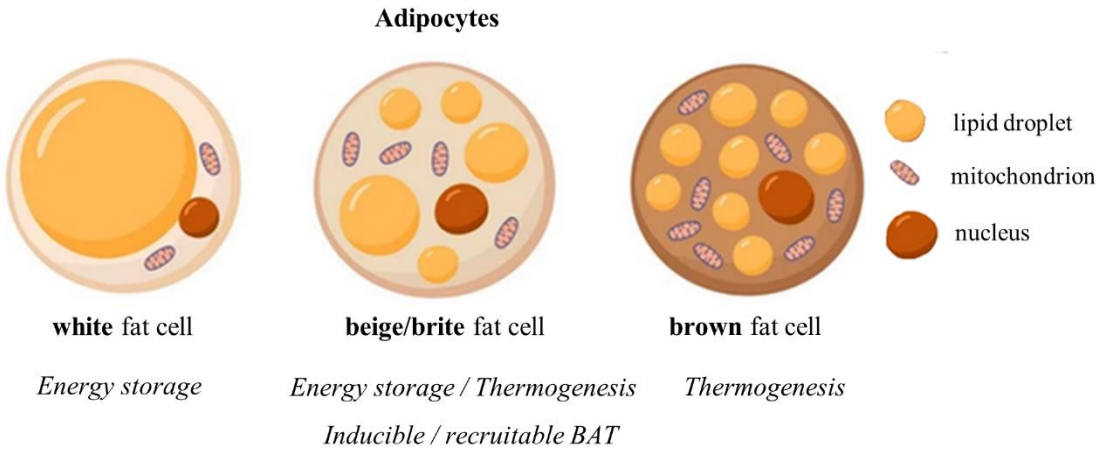

Figure 1-3 : Type of adipose tissue. Epicardial adipose tissue is deemed beige fat, with its characteristics varying between a predominant white or brown fat.

1.1.3 Role of epicardial adipose tissue in cardiovascular diseases

Under pathological conditions, EAT shifts from its cardio-protective role to an inflammatory substrate, promoting the development of cardiovascular diseases (CVD) such as coronary artery disease(13,14), atrial fibrillation(15,16) and heart failure(17).

Indeed, EAT directly contributes to the development and progression of CVD not only because of its anatomical proximity with the heart and coronary arteries but mainly due its quantity and activity(18).

The multifaceted complex mechanisms induced by EAT in these diseases include:

- inflammation(19) by the secretion of pro-inflammatory cytokines (such as interleukin (IL)-6, tumor necrosis factors (TNF) and downregulation of anti-inflammatory adiponectin
- fibrosis (20) by production of profibrotic mediators

- fatty infiltration(21)
- glucotoxicity(22)

Moreover, EAT inflammation or accumulation have also been observed in patients with type 2 diabetes(23) (T2D) and obese(24,25). Thus, EAT is a well-established risk factor CVD and its accumulation has been defined as a biomarker(26).

1.2 Epicardial fat characterization

1.2.1 Molecular and Cellular characteristics

The main component of the lipid droplets stored in adipocytes is triglycerides(27). Triglycerides consist of three fatty acids (FA) esterified to the three hydroxyl groups of glycerol. FA consist of a hydrocarbon aliphatic chain terminated by a carboxylic acid group. The nomenclature of its chemical structure is (X : YnZ) : with the chain length (X), the number of double bonds (Y) and position of the first double bond starting from the terminal methyl group of their chain (Z).

Some FA contain double bonds, which induces a bend in the molecular structure. Fatty acids without it are called saturated fatty acids (SFA) whereas the others are called unsaturated fatty acids (UFA). Those UFA could be described more precisely as monounsaturated fatty acids (MUFA) if they have only one double bond or as polyunsaturated fatty acid(PUFA) otherwise. PUFA could be categorized into three main families according to the position of the first double bond (3rd, 6th, 9th carbon atom) starting from the terminal methyl group of their chain: ω -3, ω -6, ω -9.

Linoleic acid (18:3n-6) and α-linoleic acid (18:3n-3) are considered essential to human because we are unable to synthesize it and can only be obtain through diet.

The fatty acid profile of an adipose tissue can also be described in terms of mean values per triglyceride of number of double bonds (ndb), number of methylene-interrupted double bonds (nmidb) and the chain length (cl). This triglyceride model profile(28) is mostly used in-vivo in Magnetic Resonance Spectroscopy (MRS) or Magnetic Resonance Imaging (MRI) quantification.

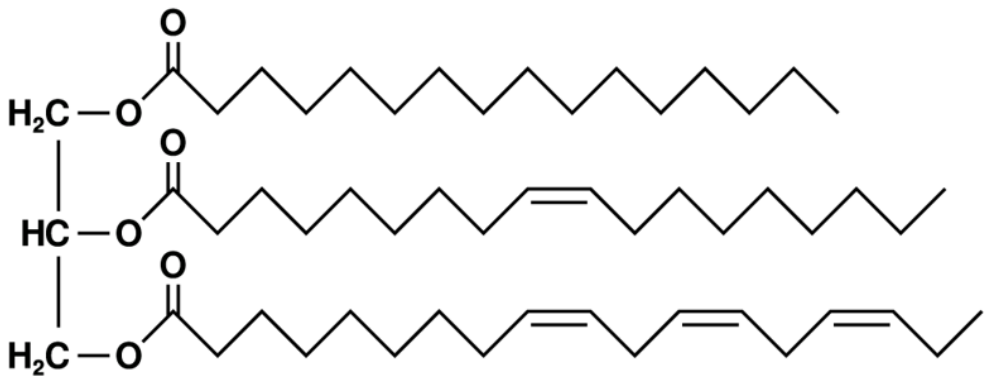

Figure 1-4 : Schematic example of a triglyceride molecule structure. From top to bottom, it consists of a palmitic acid (16:0), an oleic acid (18:1n-9) and an α-linoleic acid (18:3n-3). Its triglyceride model profile is ndb=4, nmidb=2 and cl=17.33. Extracted from Wikipedia.

1.2.2 Gas Chromatography

Gas chromatography (GC) is the gold standard technique to evaluate the relative abundance of each fatty acid (QFA) in a sample. The process separates molecules from a mixture by injecting it at the entrance of a column containing a solid or liquid active substance called stationary phase, then passing through it using a carrier gas and depending of each molecule affinity with the stationary phase, they eluted and are detected at different time.

Fatty acid profiles from various adipose tissues including EAT have been identified using GC and were summarized in **Table 1-1**. Indeed, EAT had a superior proportion of SFA compared to subcutaneous adipose tissue in advanced Coronary Artery Disease (CAD) population(29). Diabetic disease modified the fatty acids profile of EAT with a diminution of PUFA percentage(30).

Table 1-1 : Summary of fatty acids composition and triglyceride model parameters of different human adipose tissue estimated using gas chromatography.

Study	Subject	Number	Adipose tissue	UFA	SFA	MUFA	PUFA	cl	ndb	nmidb	Year
Field et al.(31)	healthy	20	SAT	73.77	26.23	58.84	14.93	17.39	2.74	0.52	1985
Garaulet et al.(32)	Obese overweight	76	SAT	72.61	27.39	54.59	18.02	17.45	2.85	0.67	2006
		57	Perivisceral	69.19	30.81	51.66	17.53	17.42	2.72	0.65	
		24	Omental	74.37	25.63	55.81	18.57	17.49	2.91	0.68	
Hodson et al.(27)	healthy	7354	SAT	70.50	29.50	53.99	16.51	17.29	2.69	0.58	2008
Pezeshkian et al.(29)	CAD	42	**EAT**	**64.20**	**35.80**	**48.26**	**15.94**	**17.17**	**2.49**	**0.57**	2009
			SAT	72.42	27.58	54.86	17.56	17.25	2.79	0.62	
Lundbom et al.(33)	healthy	10	SAT	70.64	29.36	58.29	12.35	17.39	2.60	0.48	2010
Pezeskhian et al.(30)	Diabetic	28	SAT	68.49	31.51	53.15	15.34	17.19	2.58	0.52	2013
			EAT	**64.89**	**35.11**	**50.86**	**14.03**	**17.22**	**2.46**	**0.51**	
	No Diabetic	40	SAT	72.23	27.77	54.84	17.38	17.26	2.78	0.61	
			EAT	**63.30**	**36.70**	**46.94**	**16.36**	**17.16**	**2.51**	**0.61**	
Hjelmgaard et al.(34)	At time elective cardiac surgery	49	**EAT**	**64.60**	**35.40**	**51.93**	**12.67**	**17.40**	**2.48**	**0.54**	2018
			PAT	65.06	34.94	52.39	12.67	17.39	2.46	0.51	
			SAT	65.85	34.15	53.02	12.83	17.40	2.49	0.51	
Nemeth et al.(35)	Healthy overweight	13	SAT	61.90	38.10	49.77	12.12	17.10	2.25	0.40	2019
Trinh et al.(36)	Lymphedema patients	18	SAT	72.50	27.50	60.20	12.30	17.31	2.63	0.46	2020

1.2.3 Magnetic Resonance Spectroscopy

The invasive nature of GC is less suitable for longitudinal, in-vivo study. As an non-invasive alternative, MRS or MRI approaches have been used for FAC quantification(36–42).

FAC of an adipose tissue can be estimated using Magnetic Resonance (MR) since each hydrogen proton of the triglyceride molecule contributes to the MR signal(43). The position of those protons within the triglyceride molecule result in different resonance frequencies in the NMR spectrum (**Figure 1-5** and **Table 1-2**). The chemical composition of the adipose tissue is estimated by calculating the amplitude of those peaks which depending of the field strength can vary up to 10 different peaks resolution (**Table 1-2**). Hamilton(28) simplified the NMR triglyceride spectrum model by describing the theoretical amplitude of each peak with only three parameters: the number of double bonds (ndb), the number of methylene-interrupted double bonds (nmidb) and the chain length (cl).

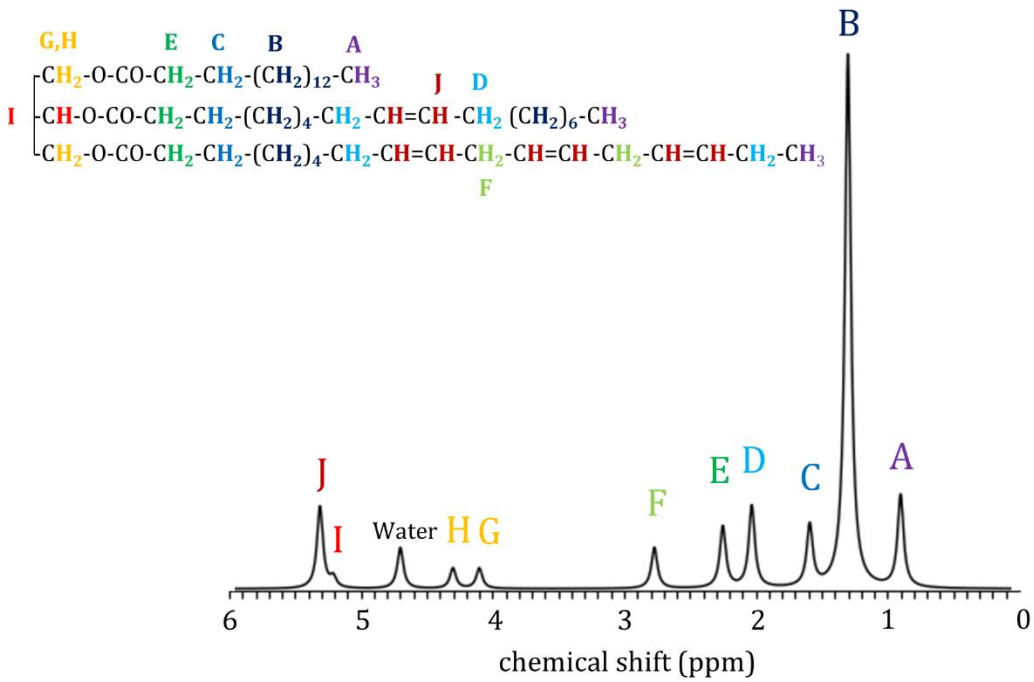

Figure 1-5 : Schematic illustration of a triglyceride molecule (top) and the corresponding MR spectrum (bottom). The letters refer to the peak assignments in **Table 1-2**.

Table 1-2 : Peak assignments and their corresponding chemical shift and theoretical amplitude expressed using the triglyceride model parameters (number of double bonds (ndb), number of methylene-interrupted double bonds (nmidb) and the chain length (cl)). The hydrogen atoms of interest are written in bold text.

Peak	Chemical shift(ppm)	Type	Proton Position	Theoretical Amplitude
A	0.90	Methyl	-CH_2-C**H**$_3$	9
B	1.30	Methylene	-(C**H**$_2$)$_n$-	6(cl-4)-8ndb+2nmidb
C	1.59	β-Carboxyl	-C**H**$_2$-CH_2-COO	6
D	2.03	α- Olefin	-C**H**$_2$-CH=CH-	4(ndb-nmidb)
E	2.25	α- Carboxyl	-CH_2-C**H**$_2$-COO	6
F	2.77	Diacyl	-CH=CH-C**H**$_2$-CH=CH-	2nmidb
G	4.10	Glycerol	-C**H**$_2$-O-CO	2
H	4.30	Glycerol	-C**H**$_2$-O-CO	2
I	5.21	Glycerol	-C**H**-O-CO-	1
J	5.31	Olefin	-C**H**=C**H**-	2ndb

The MR-estimated parameters ndb and nmidb can be translated to SFA, MUFA, and PUFA according to the following set of equations:

$$SFA = 1 - \frac{ndb - nmidb}{3} \quad ; \quad UFA = \frac{ndb - nmidb}{3}$$

$$MUFA = \frac{ndb - 2nmidb}{3} + TriUFA \quad ; \quad PUFA = \frac{nmidb}{3} - TriUFA$$

The fraction of triunsaturated fatty acids ($TriUFA$) can either be ignored $TriUFA$=0 (38) or be approximated by a fixed value of 2% (44).

Fatty acid profiles and triglyceride model from various human adipose tissues have been identified using MRS and were summarized in **Table 1-3**. To our knowledge, there were no human EAT NMR spectrum documented in the literature at the time of this thesis.

Table 1-3 : Summary of fatty acids composition and triglyceride model parameters of different human adipose tissue estimated using MRS.

Study	B0	Method	Subject	Number	Adipose tissue	SFA	MUFA	PUFA	cl	ndb	nmidb	Year
Ren et al.(38)	7T	STEAM	Healthy volunteers	20	SAT	29.1(3.5)	49.4(4.8)	24.5(3.1)				2008
Lundbom et al. (37)	1.5T	PRESS	NAFLD patients	17	SAT			37.6(4.3)				2010
Peterson et al.(39)	3T	STEAM	Healthy volunteer	1	SAT				17.9(0.4)	3.52(0.18)	0.71(0.05)	2013
Hamilton et al.(40)	3T	STEAM	NAFLD and obese subjects	340	VAT				17.5[1]	2.72(0.19)	0.69(0.14)	2017
					dSAT				17.5[1]	2.80(0.17)	0.75(0.13)	
					vSAT				17.5[1]	2.83(0.20)	0.74(0.15)	
Nemeth et al.(35)	3T	STEAM	Male volunteers, sedentary	21	SAT					2.48(0.06)	0.58(0.03)	2019
					VAT					1.90(0.16)	0.37(0.06)	
Trinh et al.(36)	3T	STEAM	Lymphedema patients	19	SAT	4.3(4.3)	64.4(4.9)	31.3(5.6)	17.79[2]	3.86(0.24)	1.02(0.11)	2020
						5.1(4.3)	61.1(0.8)	33.9(3.5)	17.19[2]	2.28(0.17)	0.17[3](0.08)	
Ouwerkerk et al.(42)	3T	PRESS	Healthy volunteers	17	WAT			48(23)				2021
				16	BAT			30(22)				

cl : [1]Fixed, [2]expressed as ndb, nmidb : [3]expressed as ndb

1.3 Epicardial fat in Radiology

Different imaging modalities have been identified to visualize and quantify EAT. Strengths and limitations of each of them have been summarized in **Table 1-4**. In a single exam, compared to Echocardiography and Cardiac Computed Tomography (CCT), cardiac MRI may offer a high-resolution volumetric quantification of EAT burden with measurement of heart function, morphology, perfusion.

Table 1-4 : Imaging modalities to quantify epicardial adipose tissue.

Imaging Modality	**Strengths**	**Limitations**
Echocardiography	Widely Available Low cost	Moderately reproducible Only thickness quantification
Cardiac Computed Tomography (CCT)	Highly reproducible Volumetric quantification Automatic segmentation Density/attenuation quantification	Radiation exposure Lack of myocardial characterization
Cardiovascular Magnetic Resonance (CMR)	Highly reproducible Volumetric quantification Fat characterization Coupled with complete cardiovascular characterization	High cost, low availability Medium resolution Tedious manual segmentation

1.3.1 Epicardial fat quantification in cardiac MRI

Epicardial fat is visible on many routine cardiac MRI examinations. Indeed, in a standard protocol, the heart with its surrounding cardiac fat is mostly imaged along three anatomical views: short axis view (**Figure 1-6**.A), four-chamber view (**Figure 1-6**.B) and 2-chamber view (**Figure 1-6**.C). However, the cardiac fat has long been considered as an obstacle in MRI: it is source of artifacts due to its hyperintensity, chemical shifted and partial volume effect, hiding epicardium and/or coronary arteries. Fat suppressed

imaging (**Figure 1-6**.D) using a fat saturation pulse remains often employed in routine and it is still a topic of research(45).

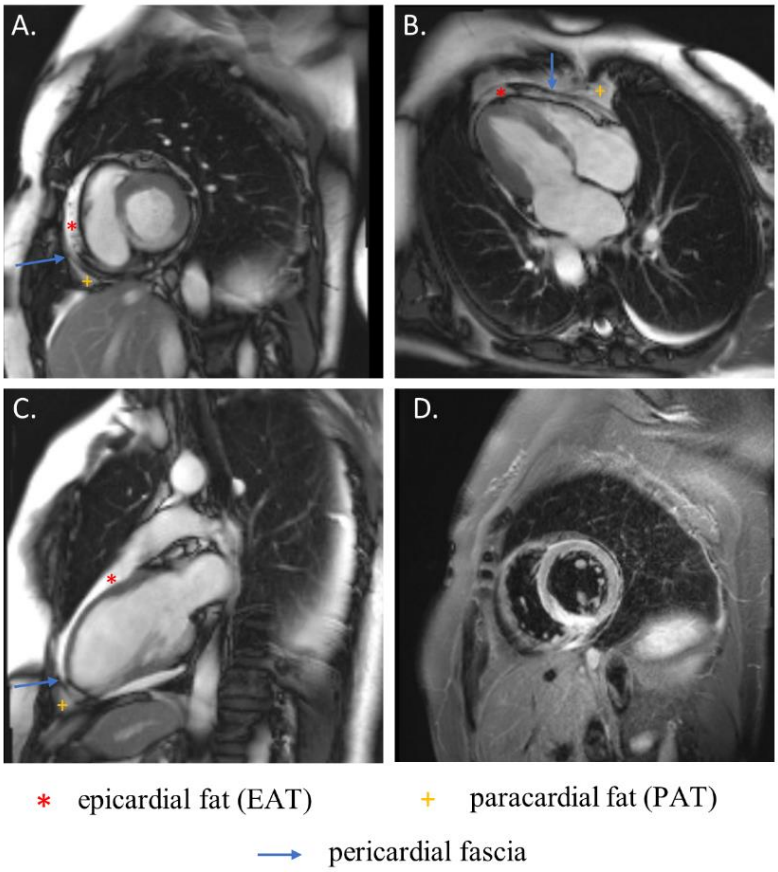

Figure 1-6 : Epicardial fat imaging during a standard cardiac exam. On short-axis (A.), four chamber (B.),and two-chamber (C.) cine sequence. EAT appears as hyperintense whereas on Short-TI Inversion Recovery (STIR), it is hided.

EAT evaluation using MRI is an emerging topic of research and its measurement is mostly performed manually whether on stack of short-axis cine(46–48) or in four-chamber cine(49–51) for volumetric or area quantification respectively. The distinct segmentation of EAT from PAT using MRI is difficult since the pericardial fascia is not clearly visible, in particular on short axis views (**Figure 1-7**). However, cine temporal information often helps experts in this tedious task.

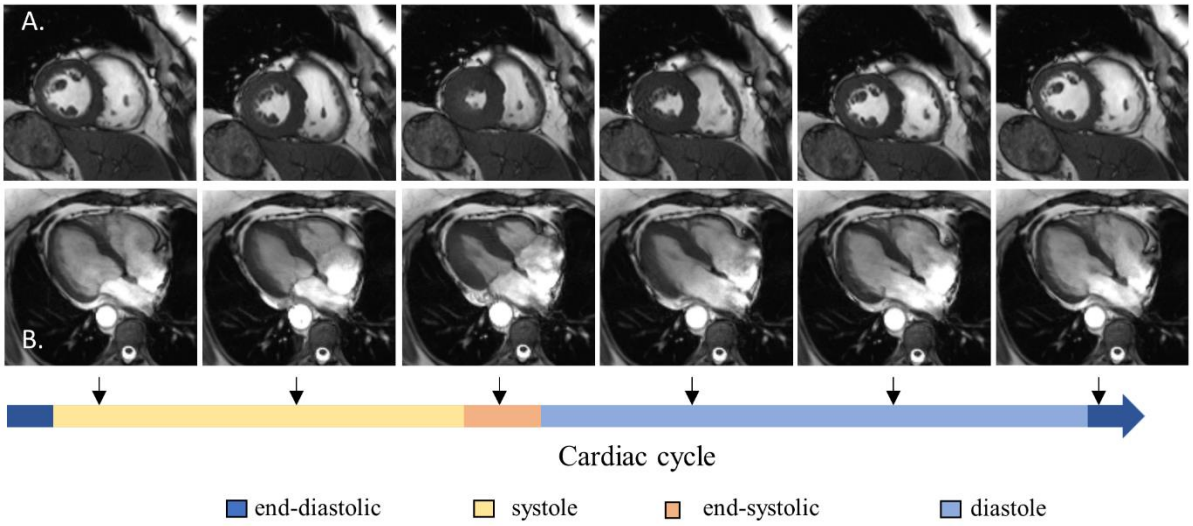

Figure 1-7 : Epicardial fat imaging during a cardiac cycle using short-axis cine (A) or four-chamber cine (B).

At the time of the start of this thesis, only two methods (52,53) for automatic, or semi-automatic, MRI-based EAT segmentation had been submitted in conferences. However, both studies had been demonstrated on very small sample sizes: less than 15 subjects each. Cristobal-Huerta et al. (52) developed an automatic pipeline including active contour and Law texture to segment EAT from a single cropped cine frame whereas Fulton et al. (53) provided a semi-automatic process using landmarks to unroll images into polar coordinates before using a neural network for segmentation of EAT, from a single cine frame as well.

1.3.2 Model-based water/fat separation by chemical shift imaging

Chemical shift encoded (CSE) MRI techniques exploit the differences in precession frequencies of water and fat tissues to identify them and even characterize fat tissues on a voxel level, at a high spatial resolution(54). CSE-MRI requires the acquisition of multiple images at different echo times (TEs), for the fat and water signals to accumulate different phase values, depending on their precession frequencies.

Using a simplified model which assumes that the spectral peak(s) are known a priori (calibrated by MRS experiments), fat and water images are then separated.

1.3.2.a Simplified Model

The original CSE-MRI method for fat water imaging was introduced by Dixon(55), based on a simplified model of the signal y(t) given by:

$$y(t) = W + Fe^{i\omega_B t} \qquad \text{Eq. 1-1}$$

where W and F are the water and fat signals and ω_B the difference of resonance frequencies of fat and water. In this model, the fat spectrum is assumed to be depicted with only one peak (B) corresponding to a chemical shift of 3.4 ppm relative to water.

In the original technique called two-point Dixon, specific echo times t_{IP} and t_{OOP} corresponding to Water and Fat signal to be in-phase or out-of-phase respectively are chosen to easily solve for Water and Fat image:

$$y(t_{IP}) = W + F \qquad y(t_{OOP}) = W - F$$

$$W = \frac{y(t_{IP}) + y(t_{OOP})}{2} \qquad F = \frac{y(t_{IP}) - y(t_{OOP})}{2}$$

However, this model (Eq. 1-1) neglects the B_0 field inhomogeneity, T_2^* relaxation time, initial phase error and also considered only one fat resonance which does not represent the complexity of the triglyceride spectrum (**Figure 1-5**).

1.3.2.b Multi-peaks Model

An iterative method based on the Iterative Decomposition of water and fat with Echo Asymmetry and Least-squares estimation algorithm (IDEAL)(56) has been developed to solve more general and realistic model signal given by:

$$y = \left(W + F\sum_{m=1}^{m} \alpha_m e^{i\omega_m t}\right) e^{(i(\omega_0+\varphi_0)-R2^*)t}$$

with W and F corresponding to water and fat absolute signal, ω_0 the off-resonance, $\varphi_0 t$he initial phase, R_2^* the transversal decay and α_m, $e^{i\omega_m}$ the relative amplitude and frequency offset of a fat spectrum respectively.

Since the development of IDEAL method, a diversity of advanced methods has emerged for the separation of fat and water signal. Whether utilizing magnitude or complex data fitting, algorithms can be based on voxel-wise(39,57–61), cluster(62,63), region(64–71), graph-cut(72–79) and more recently, deep learning(80–84) approaches. (**Table 1-5**). Magnitude-based approaches are more insensitive to phase errors and avoid the estimation of the challenging ω_0 field map but have a lower SNR performance(85) for fat-water signal separation. Advanced complex-based approaches had a higher SNR performance but could suffer from fat/water swaps in the presence of highly inhomogeneous B_0 field. The last benchmark of fat-water separation algorithms was organized during the 2012 ISMRM fat-water MRI Workshop on a multitude of in-vivo datasets(86).

Table 1-5 : Summary of fat and water signal separation algorithms published since 2012 ISMRM fat-water MRI Workshop.

Approach	Selected Work	Description /Originality	Validation	Year
Deep Learning	Liu et al.(84)	Multi-echo bidirectional convolutional residual network	V,C	2021
	Jafari et al.(83)	U-net with unsupervised training	V	2021
	Goldfarb et al.(82)	U-net with water,fat, R_2*and field-inhomogeneties output maps	V	2019
	Andersson et al(81)	U-net with water and fat output maps	V	2019
	Cho et al.(80)	Simple CNN and synthetic field inhomogeneity data augmentation method	V	2019
Graph Cut	Boehm et al.(79)	Single-min-cut method with variable layer graph enabling irregular field-map spacing sampled	N,P,V	2021
	Andersson et al.(78)	Quadratic pseudo-boolean optimization multi-scale approach with spatial smoothing term	C	2018
	Cui et al.(77)	Single-min-cut method restricting field-map candidates to its local minima voxel-wise estimation (rGOOSE)	C	2018
	Diefenbach et al.(76)	Incorporation of a priori information of the magnetic field distortions	N,V	2018
	Berglund et al.(75)	Quadratic pseudo-Boolean optimization multi-scale graph-cut	C	2017
	Stinson et al.(74)	graph-cut with constrained phase model on dual echo	P,V,C	2017
	Cui et al(73)	Single-min-cut method (GOOSE)	C	2015
	Berglund et al.(72)	Quadratic pseudo-boolean optimization graph cut	V	2012
Region Based	Peng et al.(71)	Region growing extension based on extraction of fat-water transition region instead of seed pixels	N,V,C	2020
	Bydder et al.(70)	IDEAL method with constrained parameters	N,V	2020
	Cheng et al.(69)	Self-feeding phasor estimation with multi-level resolution region-growing	C	2017
	Zhang et al.(68)	Binary quadratic optimization on dual-echo Dixon	V	2017
	Wang et al.(67)	Region growing dedicated to spiral 3 point Dixon method	N,V	2016

Approach	Selected Work	Description /Originality	Validation	Year
Region Based	Liu et al.(66)	Method based on pixel wise magnitude fitting in parallel to region based field map estimation	C	2015
	Soliman et al.(65)	Region-based labeling	V	2014
	Yu et al.(64)	fat likelihood analysis by identifying fat- and water-dominant pixels by exploiting the fitting residuals of two different signal models as complementary information	V	2012
	Tsao et al.(87)	Hierarchical IDEAL 2D multi-resolution optimization	P,V	2012
Cluster Based	Siracusano et al.(63)	K-means clustering for addressing spatial variation of fat spectra	V,C	2018
	Romu et al.(62)	Fat-water separation pipeline with tissue magnitude based clustering, phase unwrapping on dual echo Dixon	V	2017
Voxel-wise	Bagur et al.(61)	NLSQ magnitude fitting using the multistart Levenberg–Marquardt algorithm	N,P,V	2019
	Leporq et al.(60)	NLSQ fitting using the multistart Levenberg–Marquardt algorithm	P,V	2015
	Leporq et al.(59)	Multi-step fitting approach	N,P,V	2014
	Zhong et al.(58)	Multi-step magnitude NLSQ fitting approach using Levenberg–Marquardt algorithm	N,V	2014
	Leporq et al. (57)	Magnitude based method with a signal model with T_2* and T_1 effect	P,V	2013
	Peterson et al.(39)	Iterative method to solve a signal model with an additive phase and amplitude errors due to magnetic field distortions	N,P,V	2013

N: Numerical, P :Phantom, V: In-vivo, C :ISMRM Challenge 2012

NLSQ : Non Linear Least Squares

1.3.3 Chemical-shift encoded imaging acquisition strategies

An important consideration for the acquisition strategy is the choice of echo times. Indeed, depending on the algorithms used, the acquisition scheme can be required to have a fixed number of echoes(67,80–84), equidistant echo time spacing(75,78) or specific echo times such as in/out-of phase(55,62). CSE-MRI sequences based on gradient echo or spin echo have been used to acquire data at multiple echoes times with whether single echo acquisitions repeated multiple times at different TEs or multi-echo acquisitions where multiple echo TEs are successively acquired for each TR (**Figure 1-8**).

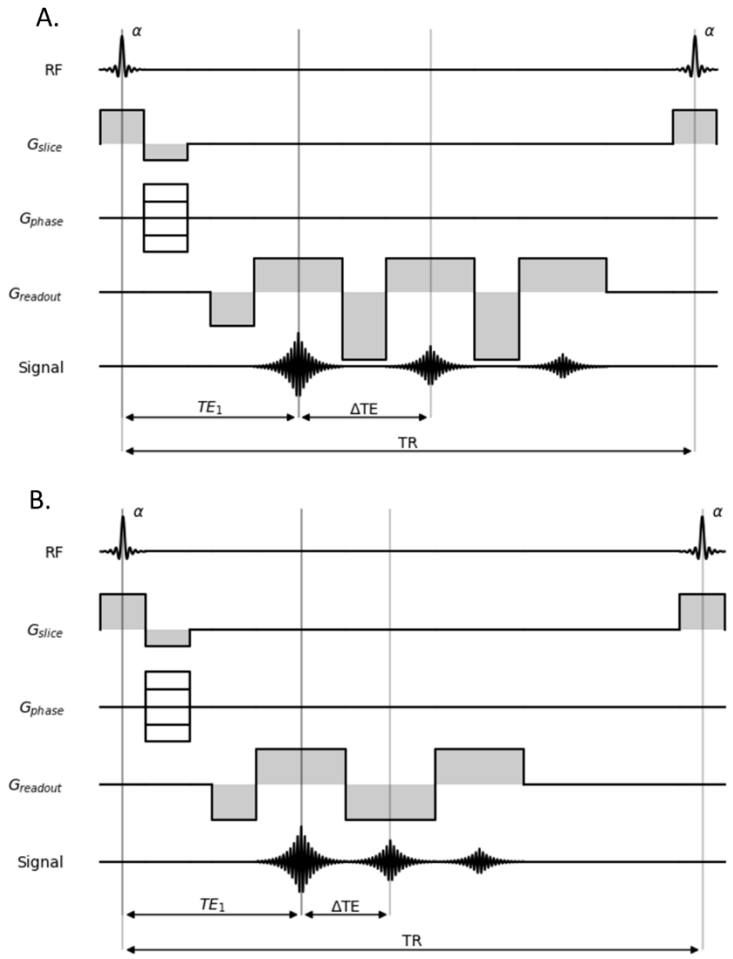

Figure 1-8: Multi-echo gradient echo (GRE) MRI sequence diagram using monopolar(A) and bipolar (B) readout gradients. RF: radiofrequency, α: flip angle, G_{slice} : slice select gradient, G_{phase} : phase encoding gradient, $G_{readout}$: frequency encoding

gradient, TE_1: first echo time, ΔTE: echo time spacing, TR: repetition time. MR sequence diagrams were generated using the mrsd toolkit(88).

The multi-echo acquisitions, more commonly used nowadays due to shorter scan time, can be categorized into monopolar or bipolar depending on the gradient readout. In monopolar mode, k-space trajectory is acquired in one way and there is a pause in data acquisition during the fly-back gradient. In comparison, in bipolar mode, k-space trajectory is acquired in two way thanks to alternative readout polarity allowing shorter echo spacing and therefore a shorter acquisition time. Bipolar readouts are more efficient than monopolar readouts but also more sensitive to inconsistent phase errors (89) due to system imperfections and eddy currents and require phase correction techniques. For more flexibility in the choice of echo times, interleaved multi-echo acquisitions could also be used.

1.4 Artificial intelligence dedicated to epicardial fat segmentation

In radiology for automatized the quantification of epicardial adipose tissue, different algorithms have been explored using atlas-based(90,91), active contours(52) and more recently deep learning approaches(53,92–94).

In this chapter, I will thus introduce basic notion of deep artificial neural networks by analyze in depth the most popular 2D segmentation for biomedical images(U-Net(95)) which is often the fundamental component of many state-of-the art segmentation cardiac MRI approaches.

U-Net is a fully convolutional neural network (FCN)(96), designs with an encoder-decoder structure (**Figure 1-9**). Given an input image, it learns high level feature representation though the encoder part. In the decoder part, it interprets those feature maps, gradually recovers spatial details back to the image space to produce k-class pixel-wise probabilistic map (layer in yellow) and assigns each pixel with the class of the highest probability to finally obtain the segmented mask. In the figure, the network would predict four regions: epicardial fat in blue, paracardial fat in green, heart ventricles in red and the background.

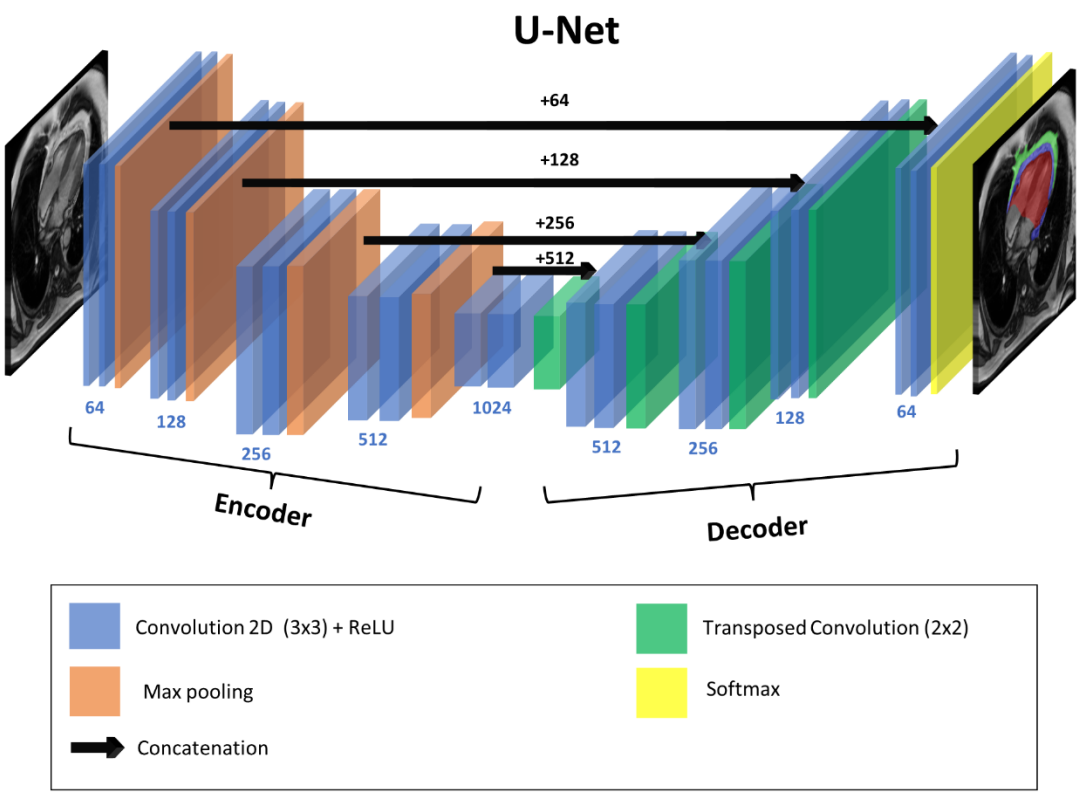

Figure 1-9 : Architecture of the Fully Convolutional Network U-Net.

The U-Net consists of a stack of functional layers including convolutional layer (in blue), down-sampling layer (in orange), up-sampling layer (in-green). The particularity of its network is to employ skip connections (black arrows) between the encoder and decoder to recover spatial information lost in down-sampling layers, resulting in a more precise segmentation.

As shown in **Figure 1-10**, a convolutional layer contains *n* convolution kernels which is followed usually by a normalization layer like batch normalization(97) (not shown here) and a non-linear activation function (e.g. ReLU) to extract *n* feature maps. The down-sampling layer decreases the size of those features maps, for multi-resolution features whereas the up-sampling layer (e.g transposed convolution) aims to increase the size of the output to reach back the size of the input image.

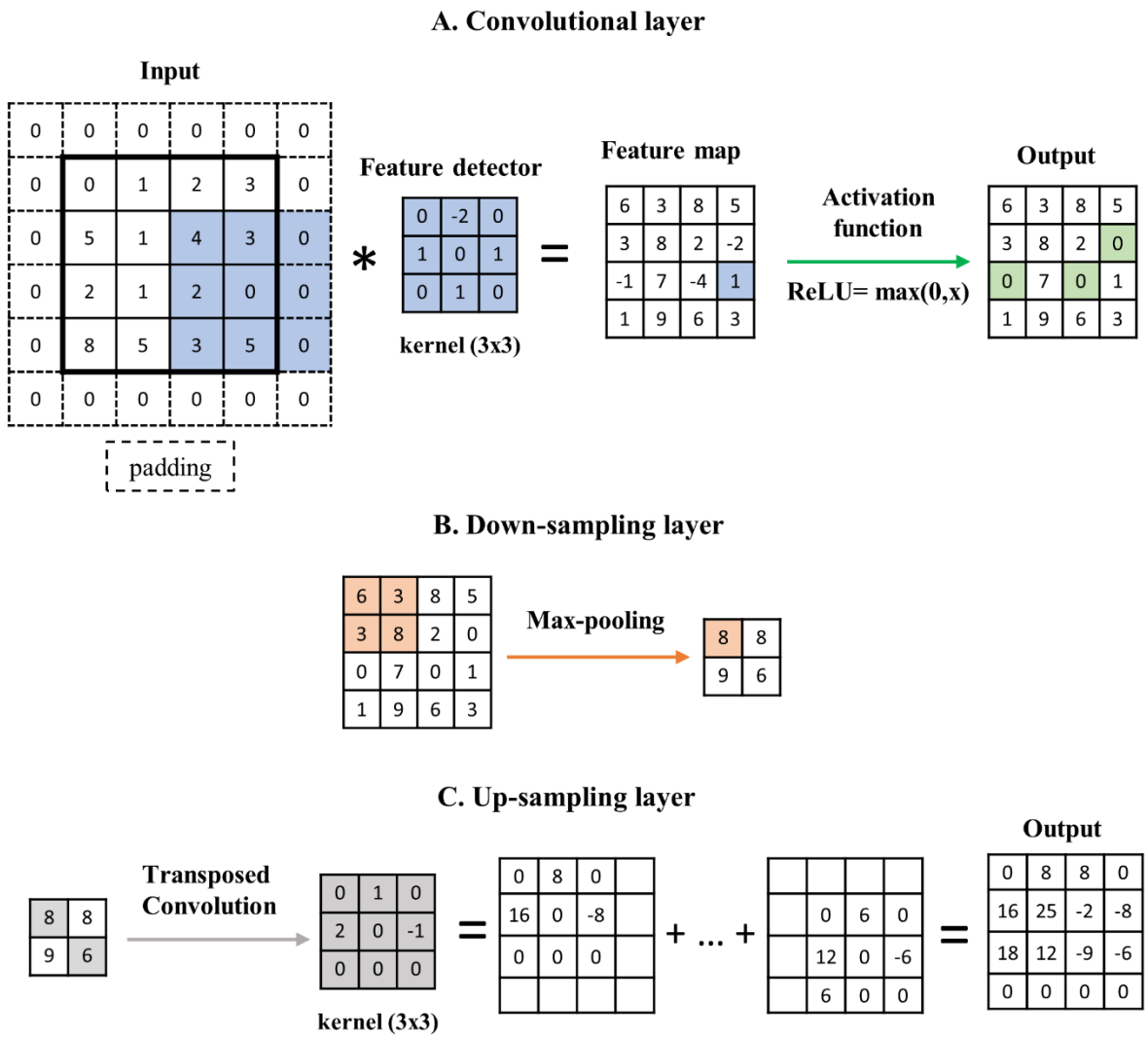

Figure 1-10: Outline of the different functional layers present in the U-net : the convolutional layer with activation function (A), the down-sampling layer(B), the up-sampling layer (C). Highlighted regions show the calculation process of each layer.

For supervised approaches, the neural network requires to be trained before it can be used it for its specific task (e.g. semantic segmentation). The standard training process requires to divide your dataset into 3 parts: training, validation, and test sets, that all contain paired images and manually segmented mask (ground truth labels). During the training, at each iteration, a loss function (e.g. cross-entropy loss) calculates the network's prediction error. This error is then used by an optimizer (e.g., stochastic gradient descent, Adam method(98)) to update network parameters (e.g. kernel weights) through backpropagation(99). The training's goal is to find optimal values that minimize the loss function but also avoid over-fitting (loss of generalization) of your training dataset.

Chapter 2 : Quantitative evaluation of epicardial fat overload from routine cardiac MRI

2.1 Synthesis

Context & motivation

In recent years, EAT is increasingly being recognized as a biomarker of risk of cardiovascular complication in multiple pathologies, most notably in diabetes and obesity. However, in cardiac MRI, EAT has often been overseen in diagnosis due to the limited spatial resolution to identify EAT and the corresponding time-consuming manual segmentation. Consequently, EAT quantification methods using MRI are still in their infancy compared to using Cardiac Computed Tomography (CCT) imaging where semi-automatic, deep-learning based approaches have already been well developed. To reduce the gap and facilitate analysis of EAT in MRI, this study proposed an automatic four-chamber area quantification using cine multi-frame Fully Convolutional Networks (FCN).

Methods & results

A retrospective mono-centric database with 100 subjects (including healthy controls, type-2 diabetic patients and non-diabetic obese patients), who underwent a CMR exam at 3T including full stack short-axis cine and four-chamber cine (4-Ch cine), was gathered to evaluate FCNs performance and the correlation between total EAT volume and 4-Ch cine EAT area. U-Net and FCN developed by Bai (noted FCNB) were optimized using 4-fold cross-validation (n=80) and evaluated on an independent dataset (n=20).

Our database showed a moderate correlation between EAT volume and four-chamber area (r = 0.77 and 0.74 in systolic and diastolic frame respectively). On the test dataset, networks performance was equivalent to inter-observers' bias (for EAT: DSCInter = 0.76, DSCU-Net = 0.77, DSCFCNB = 0.76). U-Net was better suited to provide EAT area estimation compared to FCNB.

Conclusion, limits & perspectives

The following chapter has been accepted as a full paper untitled Deep-Learning Segmentation of Epicardial Adipose Tissue Using Four-Chamber Cardiac Magnetic Resonance Imaging to Diagnostics on 29 December 2021. Beyond the publication, we decided to provide a publicly automatic EAT area segmentation that offers the possibility to quantitatively evaluate EAT on standard cardiac imaging, in both retrospective and prospective cardiac studies. However, those FCNs were trained and assessed only on a mono-centric database which limited its generalization across scanners, pathologies. Moreover, those approaches have shown limitations and the dynamic aspect of images has not been sufficiently exploited. The development of new kinds of FCNs based on temporal modules such as Convolutional Long Short-Term Memory (ConvLSTM)(100) could improve the accuracy of the automatic segmentation of this epicardial fat and be trained over a more generalized database such as the UK biobank(101). To strengthen models to clinical routine, data augmentation based on real MRI artifacts(102) and automatic evaluations of the network accuracy with a predicted quality score(103) is also important extension to this work.

After detection of patient at risk, it would be of interest to probe fatty acid profile EAT with a specific acquisition as EAT has been found to differ in composition between diabetic and non-diabetic patients(30).

Personal contributions

Before the deep-learning approaches investigation of this study, I have first explored non-supervised algorithms based on active contour to segment epicardial and paracardial fat. However, this approach did not succeed due to unsatisfying results and too many parameters to configure. That is why, I decided to study FCNs by training and optimizing over a retrospective database that I organized for facilitating the process. I performed a thorough review of FCN literature. In parallel, I followed on-line training (MOOC, Stanford machine learning class records) to reinforce my knowledge and be up to date in Deep-Learning. Upon completion of my training, I designed the networks dedicated to this study, and harvested the same database I had gathered from the previous experiments with active contours to train the two elected FCNs. I also conducted the statistical analysis, prepared all the figures, and drafted the paper.

Finally, once the study was complete and the manuscript was ready to be submitted, I integrated the optimized U-Net in FSLeyes plugin to facilitate its availability to the community.

2.2 Introduction

Epicardial adipose tissue (EAT) is a visceral fat depot surrounding the heart between the myocardium and the pericardium (18). Its volume quantification holds potential as a novel biomarker for risks of Coronary Heart Disease (CHD) (104). Pericardial fat, merging EAT and paracardial (PAT) fat, has been studied in the past in association with atherosclerotic disease (105) but these results have since been heavily criticized (106). The inclusion of two fats depots as one single entity may not reflect the separate functions and clinical implications of each adipose tissue. Indeed, recent studies focusing on separating EAT and PAT concluded that EAT alone was involved in the corresponding disease (107,108). Indeed, EAT is a metabolically active adipose tissue (18) compared to PAT. Its accumulation and subsequent inflammation add to cardiovascular risks, potentially impacting left ventricle (LV) diastolic dysfunction (8,109). Even more recently, EAT overload has raised concern as a risk factor in generalized inflammation from COVID-19 (110,111). It is now recognized that the amount of EAT is prospectively and independently associated with the number of coronary events in at-risk populations (112). Consequently, reproducibly quantifying EAT is a major public health objective aiming at a better identification of patients at high cardiovascular risk. EAT can indeed be visualized from standard cardiac Magnetic Resonance Imaging (MRI) images, but its analysis is currently not performed in clinical routine, because the necessary manual image segmentation is extremely time-consuming, and its measurement is not sufficiently standardized.

Different imaging modalities have been proposed to quantify EAT burden. Transthoracic echocardiography, forefront modality in cardiology, was used to measured EAT thickness on the free wall of the right ventricle (113). However only a single distance measurement was used to estimate EAT volume, strongly limiting the precision of this method because EAT is irregularly distributed around the heart. Cardiac Computed Tomography (CCT) imaging has become the gold standard for the quantification of EAT volume (114). In more recent studies, semi-automatic and deep learning methods have been implemented to achieve the EAT segmentation (93,115). However, the requirement of high spatial resolution CCT led to the use of elevated ionizing radiation doses, which could be a risk for patients' follow-up.

Cardiac MRI is a versatile tool than can measure cardiac function, morphology, perfusion and characterizes myocardial tissue in a single exam (116). Cardiac MRI is also highly sensitive to fat, which has long been considered as an obstacle for myocardial visualization. Cardiac fat remains under-appreciated as a diagnostic feature of cardiac MRI. To specifically probe fat around the beating heart with MRI, one can use a dedicated acquisition technique such as water-suppressed MRI (117) or Dixon MRI (3D) (118,119). Alternatively EAT volume may also be measured from a routine stack of short-axis cine images (46). EAT quantification is usually performed manually, which is a time-consuming and tedious task subjected to inter-observer variability. To help observers, first the cine temporal information could ease distinguishing EAT from paracardial fat. Indeed, EAT is attached to the myocardium and moves at pace with cardiac contraction and torsion, whereas PAT is only moderately pulled by the cardiac contraction and expansion. Second, while the pericardial fascia is not clearly visible on short axis views, which often reduced to a thin line that may be blurred by partial volume effects, on four-chamber (4Ch) views, the pericardium is generally less affected by partial volume effects resulting in better visualization. As such, the four-chamber view is recommended for evaluating pericarditis (120) and is a frequent choice of orientation to quantify EAT, PAT and pericardial fat(49–51,121–123). Consequently, the EAT analysis in this study were based on quantification of its 2D area representation in 4Ch long-axis cine MRI views. To address specifically this kind of segmentation challenges, deep learning approaches have recently bloomed. Indeed, fully automated methods applied on routine images, such as cine MRI, could be rapidly translated to the clinics. Bard et al.(121) developed a deep learning method to quantify pericardial fat in 4Ch long-axis cine MRI and evaluated it on the UK BioBank dataset. However, the segmentation of pericardial fat (EAT +PAT) limits the evaluation of the distinct roles and clinical implications of epicardial fat compared to paracardial fat.

Thus, we propose here to segment the thin EAT area on 4Ch cine MRI multi-frame images using state-of-the-art Fully Convolutional Networks (FCNs) for cardiac image segmentation, that were adapted to segment EAT, PAT and cardiac ventricles. A specific database of 4Ch cine MRI spanning diabetic, obese and healthy subjects was leveraged to train, validate, and evaluate proposed FCN networks.

2.3 Materials and Methods

2.3.1 Study Population

A retrospective mono-centric database was defined totaling 153 subjects, out of which 100 exams could be exploited. The 100 enrolled subjects including healthy controls, type-2 diabetic patients and non-diabetic obese were selected based on 4Ch orientation and the absence of severe artifacts as shown in **Figure 2-1**.

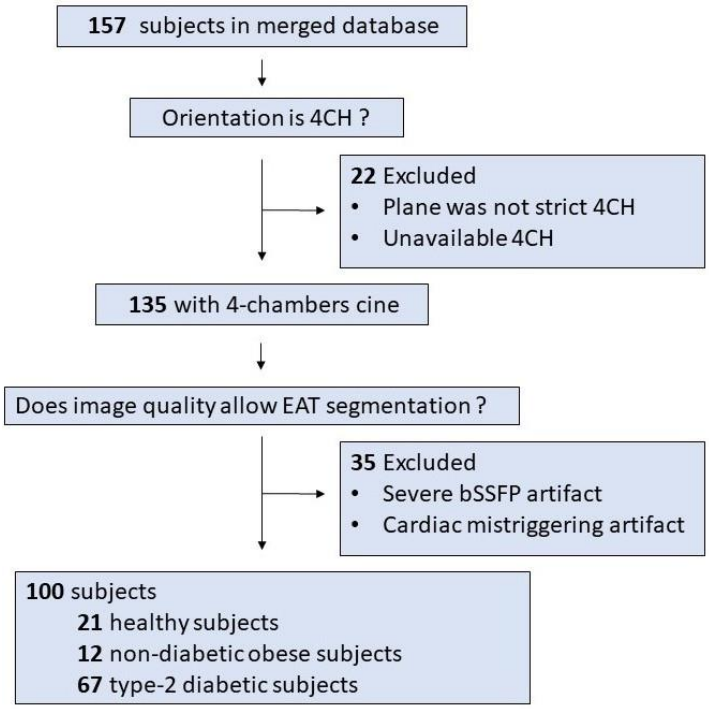

Figure 2-1.Overview of the study design

Patients were defined as having type 2 diabetes mellitus if they fulfilled any of the WHO criteria: HbA1c ≥ 6.5%, FBG level ≥ 7.0mmol/L, oral glucose tolerance test result ≥ 11.1mmol/L, or current treatment with antidiabetic agents. Obese non-diabetic patients were defined as the absence of any WHO criteria and a BMI ≥ 30 kg/m^2. All enrolled subjects had normal left ventricular function, no history of heart failure or coronary heart disease.

2.3.2 MRI acquisition

All subjects underwent cardiac MRI including the acquisition of a full stack of short-axis slices and a single slice four-chamber cine on a 3-T Siemens Verio system (Siemens Healthineers, Erlangen, Germany) with a dedicated cardiac 32-channel coil array (Invivo, Gainesville, FL, USA). The cine series were acquired with a retrospectively ECG-gated balanced steady-state free precession (bSSFP) sequence with in-plane image resolution varying from 1.3x1.3 mm^2 to 1.8x1.8 mm^2 (depending on subjects), slice thickness of 6mm, TE/TR=1.2/3.2ms, GRAPPA 2 (24 auto-calibration signal lines), temporal resolution of 28-35ms, with 25 frames reconstructed. Further details of the cardiac MRI protocols were previously described (46–48,124,125). N4 bias field correction (126) was applied to all image series before further processing.

2.3.3 EAT segmentation

For reference, EAT volume was segmented by expert readers provided with full stack short-axis series using Argus viewer (Siemens Medical Solutions, Erlangen, Germany). In an independent session, two expert readers were provided with full 4Ch series and performed blinded segmentation of 3 labels using the FSLeyes(127) viewer: heart ventricles (HV) (including both ventricle muscles and blood pools), epicardial (EAT) and paracardial (PAT) adipose tissues. EAT was defined as hyperintense signal within the pericardium around the ventricles. Peri-atrial fat was not included as it has been shown that peri-ventricle EAT alone had a stronger correlation with coronary diseases than total EAT(50). All isles of periventricular fat were included to form EAT area. PAT was defined as fat adjacent but outside the pericardium. Segmentations were performed on 3 cardiac phases determined by readers having the entire series at their disposal: first phase, peak systole and late diastole. The three segmented masks were propagated to the remaining frames using an automatic label propagation algorithm based on non-linear registrations, as previously described (128) resulting in 25 images segmented per subjects. Series in the test dataset were segmented by both readers, and reader 1 repeated blinded segmentations 6 weeks later.

2.3.4 Network architecture

Two different Fully Convolutional Networks (FCNs) were investigated: U-Net(95) with 48 filters for the first layer and FCN developed by Bai et al.(129) with 48 filters for the first layer, later referenced as FCNB. These networks are based on an encoder-decoder structure but differ in their decoder structure. The encoder part processes an image of arbitrary size as input and applies convolutional layers for extracting image features while the decoder upsamples and combines low-resolution featured map to the original input resolution. The absence of a dense layer allows these networks to process images of various sizes.

The U-Net(95) has been the most popular 2D segmentation network for biomedical images and a fundamental component of many state-of-the-art cardiac image segmentation approaches(130–132). The specificity of the U-Net is to employ skip connections between encoder and decoder to recover spatial information lost in downsampling layers as shown in **Figure 2-2**.

The second network investigated is the FCN developed by Bai et al.(129), later referred to as FCNB. FCNB has demonstrated excellent segmentation performances on the largest available cardiac MR dataset (UK-Biobank). Its specificity is based on the decoder that only consists of the concatenation of all featured maps, upsampled to the original resolution, as shown in **Figure 2-2.**

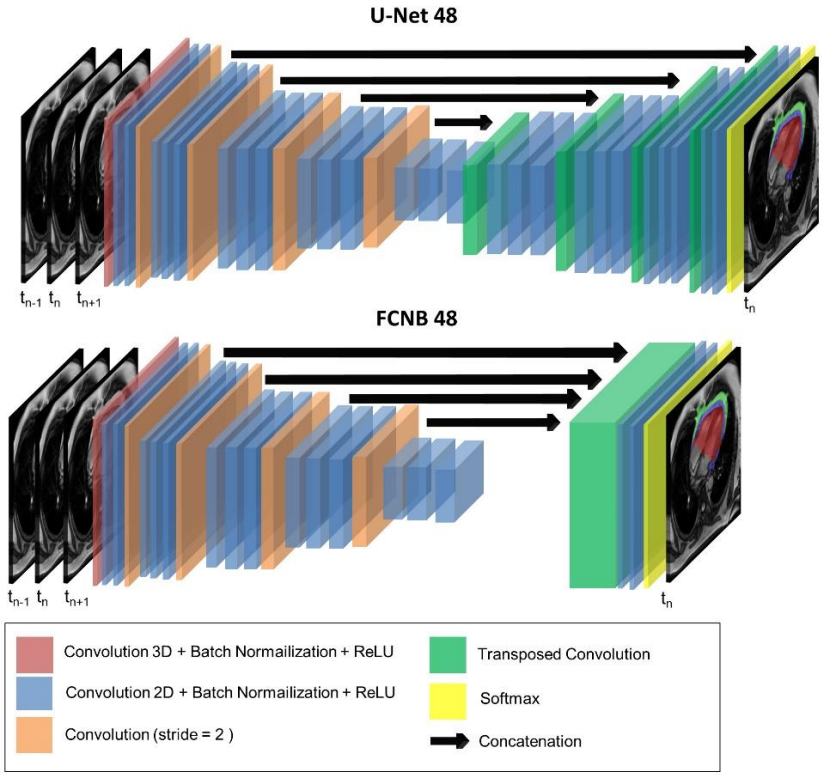

Figure 2-2. Networks' optimized architecture. The two networks evaluated in this study: U-Net and fully-convolutional network (FCNB) architectures included a first 3D convolution layer to allow multiple cardiac frames as input. Following 2D convolution layers encoded images from 48 features up to 768 features. Eventually, the decoder targeted 3 labels for segmentation in the central input frame: epicardial adipose tissue (EAT), paracardial adipose tissue (PAT) and heart ventricles (HV)

In their original papers, the cross-entropy loss was used to train those networks. However, this loss has shown limits to address class imbalance. In our study, regions of interest (ROI) were sparsely represented compared to the background and cross-entropy loss is inadequate to handle it. Thus, the loss function was defined as the mean dice between the probabilistic label map without background and the manually annotated label map.

2.3.5 Training

Specifically, optimized FCNB and U-Net were trained on 3 consecutive cine frames for segmentation of the central frame, providing a crucial temporal information often

necessary for the experts to segment EAT. Input images were normalized to the range of [0,1] with fixed size (256x192x3), mask zero-padding or cropping was applied when needed.

For each batch (N=30), on-the-fly data augmentation was performed using rotational transformation and/or image scaling before feeding them to the network. Both data augmentation were set using a random clipped normal distribution spanning from -30°/0.4 up to 30°/1.6 for rotational transformation and image scaling respectively. The Adam optimization(98) was used for minimizing the dice loss function with a constant learning rate of 1e-3. It took approximatively 35 minutes to train either the U-Net or FCNB on a *Graphics Processing Unit* (GPU) (NVidia Tesla K80).

The networks investigated were implemented using Python within the TensorFlow 2 framework. The FCNB model was adapted from the original implementation(133), whereas U-Net was custom-designed. To adapt to the proposed multi-frame approach, both 2D networks were modified to accept 2D+t inputs, considering the cardiac time dimension as a 3rd dimension with limited horizon. Thus, the first convolution layer of each network was replaced with a 3D convolution layer with valid padding. The following layers were kept identical, processing extracted features independently of the input dimensions.

To perform a robust evaluation, networks were trained using cross-validation and evaluated on an independent dataset: the database was split in 5 subsets (500 images / 20 subjects each reflecting our database populations distribution: 4 healthy controls, 13 type 2-diabetics, 3 nondiabetic obese patients). One subset (500 images) was used as a test set whereas the 4 other subsets were used for stratified cross-validation training, resulting in a 4-fold cross-validation. Thus, a single subset is retained as validation (500 images) whereas the 3 others (1500 images) are used for training, ensuring that validation and training dataset reflects the database population distribution.

2.3.6 Evaluation metrics

Segmentation performances were evaluated for accuracy, propinquity, and surface estimation error. Dice similarity coefficient (DSC) measured segmentation accuracy from the overlap between the manual and automatic segmented surfaces (S_M and S_A), defined as:

$$DSC = 2\,\frac{S_M \cap S_A}{S_M + S_A}$$

The Mean Surface Distance (MSD) calculated the propinquity between segmentations as is the mean distance (in mm) between segmented contours, defined as:

$$MSD = \frac{1}{n_M + n_A}\left(\left(\sum_{k=1}^{n_M} d(k, S_A))\right) + \left(\sum_{k=1}^{n_A} d(k, S_M)\right)\right)$$

To evaluate the clinical final purpose, which is the quantitative measurement of EAT area, Absolute Relative Surface Error (RSE) was utilized, defined as:

$$RSE = \frac{|S_M - S_A|}{S_M}$$

To further assess accuracy, positive predicted value (PPV) which is an indicator of over-segmentation (PPV << 1) was calculated on the entire database, defined as:

$$PPV = \frac{S_M \cap S_A}{S_A}$$

2.3.7 Statistical analysis

Statistical analysis was conducted using R (version 3.6.3) (134). Analysis of linear regression was used to study the correlation between manually evaluated EAT volume and 4Ch area. The metrics' distribution normality was assessed using the Shapiro-Wilk test. Wilcoxon signed rank and Wilcoxon rank sum tests were used to investigate significant differences for each metrics between intra-inter observers and FCNs. To account for segmentation difficulty and clinical relevance (26) that scale with the quantity of EAT, networks' performances were assessed per quartile of manually segmented EAT area ($Q_1 < 8.22\ cm^2 \leq Q_2 < 12.70\ cm^2 \leq Q_3 < 15.55\ cm^2 \leq Q_4$).

2.4 Results

The selected 100 subjects were divided into three groups (21 healthy controls, 67 type-2 diabetic patients and 12 non-diabetic obese patients) as detailed in **Table 2-1**.

Table 2-1. Study population clinical characteristics.

	Healthy	Non-diabetic obese	Type-2-diabetic
Clinical characteristics			
Number of participants	21	12	67
Age, years	25 ± 10	41 ± 13	53 ± 10
Gender: female, n (%)	11 (52)	10 (83)	41 (61)
BMI, kg/m^2	21.9 ± 2.6	40.8 ± 5.9	35.6 ± 6.8
T2D			
Duration of diabetes, years			8±6
Cardiovascular risk factors, n (%)			
Hypertension	6 (29)	1 (8)	32 (48)
Dyslipidaemia	2 (10)	1 (8)	36 (54)
Current Smoker, n (%)	3 (14)	1 (8)	8 (12)

In studied database, EAT volumes spanned a wide range from 29 to 376 cm^3, defining quartiles by: $Q_1 < 77.8$ cm$^3 \leq Q_2 < 94.6$ cm$^3 \leq Q_3 < 114.3$ cm$^3 \leq Q_4$.

Corresponding EAT areas as measured on 4Ch views correlated well with total EAT volume measured from the stack of short-axis cine (**Figure 2-3**) with a slightly higher correlation in systole (Pearson r = 0.77) than in diastole (Pearson r = 0.74). Thus, a wide range of EAT 4Ch areas was available from 1.2 cm^2 to 37.2 cm^2, with a lower range for healthy subjects from 2.5 to 13.7 cm^2, from 1.2 cm^2 to 23.2 cm^2 for non-diabetic obese subjects and from 5.3 cm^2 to 37.2cm^2 for type 2 diabetic patients.

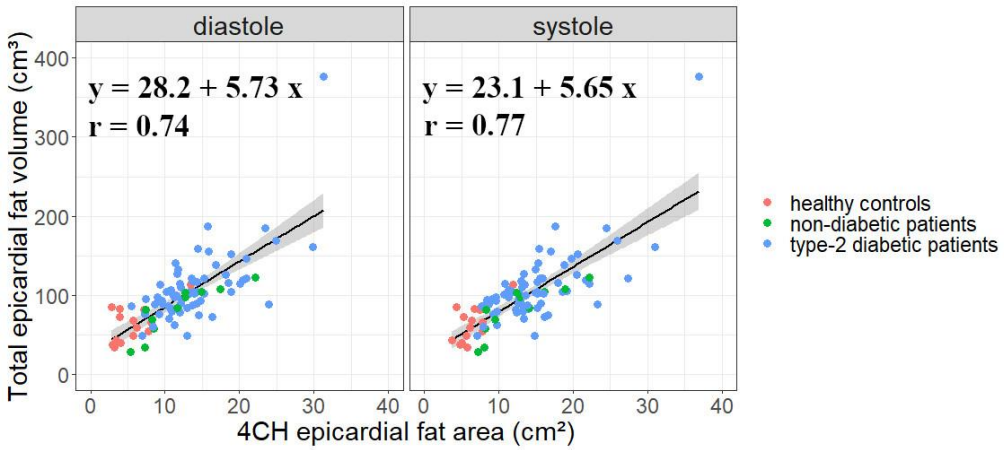

Figure 2-3. Comparison of reference total epicardial fat volume and proposed EAT area measured on four-chamber cine. EAT area was measured in end-systolic or end-diastolic frame across the 100 subjects' database. The three cohorts merged for the database were identified by markers color.

As shown in **Table 2-2**, intra and inter-observer DSC confirmed excellent reproducibility for HV segmentation (DSC_{Intra}= 0.98 and DSC_{Inter}= 0.96 resp.). EAT and PAT differed between the two observers (DSC_{Inter}= 0.76 and 0.78 for EAT and PAT resp.), although segmentations performed twice by the same observer proved to be more reproducible (DSC_{Intra}=0.83 and 0.85 for EAT and PAT resp.). Intra-observer DSC and MSD were significatively lower ($p<0.05$) concerning EAT segmentation in the diastolic frame compared to the segmentation in the systolic frame. For inter-observer bias, differences in DSC, MSD or RSE metrics were not statistically significant between diastolic and systolic frames.

FCNB and U-Net segmentations performance measured by DSC, were significantly lower ($p<0.05$) than intra-observer bias for all labels (for EAT: DSC_{Intra} = 0.83, $DSC_{U\text{-}Net}$ = 0.77, DSC_{FCNB} = 0.76). Both networks provided equivalent DSC, MSD and RSE performance than inter-observer bias for all labels (for instance PAT: DSC_{Inter} = 0.78, $DSC_{U\text{-}Net}$ = 0.80, DSC_{FCNB} = 0.78).

Table 2-2 : Mean values and standard deviations of segmentation results on the test set.

	DSC				MSD (mm)				RSE (%)			
	Intra	*Inter*	*U-Net*	*FCNB*	*Intra*	*Inter*	*U-Net*	*FCNB*	*Intra*	*Inter*	*U-Net*	*FCNB*
PAT	0.85 ±0.06	0.8 ±0.09	0.80 ±0.08	0.78 ±0.10	1.15 ±0.63	2.08 ±1.49	2.38 ±1.78	2.29 ±1.47	11.78 ±8.09	20.43 ±18.77	14.29 ±10.44	17.43 ±17.50
EAT	**0.83 ±0.07**	**0.76 ±0.10**	**0.77 ±0.07**	**0.76 ±0.07**	**1.53 ±1.32**	**2.65 ±2.98**	**1.71 ±1.06**	**2.06 ±1.96**	**13.02 14.59**	**17.67 ±15.07**	**20.33 ±15.70**	**20.97 ±15.66**
EAT+PAT	0.90 ±0.04	0.88 0.05	0.88 ±0.06	0.88 ±0.06	1.12 ±0.66	1.55 ±0.07	1.36 ±0.90	1.60 ±1.28	6.92 ±7.16	9.20 ±6.80	7.36 ±9.40	8.92 ±12.97
HV	0.98 ±0.01	0.96 0.02	0.97 ±0.02	0.96 ±0.03	0.96 ±0.5	1.88 ±2.24	1.33 ±0.79	1.42 ±0.89	2.33 ±2.20	3.69 ±3.18	3.88 ±4.46	4.22 ±5.80

Metrics are reported as mean values ± standard deviation.

Systole and diastole segmentations were not differentiated in these metrics.

PAT : Paracardial Fat, EAT : Epicardial Fat, EAT+PAT: Pericardial Fat, HV : Heart ventricles

DSC : Dice similarity coefficient, MSD :Mean Surface Distance RSE : Absolute Relative Surface Error

Across the 4 quartiles of data defined by equally populated ranges of EAT areas, both networks provided reliable segmentation of the heart ventricles (HV, FCNB: $DSC_{Q1\text{-}Q4}$ = 0.97-0.96, U-Net: $DSC_{Q1\text{-}Q4}$ = 0.97) as shown in **Table 2-3**. Interestingly, the network performances to segment EAT strongly depended on the population quartile. Indeed, U-Net DSC was significantly higher ($p<0.001$) for upper quartiles as observed using U-Net: $DSC_{Q4} = 0.83 > DSC_{Q3} = 0.80 > DSC_{Q2} = 0.76 > DSC_{Q1} = 0.69$ as illustrated in **Figure 2-4**. DSC and RSE metrics demonstrated a gap of segmentation quality between the lower two quartiles and the upper two quartiles for both PAT and EAT segmentation (for EAT FCN: $RSE_{Q4} = 15.60$, $RSE_{Q3} = 15.87 < RSE_{Q2} = 21.91 < RSE_{Q1} = 27.98$). Across all quartiles, both networks had more difficulty separating PAT from EAT than identifying total pericardial fat (EAT+ PAT) in the image (with U-Net, $RSE_{EAT+PAT} << RSE_{EAT}$ or RSE_{PAT} for all quartiles).

Over the database and for all labels, U-net outperformed ($p<0.0001$) FCNB for segmenting accurately (DSC), nearer to the ground truth (MSD) and thus providing a more reliable (i.e. accurate) measurement (RSE).

Table 2-3. DSC, MSD, RSE metrics evaluated per quartile (Q1-Q4) of EAT area for U-Net and FCNB.

Q1	**DSC**		**MSD (mm)**		**RSE (%)**	
	U-Net	*FCNB*	*U-Net*	*FCNB*	*U-Net*	*FCNB*
Paracardial Fat (PAT)	0.55	0.53	5.82	5.69	36.21	38.54
Epicardial Fat (EAT)	**0.69**	**0.67**	**2.14**	**2.21**	**22.15**	**27.98**
Pericardial Fat (EAT+PAT)	0.78	0.77	1.60	1.78	2.08	2.65
Heart ventricles (HV)	0.97	0.97	1.12	1.35	12.59	16.19
Q2	**DSC**		**MSD (mm)**		**RSE (%)**	
	U-Net	*FCNB*	*U-Net*	*FCNB*	*U-Net*	*FCNB*
Paracardial Fat (PAT)	0.76	0.75	2.68	2.82	17.29	20.83
Epicardial Fat (EAT)	**0.76**	**0.74**	**1.22**	**1.53**	**17.85**	**21.91**
Pericardial Fat (EAT+PAT)	0.87	0.87	1.16	1.35	7.55	8.60
Heart ventricles (HV)	0.97	0.97	1.11	1.65	2.57	3.04
Q3	**DSC**		**MSD (mm)**		**RSE (%)**	
	U-Net	*FCNB*	*U-Net*	*FCNB*	*U-Net*	*FCNB*
Paracardial Fat (PAT)	0.82	0.82	2.26	1.99	12.72	12.14
Epicardial Fat (EAT)	**0.80**	**0.79**	**1.30**	**1.47**	**13.49**	**15.87**
Pericardial Fat (EAT+PAT)	0.90	0.90	1.37	1.43	5.86	5.28
Heart ventricles (HV)	0.97	0.97	1.08	1.50	2.54	3.07
Q4	**DSC**		**MSD (mm)**		**RSE (%)**	
	U-Net	*FCNB*	*U-Net*	*FCNB*	*U-Net*	*FCNB*
Paracardial Fat (PAT)	0.80	0.78	2.46	3.12	13.65	16.72
Epicardial Fat (EAT)	**0.83**	**0.79**	**1.40**	**2.06**	**11.72**	**15.60**
Pericardial Fat (EAT+PAT)	0.91	0.90	1.40	1.84	5.64	6.43
Heart ventricles (HV)	0.97	0.96	1.31	2.60	3.20	4.52

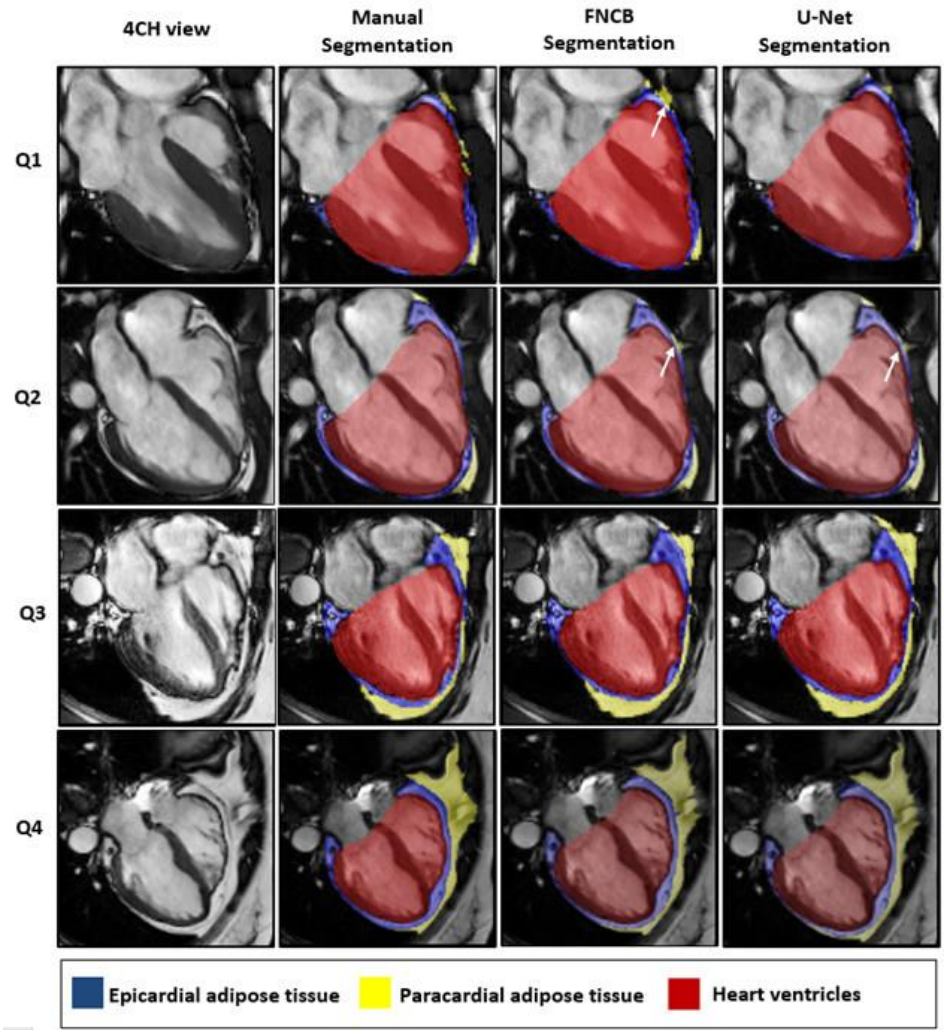

Figure 2-4. Representative segmentation results for each population defined by quartile of EAT area. Images were cropped around the heart for visualization. White arrows point out discrepancies between manual and automatic segmentations. As detailed in the methods, only periventricular EAT was segmented.

FCNB and U-net performed significantly better ($p<0.05$) for segmenting EAT area on the systolic frame compared to the diastolic frame ($DSC_{UNet\text{-}diastole} = 0.76$ $DSC_{UNet\text{-}systole} = 0.80$). These differences were not significant in PAT (see **Supportive Information Figure S 2-1**).

Classification of our database split by quartile of EAT burden was observed by confusion matrices. From **Figure 2-5**, the confusion matrices diagonal (in green) gave a measure of correct classification (66 % for FCNB and 71% for U-Net), whereas the subdiagonal and the superdiagonal (in yellow) allowed evaluating a misclassification by

one quartile (32% for FCNB and 27% U-Net) and the 2nd subdiagonal and superdiagonal (in red) gave an estimate of a misclassification by two quartiles (2 % for FCNB 2% for U-Net). As shown by subdiagonal confusion matrices and confirmed by PPV, FCNB significantly over-estimated EAT area compared to U-Net ($PPV_{FCNB} = 0.73 < PPV_{U\text{-}Net} = 0.75$, $p<0.0001$).

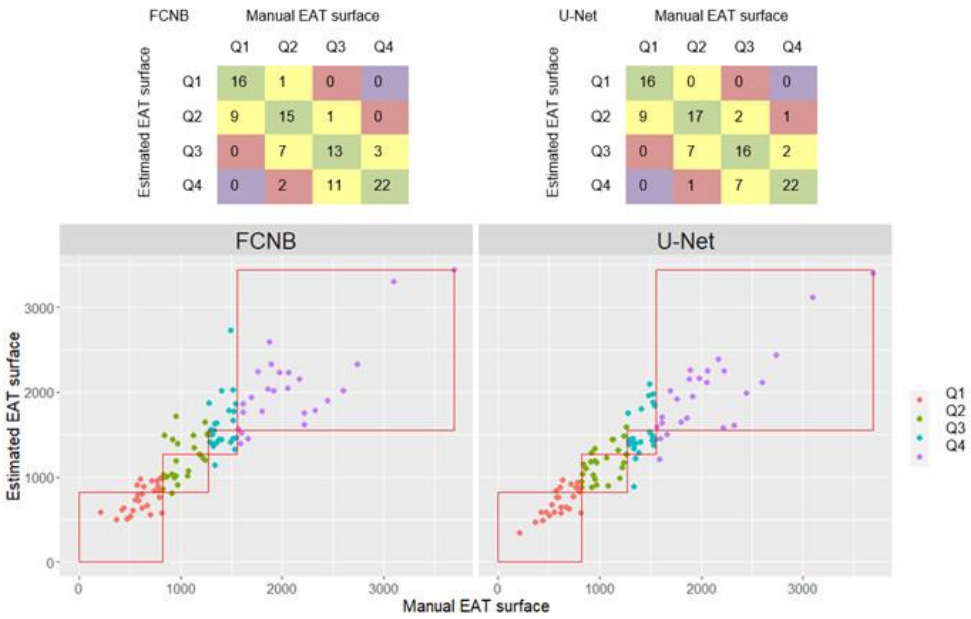

Figure 2-5. Quartile classification results from EAT area estimated from networks segmentation against classification from manual EAT area. Only segmentations from preferred systolic frames were shown here.

2.5 Discussion

This study aimed at providing a rapid and fully integrable evaluation of epicardial fat burden. To achieve this evaluation, automated segmentation of the EAT layer was performed on four-chamber cine MRI series using Deep Learning approaches.

2.5.1 Four-chamber-view intrapericardial fat area is a relevant measure of EAT

Confirming previous literature (49,122), the correlation found in this work between EAT area and volume across a wide range of EAT volumes (from 29 to 376 cm^3) comforted the relevant use of four-chamber EAT area as a rapid but realistic measure of EAT burden. Already in past studies, the 2D EAT area has been linked to left ventricular diastolic

dysfunction (50,51), hypertension and severity of insulin resistance (122) and non-alcoholic fatty liver disease patients (123). Thus, four-chamber view holds potential as a surrogate to quantify EAT in routine clinical practice. Moreover, in four-chamber view, the pericardium beyond the apex of the heart could be visualized with more reliability. However, our database gathered retrospective studies in which EAT volume segmentation had been measured in short-axis views by different investigators over the years, which could lead to unaccounted volume imprecision. Ideally, the gold standard CCT EAT volume quantification would have been preferred but this examination is not commonly indicated for metabolic patients.

2.5.2 A specific database with possible extensions

This work leverages a unique database that combines a population spanning a large range of EAT quantity and manual segmentation of EAT on cine series. The strength of our dedicated database stands in its diversity in BMI, sex, age, health condition across many subjects (n=100) (**Table 2-1**). Despite a large diversity of subjects, a disparity of age remains between younger healthy subjects and diabetic and/or obese patients. The addition of data from older healthy subjects, as well as elderly subjects (>65 years) would benefit the current database to reinforce our network training as elderly have been shown to be significantly more EAT burdened than younger individuals (135). Our database could also be extended by including image sets from different MRI scanner types. Currently, this is a monocentric study and database. As a result, the trained models might not adapt well on datasets from scanners of different vendors and field strengths. Nevertheless, the database was made up of multiple protocols acquired over a decade, which already featured a variety of acquisition parameters and image quality levels. To further leverage the number of annotated data (2500 ground-truth, 25 images segmented per subject), Generative Adversarial Network could be explored to extend beyond proposed data augmentation (136). Another challenge are recurrent artifacts (aliasing, dark bands, flux artifacts) commonly observed in 3T bSSFP cine-MRI images, particularly pronounced in obese patients. This might preclude EAT segmentation and disturb networks accuracy. Training networks on artifacted images is another important addition to strengthen models for them to be ready for the clinic.

2.5.3 The challenge of EAT segmentation

Experts and networks provided excellent results on large structures such as Heart Ventricles (DSC ≥ 0.96) and pericardial fat (DSC ≥ 0.88). But one major challenge for the segmentation of EAT on cine MRI is to distinguish between burdening EAT and its extra-pericardial neighbor PAT. The pericardial fascia that separates those two fat compartments is about 2 mm thick (137,138) which is of the same order of magnitude as the image resolution (1.3-1.8 mm). This explains why both networks were able to segment combined EAT+PAT pericardial fat with appreciable precision, but the identification of individual fat was less satisfying. Nevertheless, FCNs networks provided segmentation results on par with experts' precision. Also, since cardiac contraction pulls onto the pericardium, its visualization improves in peak-systole(51), making this frame more suitable for the measurement of EAT when compared to diastole (p_{intra}(DSCdia/DSCsys)= 0.0282).

One novelty has been to input multiple cardiac frames from the cardiac cycle to networks using a 3D first convolutional layer. It could be interesting in future work to enhance temporal information which is essential to detect the pericardial fascia. A map of cardiac deformations could enhance input images to be supplied to the network. It would be also interesting to investigate other network architectures such as Recurrent Neural Network that could memorize information from adjacent slices to improve inter-slices coherence (139), but these extensions fall outside the scope of this work.

2.5.4 Comparing FCNs performances

Specific complementary metrics (DSC, MSD and RSE) have been chosen to evaluate EAT area segmentation and quantification. Alternatively, the Hausdorff distance metric is a common choice to evaluate segmentation performance(140), measuring the maximal pixel distance error between segmentations. However, EAT region is sparsely distributed around the heart, thus the Hausdorff distance was not considered in this work since it might range rapidly high, even when comparing two segmentations with similar areas.

From chosen metrics, U-Net outperformed FCNB for all labels, thus appearing preferrable to quantify EAT 4Ch area. Alternative semi- and fully automatic methods have been proposed for the EAT quantification on MRI-cine. Cristobal-Huerta et al. (52)

developed an automatic pipeline composed of Law texture filters, snakes and K-cosine curvature analysis to partially quantify EAT volume, albeit on 10 subjects only. In a semi-automatic processing, Fulton et al. (53) applied landmarks on short-axis images from 12 subjects to unroll images into polar coordinates before employing a neural network for detection of epicardial fat contours. We were unable to compare our results with those previous works as segmentation metrics (e.g., DSC metric or Jaccard similarity index) were not provided. Recently, automatic total pericardial fat quantification has been developed in 4Ch cine MRI. Bard, Raisi-Estabragh et al. (121) obtained segmentation performances ($DSC_{EAT+PAT}$ = 0.8) very similar to ours ($DSC_{EAT+PAT}$ = 0.88) on their respective test-set. In their study, only the end-diastolic frame had been segmented while we segmented the full 4Ch cine MRI and trained on 3 consecutive cine frames to leverage cine temporal information. Finally, the optimized multi-frame U-Net was integrated in a FSLeyes plugin made available to the community (https://github.com/pdaude/fsleyes-plugin-epicseg) allowing comparison with further work and providing clinicians with a rapid EAT area segmentation (see **Supportive Information Figure S 2-2**).

2.5.5 Performances across quartiles

Splitting the database in quartiles of EAT enabled to differentiate segmentation performances depending on EAT area. Indeed, segmentations quality from FCNs proved to be degraded in group Q1, in which EAT (as well as PAT) was thin and sparse as illustrated in **Figure 2-4**. However, EAT segmentations were on a par with inter-observers' manual segmentation for the three upper quartiles and remained relevant for identifying patient at risk (Q_2, Q_3, $Q_4 \geq 8.22$ cm^2) by measuring their EAT burden within 14% and 18% precision for U-Net and FCNB respectively.

2.6 Conclusions

This study provides a methodology for fully automated segmentation of epicardial fat on multi-frame cardiac cine MRI, demonstrated across one hundred subjects exhibiting low to high EAT quantities. EAT is often overseen in diagnosis but has received increasing attention as a relevant biomarker of cardiac risk. Automatic EAT evaluation could help to identify patients at risk, especially for diabetic patients. The comparison with EAT volume

supports the potential of four-chamber cine EAT area as a surrogate for clinical evaluation, with higher segmentation robustness in systolic frame. Between the two FCNs investigated, the optimized U-Net was better suited to provide EAT area estimation with a 14.2 % precision for the clinically-relevant upper three quarters of targeted EAT range. EAT evaluation on cine, leveraging multi-frame information, could be further integrated to explore both retrospective and prospective cardiac studies without the need of a specific acquisition thanks to publicly provided automatic EAT area segmentation.

2.7 Supportive Information

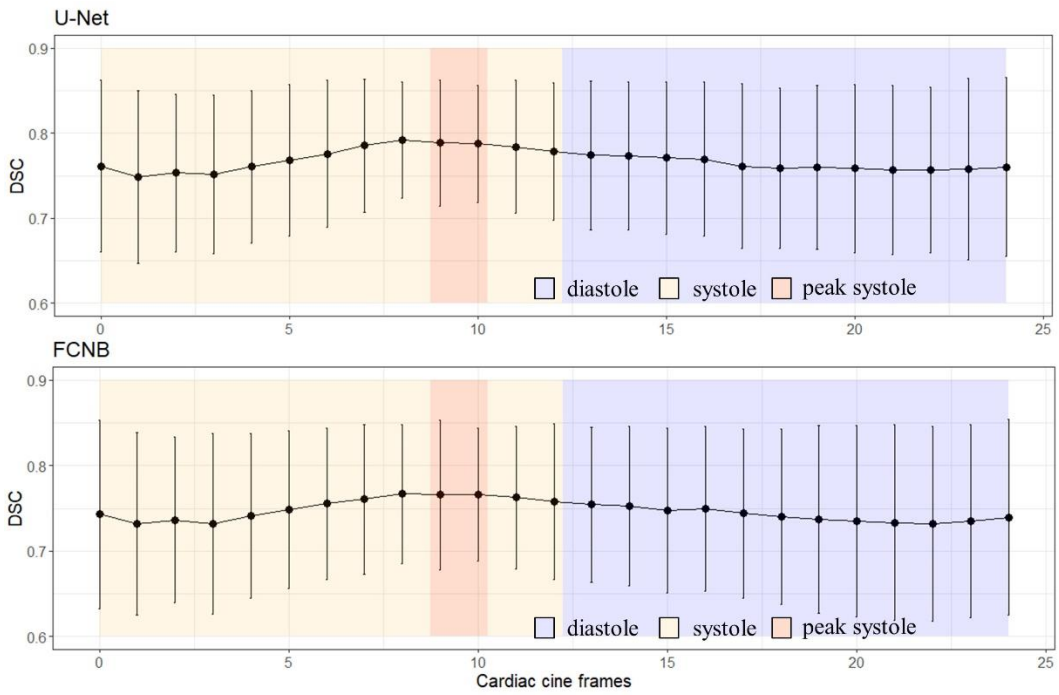

Supportive Information Figure S 2-1: FCNs DSC performance varies along the cardiac cine frames with a maximum mean Dice and minimum standard deviation in systole.

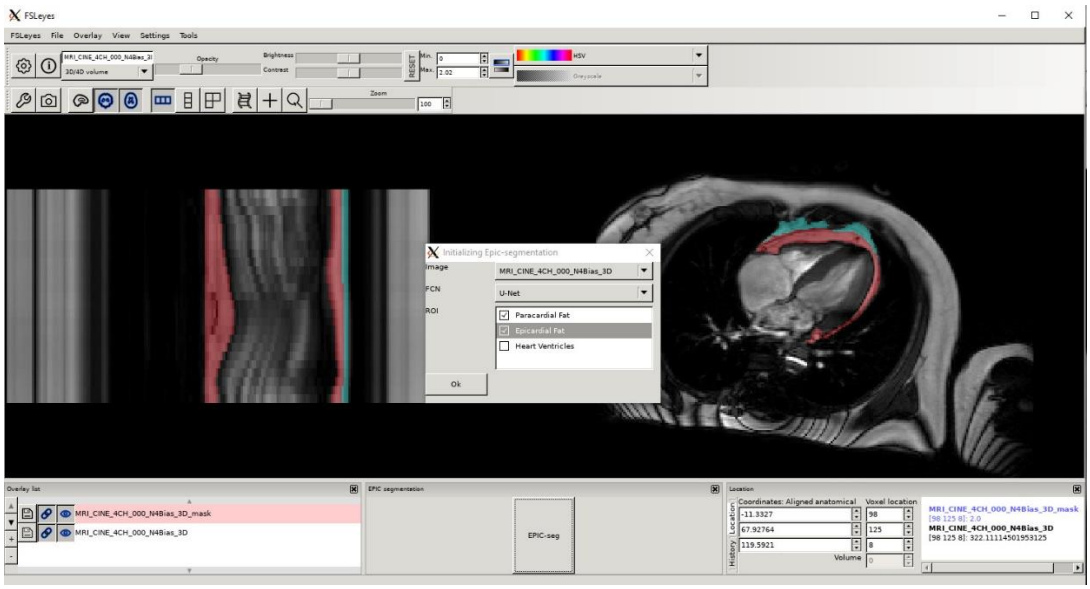

Supportive Information Figure S 2-2 : FSLeyes plugin interface for epicardial and paracardial segmentation will facilitate reproducibility of proposed methods.

Chapter 3 : Fat precision imaging using CSE imaging

3.1 Synthesis

Context & motivation

Proton density fat fraction (PDFF) is non-invasive biomarker to assess tissue adiposity. To obtain this quantitative biomarker, numerous fat water signal separation algorithms have been developed with a diversity of methods and implemented in different programming language. We needed to select one of them with criteria based on precision and reliability to process our CSE-MRI data. However, it has been a decade since the last benchmark of those algorithms. Indeed, during 2012 ISMRM Fat-Water MRI Workshop, a challenge has been organized to compare state of the art algorithms on a multitude of in-vivo datasets and a MATLAB toolbox has been developed for facilitate future comparison. It was necessary to renew this comparison with the state of the art open-source algorithms with numerical simulations to have an extensive exploration, evaluation and validation and extend the toolbox considering other programming language and the diversity of fat spectrum model. Thus, in accordance with this PDFF standardization, the purpose of this study was to implement a multilanguage numerical toolbox for addressing the performance of open-source fat-water separation algorithm.

Methods & results

An open-source toolbox implemented in MATLAB and Python was developed to assess performance of recent fat-water separation methods. Synthetic CSE-MRI volumes were simulated with a full range of PDFF, a large range of B_0 varying in terms of echo times, echo spacings and SNR. For in vitro validation, homemade fat water phantom was acquired at 3T with the same acquisition parameters as simulation. Challenging in-vivo data in terms of large variation of B_0 inhomogeneities, large echo-spacing and low SNR was also acquired to illustrate performance of the algorithms.

Monte-Carlo simulation and in-vitro experiments highlighted that algorithms proved to be robust fat/water swaps and B_0 offset only with 5 echoes and more. However, for

PDFF quantification with 7 echoes and SNR=50, two methods proved to still be inaccurate whereas two others provided PDFF precision dependent of the echo spacing scheme (*P<0.05)* and the remaining 4 ones provided similar performance with a bias <0.15. The choice of fat spectrum model influenced PDFF and severely R_2^* quantification.

Conclusion, limits & perspectives

This benchmarking using a bi-language open-source toolbox offers the possibility to better appreciate recent fat-water separation algorithms precision and accuracy for PDFF and R_2^* quantification. It could also allow to optimize acquisition parameters by predicting margins of errors of algorithms. It would have been of interest to have a larger diversity of method which is based on MRI vendors algorithms, magnitude based model or artificial intelligence algorithms, as they are becoming increasingly present in this field. This toolbox will greatly improve from in-vitro, in-vivo multi-vendor, multi-field data in order to better validate algorithms. Moreover, algorithms have started to include refined Dixon-MRI signal model, designed for quantitative fatty acid composition parameter mapping(36,59). This toolbox could be extended to explore precision and reliability of estimation of those parameters using extensive in-silico acquisition parameter set. Indeed, synthetic magnitude Dixon-MRI signal with realistic variations of triglyceride parameters (CL, ndb, nmidb) which are linked to fatty acid composition revealed influence on the signal at specific echo times (**Figure 3-1**).

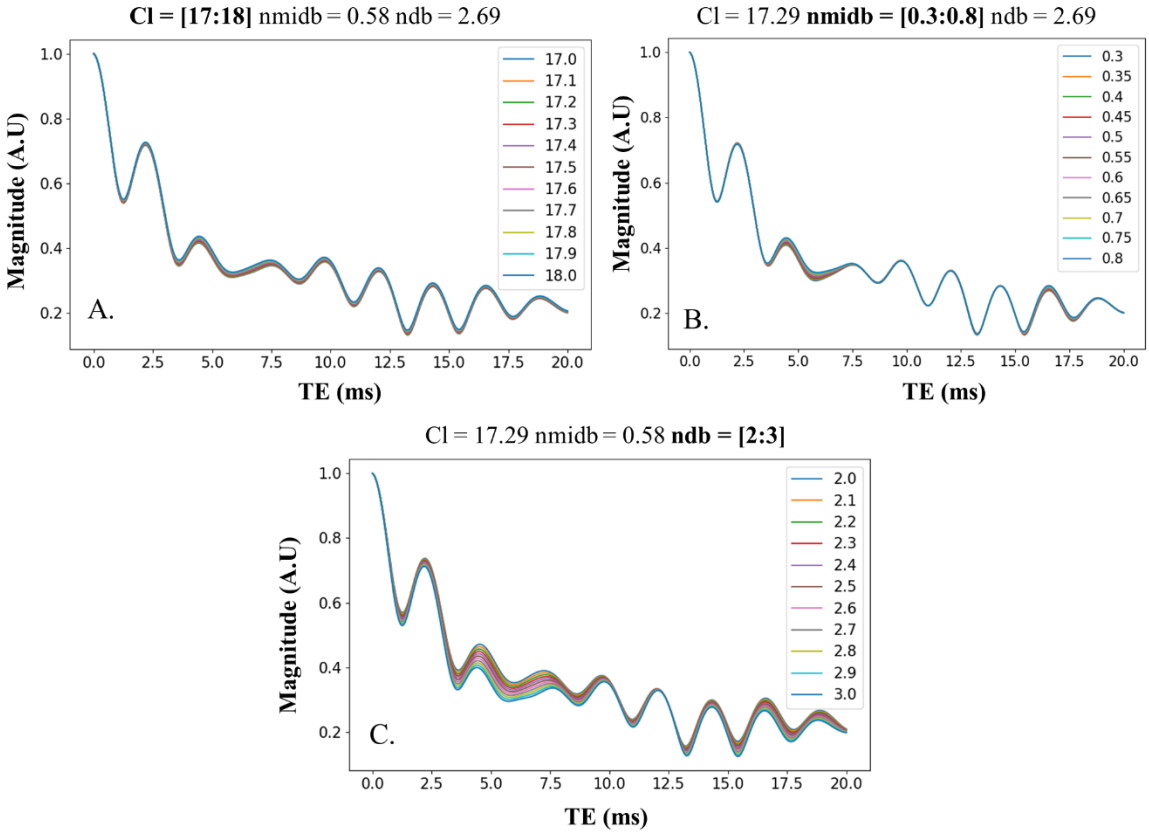

Figure 3-1 : Influence of triglyceride parameters (Cl, ndb, nmidb) on synthetic magnitude CSE-MRI signal at PDFF 90% and T_2^*=20 ms at 3T. Synthetic magnitude CSE-MRI were synthesized based on SAT fat spectrum (Cl=17.29, nmidb=0.58, ndb=2.69) with realistic variation of one parameter (A. Cl, B. nmidb, C. ndb) while the others are fixed.

Personal contributions

Starting from the water-fat algorithms benchmarking organized at the 2012 ISMRM Fat-Water MRI Workshop, I conducted a thorough review of fat-water signal separation algorithms in the literature (**Table 1-5**). In parallel, I followed a MOOC on Reproducible Research that sensitized my perspective to the benefits of reproducible research (validation process, comparison metrics, code availability) in our quest to utilize the 'optimal' algorithm. The diversity of validation process and metrics of grading the methods' performances encouraged me to re-think, and develop, a framework for a standardized comparison between these algorithms, both past and recent. Inspired by the 2012 ISMRM MATLAB format and toolbox used for the challenge, I implemented an open-

source bi-language (Python and MATLAB) toolbox. Accounting for the variety of applications of fat-water imaging, and considering my own needs for epicardial fat MRI, I included an exhaustive fat spectrum library to facilitate the fat spectrum model calibration. For a reliable and complete assessment of algorithms, I conducted the numerical simulations, participated at the elaboration of in-vitro samples (two batches, the 1st one was not satisfying), acquired imaging and spectroscopy data from these samples, along with in-vivo data. Finally, I performed the statistical analysis, prepared all the figures, and drafted the paper.

Submission status

The following chapter has been submitted as a full paper entitled Comparative Review of Algorithms and Methods for proton-density fat fraction (PDFF) quantification to Magnetic Resonance in Medicine. It was rejected, but with encouraging comments to revise the structure of the study, include a comparison with more algorithms: commercial algorithms or magnitude-based algorithms. We planned to improve this work on the following aspects:

- Modifying the introduction to link and distinguish better this work from the ISMRM Challenge 2012 toolbox
- Describing in greater details how the toolbox is structured
- Extending the comparison to open-source based magnitude algorithms
- Separating the analysis of fat-water swaps from the considerations of PDFF bias

3.2 Introduction

Chemical shift encoded MRI (CSE-MRI) techniques have become the reference for quantitative in vivo evaluation of fatty depots. Chemical shift between fat and water signals allows fat accumulation quantification and characterization. The original CSE-MRI, often referred to as Dixon techniques(55), acquire images at multiple echo times when fat/water signals are alternatively in-phase and in opposition of phase. The estimated proton-density fat fraction (PDFF), which is the ratio between fat protons over water and fat protons, derives from these images.

Mapping the PDFF has been established as refined non-invasive biomarker(141) to assess tissue adiposity in the liver(142), bone marrow(143) and other organs(144). Each application holds a specific range of PDFF but also a different type of fat composition. Complementary to PDFF and using the same multi-echo acquisition, the quantification of R_2^* decay is another biomarker of interest to further probe iron overload(145) and hemorrhage(146). The accuracy and precision of PDFF and R_2^* evaluation can be demanding, whereas the versatility of the methods remains fundamental to probe organs of varied sizes, positions and even under motion.

Nowadays, to obtain these quantitative biomarkers, advanced methods of fat-water signal separation have been developed. This abundance of methods raises the question of scientific standards for grading the methods' performances in the context of reproducible research(147).

Relevantly, over the past decade, multiple initiatives have been proposed to standardize PDFF as a quantitative imaging biomarker, starting with the 2012 ISMRM fat-water MRI Workshop. Gathered algorithms were benchmarked on a multitude of in-vivo datasets(86) and a MATLAB algorithm toolbox was developed and disseminated. It provided standardization for the input/output formats of algorithms and facilitated their comparison. More recently, groups of experts such as the PDFF Quantitative Imaging Biomarkers Assessment (QIBA) group and the ISMRM Quantitative MR Study group provided consensus guidelines to assess the development and validation of new quantitative MR methods(148,149). In the QIBA multi-site study(150), a fat/water phantom traveled to assess the precision of PDFF measurements across various MRI vendors' solutions. PDFF was demonstrated to be reproducible across sites and acquisition schemes using the same fat-water separation algorithm. However,

complementary to in-vitro validation which offers a limited evaluation, numerical simulations enable to extensively explore, validate, and compare methods in many more scenarios. For instance, a python open-source framework(151) was developed to explore optimal acquisition parameters according to the number of peaks resolved in water-fat signal model. However, this framework considered only a single algorithm, and focused only on acquisition parameters.

To use PDFF as a quantitative imaging biomarker, algorithms that calculate the quantitative maps have to be precise, reliable and comparable with others from the literature. However, numerous algorithms have emerged with a diversity of methods to solve fat-water signal separation. Whether utilizing magnitude or complex data fitting, algorithms can be based on graph-cut(72,73,75,78,79,152), region growing(66,69,71) and, more recently, deep learning(80,81,83,84) approaches. To elect optimal CSE-MRI algorithms, a numerical toolbox that fairly compares them in an extensive acquisition parameter set is needed. Indeed, renewed comparison of these algorithms has not been undertaken since a decade. Moreover, this framework should remain open source for facilitating comparison with new methods and its evolution to new challenges. Therefore, the purpose of this work was to develop a multilanguage numerical toolbox and address the performances of open-source state-of-the-art fat-water reconstruction methods for PDFF and R_2^* quantification.

3.1 Materials and Methods

3.1.1 Open-source algorithms

An open-source toolbox available both in Python and MATLAB (https://github.com/pdaude/CREAM_PDFF) was implemented to assess and numerically compare the performances of recent and novel open-source fat-water separation algorithms (**Table 3-1**). The already available algorithms include: Hernando et al(152)'s original graph-cut method (Hernando-GC), the ISMRM challenge winner leveraging quadratic pseudo-Boolean optimization graph-cut (Fatty-Riot-GC(72)), the multi-scale approach graph-cut (MSGCA-B(75)), enhanced later with spatial smoothing (MSGCA-A(78)), the globally optimal surface estimation (GOOSE(73)), the Variable Layer graph-cut (VLGCA(79)), a region-based approach (B0-NICE(66)) and an IDEAL constrained estimation (IDEAL-CE(70)).

3.1.2 Algorithm standardization

Algorithms were standardized, building upon ISMRM fat-water toolbox input structure, with the addition of the voxel dimension. Towards generalization of applications, all algorithms were adapted to accommodate an input fat spectrum in their models. Output structure from algorithms comprised of algorithms' parameters, employed model fat spectrum, and maps of Fat, Water, R_2^*, B_0, PDFF and the voxel-wise sum of square error. For all graph-cut algorithms, the discretization of B_0 fields was set at 2Hz-steps.

Table 3-1 : Summary of evaluated state-of-the-art open-source Fat-Water reconstruction algorithms with specific features, corresponding references and code repository links.

Reference	Referred as	Method	Code	2D/ 3D	Spectrum choice	Echo spacing	Code acceleration	Year	**Code repository** (If not specified,it is on github.com)
Boehm et al. (79)	VLGCA	Graph-cut	MATLAB	2D	Free	Uniform	Parallel computing	2021	gitlab.com/christofboehm/fieldmap-graph-cut
Bydder *et al.* (70)	IDEAL-CE	IDEAL	MATLAB	3D	Model Constrained	Free	GPU computing	2020	marcsous/pdff
Andersson et al. (78)	MSGCA-A	Graph-cut	MATLAB	3D	Free	Uniform	No	2018	Snubben-B/FW-Recon-Spatial-Smoothing
Cui et al.(73)	GOOSE	Graph-cut	MATLAB	2D	Fixed[a]	Uniform / Free	No	2015	https://research.engineering.uiowa.edu/cbig/content/goose
Berglund et al.(75)	MSGCA-B	Graph-cut	Python	3D	Free	Uniform	No	2017	bretglun/fwqpbo
Liu et al. (66)	B0-NICE	Region-based	MATLAB	3D	Fixed[b]	Uniform	No	2015	https://www.mathworks.com/MATLABcentral/fileexchange/48313-b0-mapping-b0-nice
Berglund et al.(72)	Fatty-Riot-GC	Graph-cut	MATLAB	3D	Free	Uniform	No	2012	**welcheb/fw_i3cm1i_3pluspoint_berglund_QPBO** **welcheb/FattyRiot**
Hernando et al. (152)	Hernando-GC	Graph-cut	MATLAB	2D	Free	Uniform / Free	No	2012	ISMRM Workshop on Fat-Water Separation: Insights, Applications & Progress in MRI

a. ISMRM challenge spectrum

b. own spectrum

3.1.3 Monte Carlo simulation

To numerically evaluate the algorithms' performances, synthetic CSE-MRI volumes were modeled as :

$$y = \left(W + F \sum_{m=1}^{m} \alpha_m e^{i\omega_m t} \right) e^{(i(\omega_0+\varphi_0)-R_2^*)t} + N(t)$$

Eq 3-1

with W=(1-PDFF) and F=PDFF corresponding to normalized water and fat absolute signal, ω_0 the off-resonance, $\varphi_0 = 30°$ the initial phase, R_2^*=50 s^{-1} the transversal decay, N(t) the complex gaussian noise and α_m, $e^{i\omega_m}$ the relative amplitude and frequency offset of a subcutaneous fat spectrum respectively. Considering a 3T scanner field strength, virtual CSE-MRI volumes were synthesized as follows: along the x-axis, PDFF varied from 0 to 100% with 1% step, along the y-axis, B_0 was uniformly distributed from -300Hz to 300Hz(153) with 6Hz step, in z-axis consist in 100 repetitions. Gaussian noise N(t) was added to obtain SNR=10, 50, 100. Synthetic volumes were normalized based on 99% of the maximum of the first echo. To avoid border effects due to spatial regularization, a five pixels padding was added for each CSE-MRI volume. Different numbers of echo times (NTE=3, 5, 7, 9) and echo spacing schemes were considered.

3.1.4 Acquisition parameter: echo spacing

Multiple echo time sampling schemes were explored through numerical evaluations of the algorithms' sensitivity, with the aim to optimize the precision of targeted parameter, such as PDFF or R_2^*. Acquisition constraints (minimum TE and echo-spacing due to field strength and acquisition parameters, including dwell time and resolution) also influence echo-times sampling. Finally, most of the compared algorithms were constrained by uniform echo spacing CSE MRI. Thus, in this toolbox a function was developed to automatically calculate echo time schemes based on acquisition constraints for any number of echoes. The uniform IDEAL echo-shift formulated by Pineda(154) was generalized to offer realistic IDEAL echo spacing, abiding to both acquisition constraints and the following criteria:

$$\Delta\theta_{k,j} = \frac{2\mathrm{k}}{\mathrm{N}}\pi + 2j\pi \; with \; k \in [\,1, N[\; and \; \gcd(k, N) = 1, j \in \mathbb{N}.$$

Eq 3-2

Demonstration of this functionality is detailed in **Supportive Information S 3-1**.

In this context, considering the minimum echo spacing constraint, prime or odd number of echoes offered more solutions in Eq 2 and were then, more permissive to obtain realistic IDEAL TE (3, 5, 7, 9) for the Monte-Carlo simulation. The chosen echo spacing schemes were realistic minimal IDEAL and in-/out of phase with echo times calculated when considering hardware constraints at 3T (TE_{min}=0.98ms and ΔTE_{min}=1.68ms).

3.1.5 Fat spectrum library

The CSE-MRI signal model (Eq 3-1) relies on a multi peak fat spectrum model with established relative amplitudes and chemical shifts corresponding to triglycerides(155,156). The choice of fat spectrum has been shown to reduce PDFF bias estimation compared to single fat peak spectrum model(157) but remains highly variable in the implementations. Contrary to the ISMRM challenge which benchmarked algorithms with a single human fat spectrum, the algorithms' sensitivity to the diversity of human fat NMR spectra(158) was explored in this study. Moreover, using a generic triglyceride model(28), fat NMR spectra could be described with only three parameters: number of double bonds (ndb), number of interrupted methylene double bonds (nmidb) and chain length (CL). Thus, an extensible human fat spectrum(28,38,59) library was implemented in the toolbox. Additionally, this simplified model enables us to translate gas-chromatography measurements of fatty acids composition to NMR spectrum signal. Thus, any spectrum could easily be integrated within each algorithm. Synthetic CSE volume was modeled with the subcutaneous fat spectrum (CL=17.29, ndb=2.69, nmidb=0.58). To probe spectra influence, synthetic signals (NTE=9) were simulated with a peanut oil spectrum and processed with either the same calibrated peanut oil spectrum or with the ISMRM challenge spectrum.

3.1.6 In vitro: fat-water phantom

Eight fat-water phantoms of 50mL were prepared with different fat fraction of peanut oil. Recipes and protocols from Hines et al(159) and Bush et al(160) were followed scrupulously to obtain stable and homogeneous samples. A water solution was prepared

containing deionized water, 15 mM sodium dodecyl sulfate (Sigma Aldrich, St Louis, MO), 3.75 mM of sodium azide (Sigma Aldrich, St Louis, MO), 0.185mM of $MgCl_2$ (Sigma Aldrich, St Louis, MO) to shorten $T_1^{H_2O}$ and 1.0% w/v agarose (Sigma Aldrich, St Louis, MO). The volume percentages of oil in the phantoms were targeted at 0, 10, 20, 40, 60, 80, 90 and 100% and were calculated with MRS reference at 0, 8.50, 20.01, 37.03, 63.19, 85.40, 92.14, 100% (**Supportive Information Figure S 3-1**).

Imaging and spectroscopy data were acquired in a 3T MRI system (Magnetom Vida, Siemens Healthcare, Erlangen Germany) using a 20-channel head coil. Phantoms vials were aligned along the static magnetic field direction, and iterative shimming was performed prior to the acquisitions. Using a monopolar 3D spoiled gradient echo sequence, 1.8x1.8x2.5 mm, FOV=172x288x140mm, FA=6°, BW=1563 Hz/px and echo times similar to the Monte Carlo simulation (realistic minimal: TE1/ΔTE=0.98/1.68 ms, in-out-of-phase: TE1/ΔTE=1.19/3.58 ms, IDEAL: TE1=0.98 ms, ΔTE=3.18, 1.91, 1.70, 1.86 ms for 3, 5, 7 and 9 echoes respectively) with a maximum scan time of 2 min. Spectroscopy data were acquired using a non-localized FID with TR=8000ms for each phantoms vials.

Fitting of spectroscopy data was performed using a Linear Combination model implemented in FSL-MRS(161) version 1.1.10, part of FSL (FMRIB's Software Library, www.fmrib.ox.ac.uk/fsl). Briefly, basis spectra were fitted to the complex valued spectrum in frequency domain. The basis spectra were shifted and broadened with parameters fitted to the data grouped in 2 metabolites groups (water and lipids). A complex polynomial baseline was also concurrently fitted (order=3). Model fitting was performed using the Metropolis Hasting algorithm.

3.1.7 In vivo imaging

For practical demonstration purposes, leading algorithms' discrepancies were evaluated on challenging in vivo datasets. Three healthy volunteers were recruited after informed consent. MR images were acquired with the same MR system using a dedicated cardiac 18-channel coil array and the spine coil. Supraclavicular body fat, that contains brown fat, bone marrow fat in the sacrum region and liver were considered challenging applications due to a large range of B_0 inhomogeneity, low SNR and subtly varying fat content.

Two supraclavicular CSE-MRI data sets were acquired using a coronal 3D spoiled gradient echo sequence, with 1. a spatial resolution of 1.88x1.88x3 mm^3, 9 echoes (TE1/ΔTE=0.73/1.44 ms), FOV=360x247x192mm^3, FA=6°, BW=1532 Hz/px for all echoes and 2. a spatial resolution of 1.67x1.67x3 mm^3 6 echoes (TE1/ΔTE=1.23/1.23 ms), FOV=319x319x192 mm^3, FA=6°, BW=1240 Hz/px for all echoes. Sacrum CSE-MRI was also acquired using 2D spoiled gradient echo sequence with in-plane resolution of 1.8x1.8 mm^2, 7 echoes (TE1/ΔTE=1.2/1.54 ms), FOV=287x287 mm^2, slice thickness 6mm, FA=8°, BW=744 Hz/px for all echoes. Finally, liver CSE-MRI was acquired using a transversal 3D spoiled gradient echo sequence with a spatial resolution of 2.25x2.25x2.3 mm^3 7 echoes (TE1/ΔTE=0.93/1.53 ms), FOV=360x288x147mm^3, FA=5°, BW=1563 Hz/px for all echoes, CAIPIRINHA(162) 4 (2x2).

3.1.8 Evaluation metrics and statistical analysis

The comparison followed the guidelines provided by the Quantitative Imaging Biomarkers Assessment(148). From Monte-Carlo simulation, algorithms results were evaluated based on their bias, precision, and limits of agreement (LOA) for each model parameters (PDFF, B_0, R_2^*). As an indication, the computational times of the algorithms were recorded and reported as seconds per slice. Computations were performed in MATLAB R2019b and Python v3.7.5 with a computer equipped with a GPU (Nvidia Quadro P5000, 16Gb) and 40 CPUs (Intel Xeon e5-2630 v4, 2.20Ghz,). Statistical analysis was conducted using R (version 3.6.3) (134).

3.2 Results

3.2.1 Numerical simulations

Expectedly, the echo number and spacing schemes affected the performance of the algorithms (**Figure 3-2**). Several pitfalls were noticeable for NTE=3: fat/water swaps were present when processing with Fatty-Riot-GC and B0-NICE. PDFF measured with Hernando-GC was influenced by B_0 inhomogeneity (NTE=3 IN/OPP & IDEAL). GOOSE led to a significant global bias (>15%). Thus, with only 3 echo times, only MSGCA-A/B, IDEAL-CE and VLGCA gave more robust results compared to the other algorithms.

For NTE ≥ 5, B0-NICE and GOOSE proved to be still highly biased and were not further compared, whereas the other algorithms demonstrated robustness to B_0 and fat/water swaps. In addition to B0-NICE and GOOSE, VLGCA and Hernando-GC, were still influenced by echo spacing for PDFF quantification (VLGCA: P <0.0001, Hernando-GC (P <0.05).

Increasing the number of TE (NTE=7 and 9) improved PDFF precision, absolute bias decreased significantly (P <0.0001) for all algorithms (**Supportive Information Figure S 3-2**). Individually considering the best echo spacing for PDFF measurement at SNR 50, algorithms provided similar PDFF bias (bias<0.15 LOA<2.6 %) (**Figure 3-3**). However, extrema PDFF (<10% or >90%) remained challenging for most algorithms and differentiated their performances: for NTE=7, LOA in extrema PDFF were 0.3% for IDEAL-CE and were greater than 1.1% for the other algorithms.

As shown in **Figure 3-3**, algorithms provided a low R_2^* mean bias (<0.15 s^{-1}) but with large LOA depending on echo times ($LOA_{IN/OUT\text{-}OF\text{-}PHASE}$=5.8 s^{-1}, LOA_{IDEAL}=9.3 s^{-1}, $LOA_{MINIMAL}$=9.6 s^{-1}). Increasing the number of TE decreased significantly (P <0.0001) the LOA for all algorithms.

Computation times for processing one slice with NTE=7 ranged from $T_{B0\text{-}NICE}$=1.81±0.24s, $T_{IDEAL\text{-}CE}$=1.95±0.02s, to $T_{Fatty\text{-}Riot\text{-}GC}$=51.34±18.04s and T_{GOOSE}=5455.18±7122.50s.

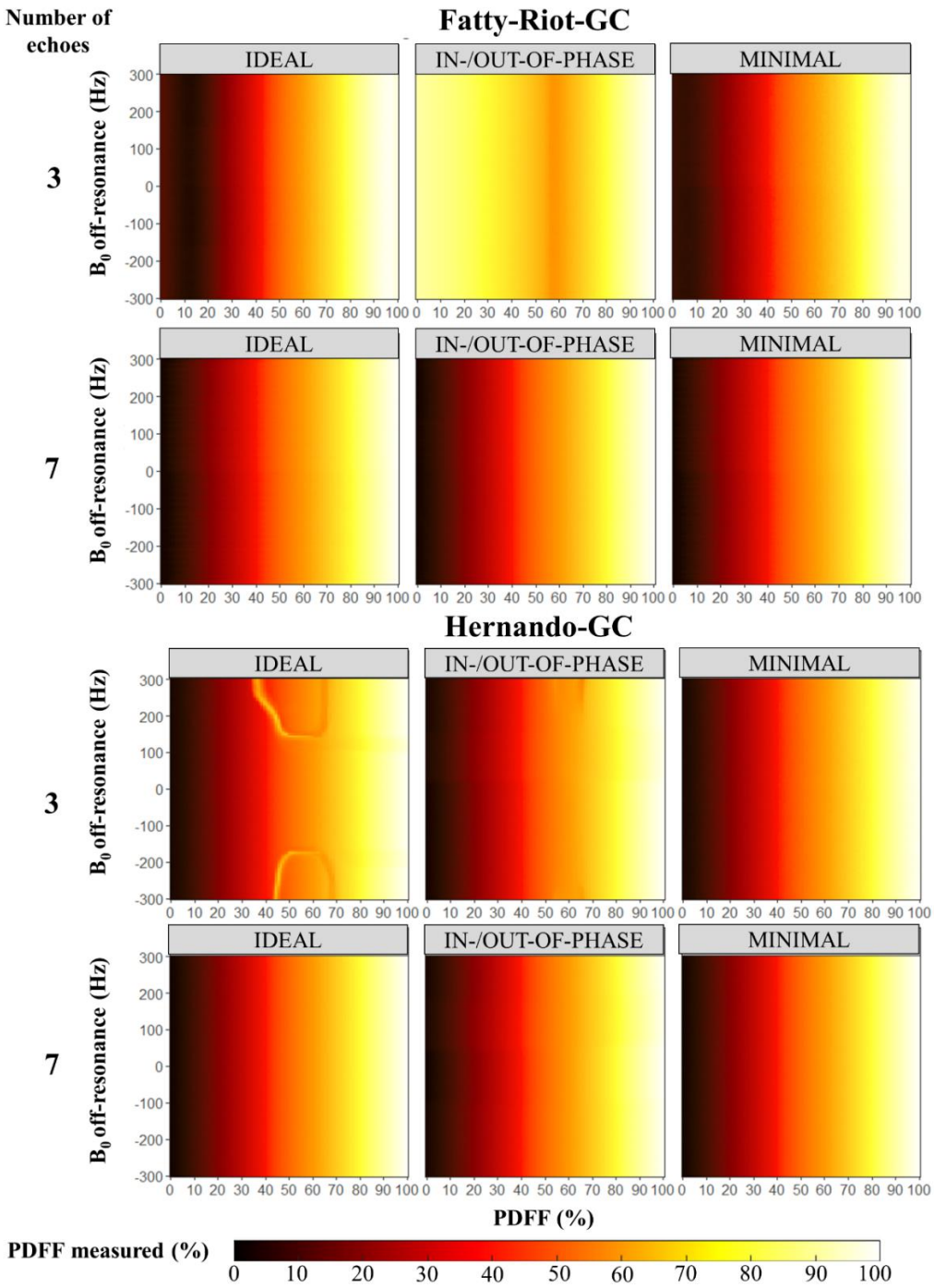

Figure 3-2 : PDFF was measured by Fatty-Riot-GC and Hernando-GC over synthetic CSE-MRI volumes with SNR=50 at 3 and 7 echoes. PDFF maps were averaged along repetition axis and separated according to the echo spacing scheme (IDEAL, IN-/OUT-OF-PHASE, MINIMAL). Fat-water swaps were visible at 3T with Fatty-Riot-GC while bias appeared on the PDFF map processed by Hernando-GC due to B_0 inhomogeneities. With 7 echoes, both algorithms provided more reliable quantitative maps.

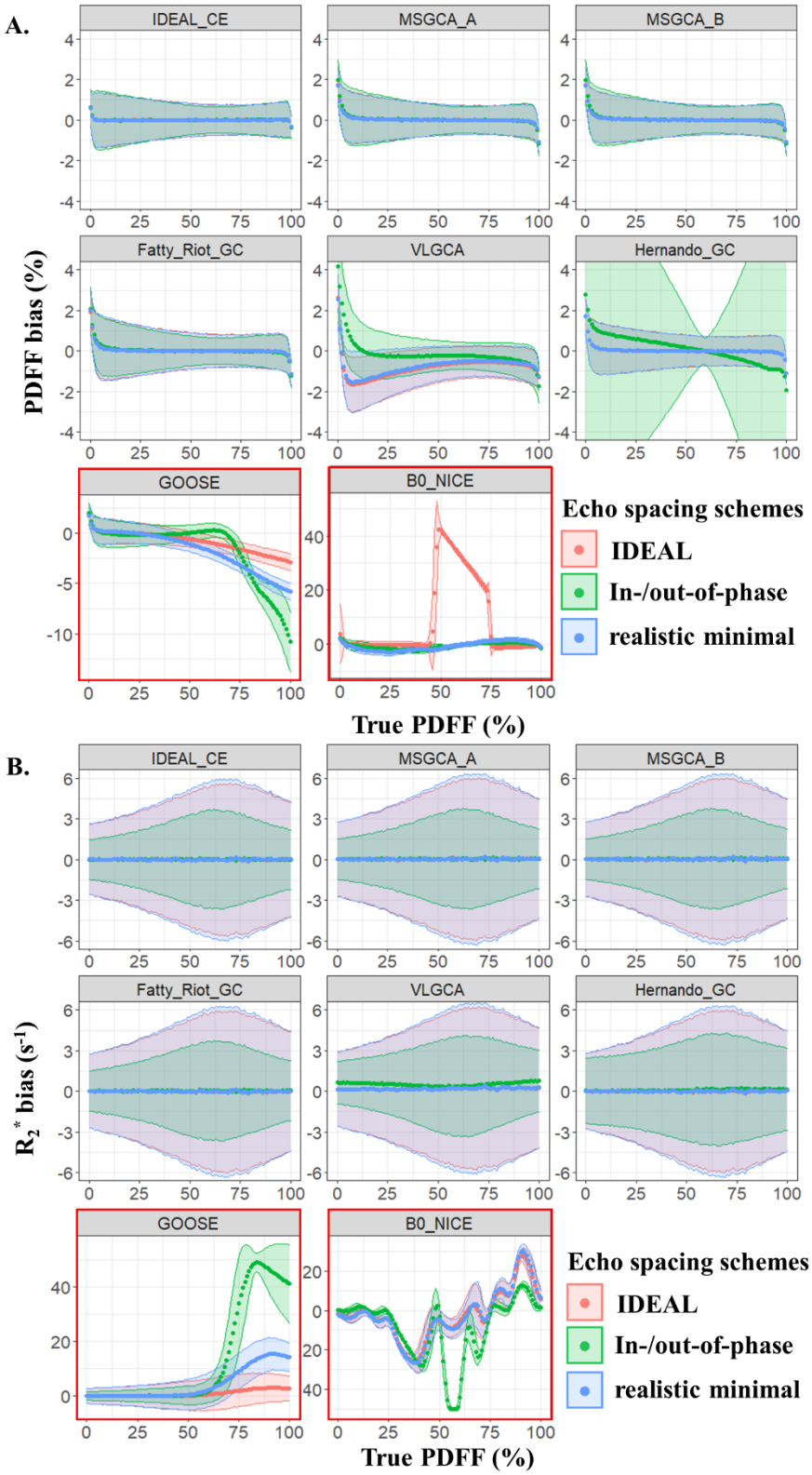

Figure 3-3 : Comparison of PDFF (A) and R_2^* (B) bias of each algorithm over synthetic CSE-MRI volumes with NTE=7 and SNR=100. Mean and standard deviation PDFF and R_2^* bias were averaged along the B_0 off-resonance and repetition axes and

separated (in color) according to the echo spacing schemes. GOOSE and B0-NICE (in red square) where not further investigated due to highly bias results.

3.2.2 In vitro experiments

Experimental SNR varied across vials with a minimum of 50 and a maximum of 190. Confirming simulation results, the algorithms proved robust to fat/water swaps and B_0 offset with NTE ≥ 5. Indeed, at 3T, with NTE=3, Fatty-Riot-GC was influenced by B_0 inhomogeneity which varied from −220 Hz to 150 Hz through the phantom volume whereas MSGCA-B produced a fat-water swaps in the 60% oil vial (**Figure 3-4**). For PDFF quantification, GOOSE, VLGCA, Fatty-Riot-GC and MSGCA-A were significantly influenced ($p < 0.05$) by echo spacing with NTE=7. Indeed, the mean variation of bias between realistic minimal and IDEAL echo spacing scheme was of 0.1% for VLGCA, Fatty-Riot-GC and MSGCA-A and 1.2% for GOOSE respectively. The mean variation of bias between IN/OPP and IDEAL echo spacing scheme was of 1.5% for VLGCA and 1.9% for GOOSE. Using NTE=7, apart from GOOSE and B0-Nice, all algorithms provided mean PDFF absolute bias below 3%.

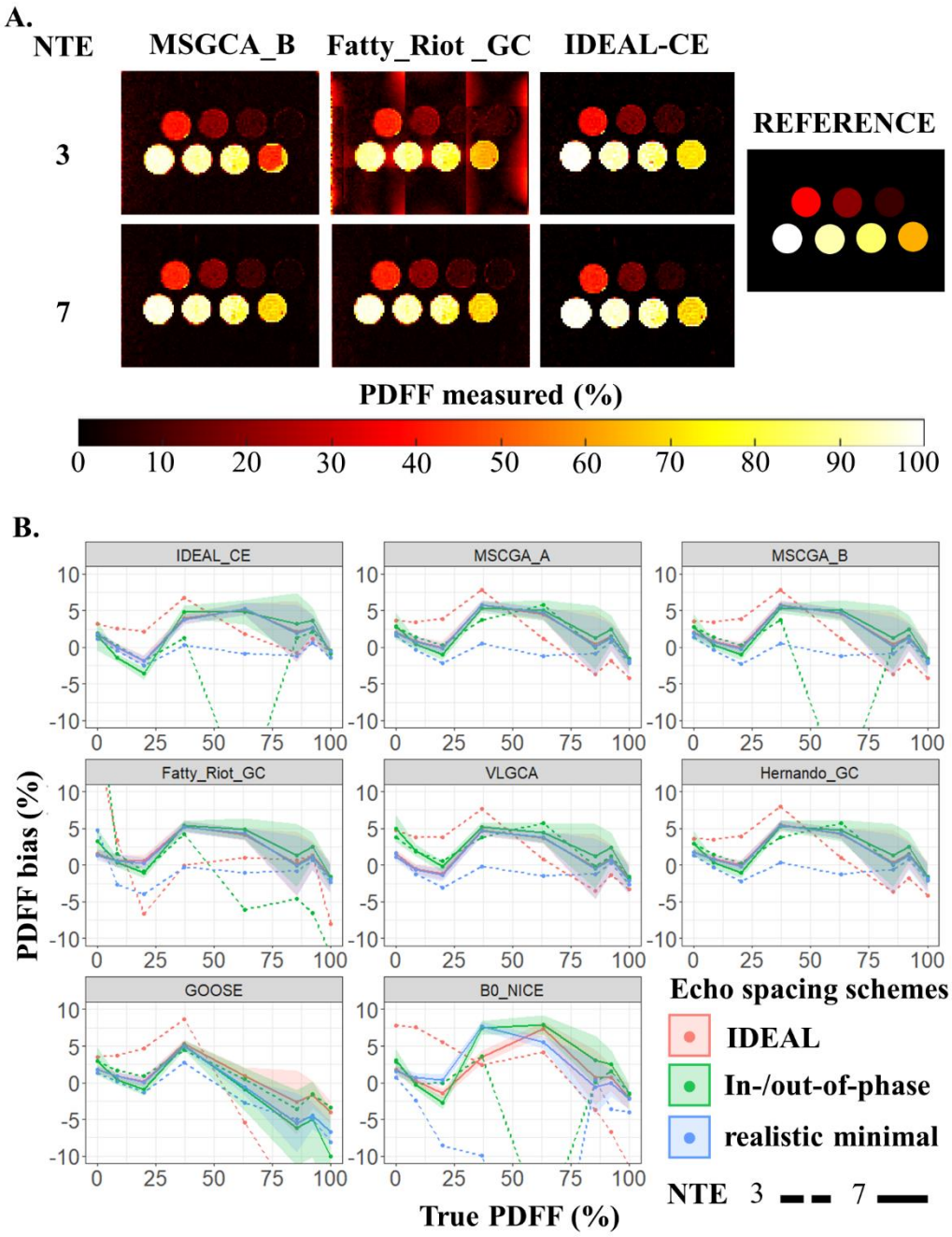

Figure 3-4 : A. PDFF measurement from in-vitro experiments using MSGCA-A, Fatty-Riot-GC and IDEAL-CE with NTE=3 and NTE=7 and in-/out-of-phase echo spacing. B. Comparison of PDFF bias of each algorithm in phantoms. Mean and standard deviation PDFF bias were averaged along the B_0 off-resonance and repetition axes and separated according to the echo spacing schemes (in colour) and echo number (in line style). For clarity, only standard deviation of PDFF bias for NTE=7 have been plotted.

3.2.3 In vivo experiments

The in vivo experiments were challenging due to large B_0 inhomogeneity variations measured by frequency offset up to Δ_{B0}=500 Hz and 350 Hz for supraclavicular and sacrum regions respectively. As shown in **Figure 3-5**, algorithms that were comparable in silico (IDEAL-CE, MSGCA-A and Fatty-Riot-GC) demonstrated significant PDFF discrepancies in vivo: graph-cuts algorithms were misled by the strong B_0 gradient and resulted, as initially observed in **Figure 3-2**, to fat-water swaps or B_0-dependent PDFF values. Eventually, these algorithms overestimated fat content in tissues with negligible expected adiposity (in the bladder: $PDFF_{IDEAL\text{-}CE}$=0.45% ± 0.81, $PDFF_{MSGCA\text{-}A}$=18.24±10.20, $PDFF_{Fatty\text{-}Riot\text{-}GC}$=90.87±2.68%). However, for liver CSE-MRI challenging due to low SNR=14, the three algorithms provided similar performance with a standard deviation in the liver ($SD_{IDEAL\text{-}CE}$=2.45% / 10.26 s^{-1}, $SD_{MSGCA\text{-}A}$=2.46% / 10.25 s^{-1}, $SD_{Fatty\text{-}Riot\text{-}GC}$=2.35% / 10.25 s^{-1}) for PDFF and R_2^* respectively, confirming equivalent, and very acceptable, noise propagation in these algorithms.

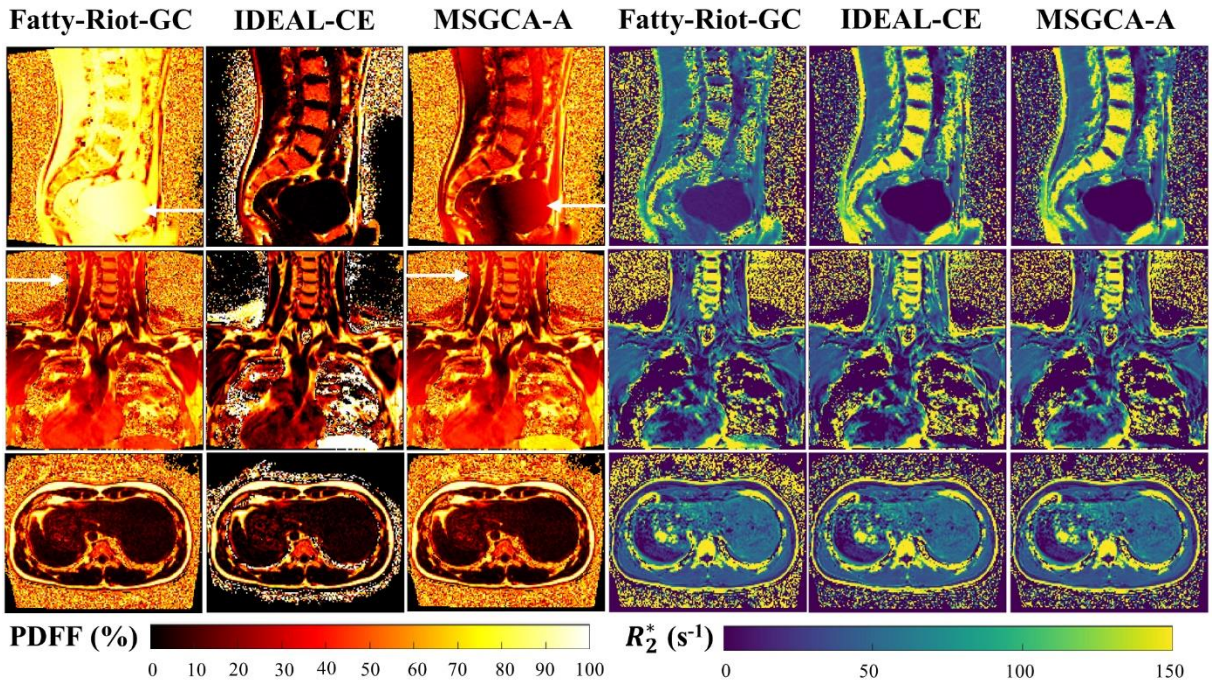

Figure 3-5 : PDFF and R_2^* quantification of Fatty-Riot-GC,IDEAL-CE and MSGCA-A over challenging in-vivo datasets at 3T. PDFF overestimation was observed using MSGCA-A and Fatty-Riot-GC as shown by white arrows where fat is not expected inside the bladder or the neck.

3.2.4 Influence of the spectrum model

As shown in **Figure 3-6-A**, the synthetic magnitude CSE signal decay depends on the fat spectrum model chosen. Processing data with a different spectrum (ISMRM challenge) than the one employed for simulation (peanut oil) revealed a significant bias in PDFF quantification (P <0.0001) and R_2^* (P <0.0001) with a maximum bias of 2.35% and 20.66 s^{-1}, respectively, at NTE=9 and SNR=100 (**Figure 3-6-B**). In vitro (**Figure 3-6-C**) and in vivo (**Figure 3-6-D**) experiments revealed similar values with mean PDFF and R_2^* differences of 1.22% and 12.22 s^{-1} respectively in supra-clavicular adipose tissue.

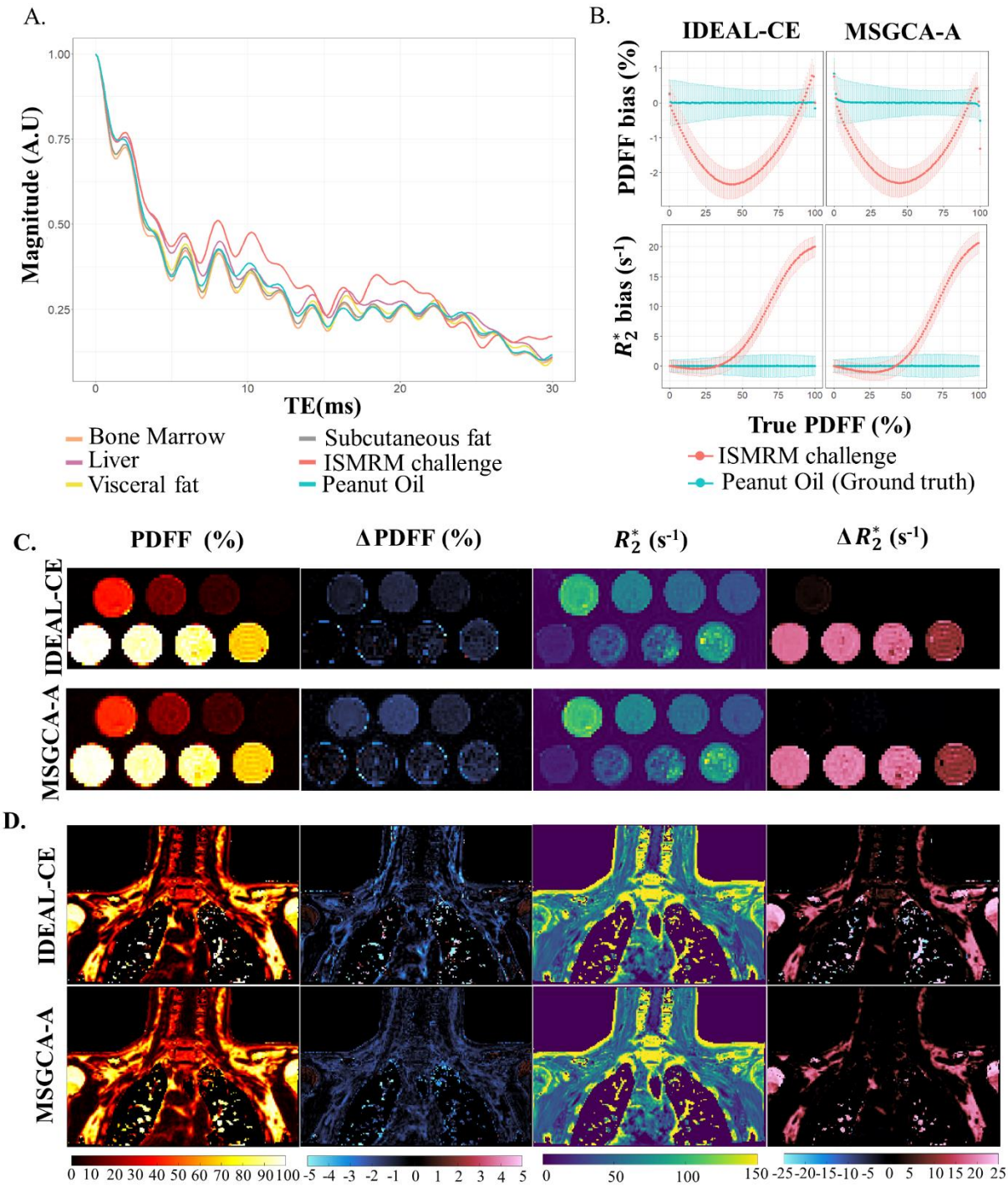

Figure 3-6 : Influence of fat spectrum models on PDFF and R_2^* quantification with IDEAL-CE, MSGCA-A : A. Synthetic magnitude CSE-MRI signal at PDFF 100% and T_2^*=20 ms with different spectrum depicted in the literature or acquired for this study.B. PDFF and R_2^* bias when synthetic CSE-volume are processed with either the same spectrum (peanut oil) or with the ISMRM challenge one at 3T with 9 echoes and realistic minimal echo-spacing. PDFF, R_2^* measurement when in vitro

experiment (.C) or in in vivo (.D) were processed with peanut oil spectrum at 3T with 9 echoes with a minimal echo spacing scheme and the difference ΔPDFF, ΔR_2^* resulted when those data were processed with the ISMRM challenge spectrum.

3.3 Discussion

In keeping with standardization of MRI body fat quantification, an open-source toolbox was implemented to evaluate fat-water separation algorithms, offering the possibility to better appreciate the precision and accuracy of recently proposed algorithms. This benchmarking also allows the optimization of acquisition parameters (echo number and spacing) to obtain more accurate quantitative maps.

3.3.1 Open-source framework and reproducibility research

The proposed toolbox was developed in both Python and MATLAB programming languages to facilitate benchmarking of fat-water separation algorithms. It can be considered as an extension of the ISMRM fat-water toolbox that currently allows to compare MATLAB algorithms only. Another addition is the capability to operate with an exhaustive fat spectrum library. This framework was made open-source (https://github.com/pdaude/CREAM_PDFF) to ease comparison with new methods.

3.3.2 Numerical simulations

Provided with synthesized data using only 3 echoes, most algorithms suffered from fat-water swaps or bias due to B_0 inhomogeneities (**Figure 3-2**) while 5 or 7 echoes provided a significant improvement in reliability and precision in PDFF measurement. Even when using 5 echoes, the precision of PDFF for VLGCA, Hernando-GC, B0-NICE and GOOSE was still greatly dependent on the echo spacing. In contrast, MSGCA-A, MSGCA-B, IDEAL-CE, Fatty-Riot-GC proved robust to echo-spacing and provided similar results, all suitable for a reliable PDFF quantification (**Figure 3-3-A**).

Considering the latter algorithms, echo spacing still influenced the precision of the R_2^* quantification (**Figure 3-3-B**).With a fixed number of echo times, R_2^* precision depended on the longest echo time. Therefore, to quantify R_2^* with a given number of echoes, in-

phase/out-of-phase schemes should be preferred to IDEAL or minimal echo spacing. However, with a fixed TR, minimal echo spacing, potentially allowing fitting more echoes, should be preferred to the other echo spacing schemes for R_2^* accuracy.

In addition to help in choosing optimal set of parameters (echo scheme, number of echoes) for a specific acquisition, this toolbox also provides an estimate of precision in parameter quantification by predicting margins of error for a given SNR.

3.3.3 In vitro experiments

The in vitro experiments enabled us to validate the numerical findings. Notably, experimental results confirmed the necessity to acquire at least 5 echoes to avoid fat-water swaps and bias due to B_0 inhomogeneities with most algorithms (**Figure 3-4**). It also showed that the echo-spacing scheme can influence PDFF quantification even with 7 echoes: the mean variation of bias between IN/OPP and IDEAL was 1.5% for VLGCA and 1.9% for GOOSE. Using spectroscopy as a reference measurement, PDFF bias was higher than in the corresponding simulation for all algorithms and in particular for vials with 40% and 60% fat. This discrepancy could be due to the model assumption of a common single R_2^* value for fat and water when a dual R_2^* would have been more relevant(163). As the majority of algorithms make this assumption, separate R_2^* has not been investigated in this study, but they would be a valuable extension for double-R_2^* fat-water algorithms.

3.3.4 In vivo experiments

Challenging in vivo data surprisingly revealed disparities between numerically comparable algorithms (IDEAL-CE, MSGCA-B, Fatty-Riot). These may be due to rapid and large variations of B_0 which breaks the stringent constraint of a smooth field map assumed by these algorithms (**Figure 3-5**). However, algorithms provided similar performance and showed to be highly resilient to to challenging low SNR in-vivo data (SNR=14) with PDFF and R_2^* measurements standard deviation in liver of 2.4% and 11 s^{-1} which was verified by simulation (**Supportive Information Figure S 3-3**).

3.3.5 Influence of the spectrum model

Interestingly, processing data with a different spectrum from the simulation led to a non-negligible bias in PDFF and R_2^* (**Figure 3-6**). The in vitro and in vivo experiments confirmed this difference, as shown in **Figure 3-6.C** and **Figure 3-6.D** thus electing a relevant spectrum remains essential for characterizing fat deposits with different fatty acid composition. This consideration might be even more important in applications such as CSE-MRI of bone marrow. The sensitivity of PDFF quantification alone to multi peak fat spectrum calibration has been previously explored(157) using synthetic CSE data with low PDFF (<=40%), 6 echoes and a graph-cut algorithm. Within this range, the choice of the number of spectrum peaks was found not to significantly impact PDFF. Our results extend these findings, demonstrating that with enough echoes (NTE=9) and high SNR, there can be a small bias (<2%) for PDFF within the PDFF range of 20-80% depending on the selected fat spectra. But more importantly, the choice of spectra significantly influenced the R_2^* bias, which can alter the evaluation of iron content in organs such as liver or bone marrow.

3.3.6 Algorithms running time

Apart from GOOSE, the algorithms' running times on the system used were within seconds to minutes of processing time per slice. Considering the limited computational optimization of open-source implementations (in MATLAB or Python), the 8 remaining algorithms are all potentially suitable for a clinical routine PDFF quantification upon code optimization. We noted that algorithms developed after the 2012 ISMRM challenge (MSGCA-A/B, IDEAL-CE, B0-NICE, VLGCA) were faster than the earlier ones (Hernando-GC, Fatty-Riot-GC).

3.3.7 Choices of open-source algorithms

Some of the current state of the art open-source algorithms, were not investigated within our comparison study. Indeed, new approaches for solving the fat-water separation problem based on deep learning have emerged(82–84). However, all currently available algorithms are based on a fixed number of echoes or need a specific training strategy and network modification to be compatible with our benchmark. Moreover, all

algorithms in this study are based on the complex signal model, and it would be interesting to include those using only the magnitude signal model as they have been developed to be more robust to phase errors and avoid field map estimation. However, to our knowledge, there were no open-source algorithms of this type documented in the literature at the time of this study.

3.3.8 Possible extensions and new challenges

This open-source toolbox was designed to be evolutive to tackle new challenges, leaving room for multiple extensions that were beyond the scope of this study. First, more diversified validation data(150) with multi-site, multi-vendor, multi-field in-vivo and phantom data certainly reinforce the evaluation of Fat-Water separation methods, albeit in a less extensive and controlled set-up than in silico studies allow for. Evidently, numerical simulations are also limited, as proven by our experimental phantoms results that hinted at a bias from the single T_2^*-relaxation signal model. Nevertheless, algorithms extensions based on B_0 field map initialisation are also of interest as new methods have incorporated a priori information of the scanner magnetic field distribution(76,164). Recently, algorithms have started to include refined complex signal MR models, designed for quantitative fatty acid composition parameter mapping(36,59). A standard evaluation of such advanced algorithms performance will definitely hold interest. Finally, as it has already been done for Quantitative Susceptibility Mapping (QSM) processing pipelines with the SEPIA(165) package, a graphical user interface for this framework could also benefit from a user's perspective.

3.4 Conclusions

In accordance with standardization of MRI body fat quantification, an open-source bi-language toolbox was developed to evaluate eight state-of-the-art open-source algorithms for fat-water separation. Numerical simulations showed that bias and limits of agreement revealed disparities between algorithms depending on the number of echoes and spacing schemes, confirmed by in-vitro experiments. To obtain reliable PDFF quantification, it seems that all algorithms tested required more than 3 echoes. Among the eight algorithms, two proved to be inaccurate whereas the other provided comparable performances. Extrema PDFF remained challenging for accurate estimation, impacting

certain in-vivo applications. The choice of the fat spectrum model influenced PDFF quantification and, more severely, the R_2^* measurements. This benchmark also allows to optimize acquisition parameters (echo number and spacing) by predicting margin of errors of algorithms to obtain more accurate quantitative maps.

3.5 Supportive Information

Supportive Information S 3-1: IDEAL TE values computation for arbitrary numbers of TE

According to information theory, a parameter-specific mathematical optimization can be proposed that maximizes the corresponding Fisher matrix. Here the fat fraction precision can be optimized by choosing optimal echo times (TE). In the Dixon model, Pineda et al(154) demonstrated by minimizing the Cramer-Rao lower bound, that the optimal estimation of fat and water magnitude is obtained by distributing N echo time sampling (TE) at regular intervals referred commonly as IDEAL TE:

$$TE(k) = \frac{\frac{\pi}{2} + \frac{2\mathrm{k}}{\mathrm{N}}\pi}{\gamma B_0 CS_{FW}} + 2j\pi$$

$with\ k \in [\,1, N[\,, j \in \mathbb{N}, B_0$ the static magnetic field and CS_{FW} the fat-water chemical shift, N the number of echoes.

Those intervals $\Delta\theta$ assured that the echo times are equally spaced over the unit circle as

$\Delta\theta_{\mathrm{j}} = \frac{2}{\mathrm{N}}\pi + 2\mathrm{j}\pi$ with $\mathrm{j} \in \mathbb{N}$, N the number of echoes Eq. S3

Due to hardware constraints, the smallest ΔTE, referred as $\Delta TE_{min} = \frac{\Delta\theta_0}{\gamma B_0 CS_{FW}}$ is often impossible to be reached. $\Delta\theta_1$ imposed an additional 2π interval which could be deleterious in organs for which there is rapid signal decay due to susceptibility. Thus, we studied if it was possible to define other echo times spacing $\frac{2\mathrm{k}}{\mathrm{N}}\pi$, given N the number of echo times, which respect equally distributed echo-times over the unit cercle. As a prerequisite, each $\frac{2\mathrm{k}}{\mathrm{N}}\pi$ step has to satisfy that one of its multiples is equal to $\frac{2\pi}{N}$, modulo 2π. As such, k verifies:

Let $\mathrm{N} \in \mathbb{N}^*$, $k \in [\,1\,, N[\,, j \in \mathbb{N}$ and $\alpha \in [\,1\,, N[\,,$ $thus\ the\ set\ of\ k\ which\ satisfied$ $\alpha * \frac{2\mathrm{k}}{\mathrm{N}}\pi = \frac{2\pi}{N} + j * 2\pi \iff \alpha * \mathrm{k} = 1 + j * N$ are $\gcd(k, N) = 1$

The latest equation is demonstrated thanks to Bachet Bezout theorem. Thus, we extended Pineda equation (Eq. S1) with

$\Delta\theta_{k,j} = \frac{2\mathrm{k}}{\mathrm{N}}\pi + 2j\pi$ $with$ $k \in [\,1\,, N[$ and $\gcd(k, N) = 1$, $j \in \mathbb{N}$.

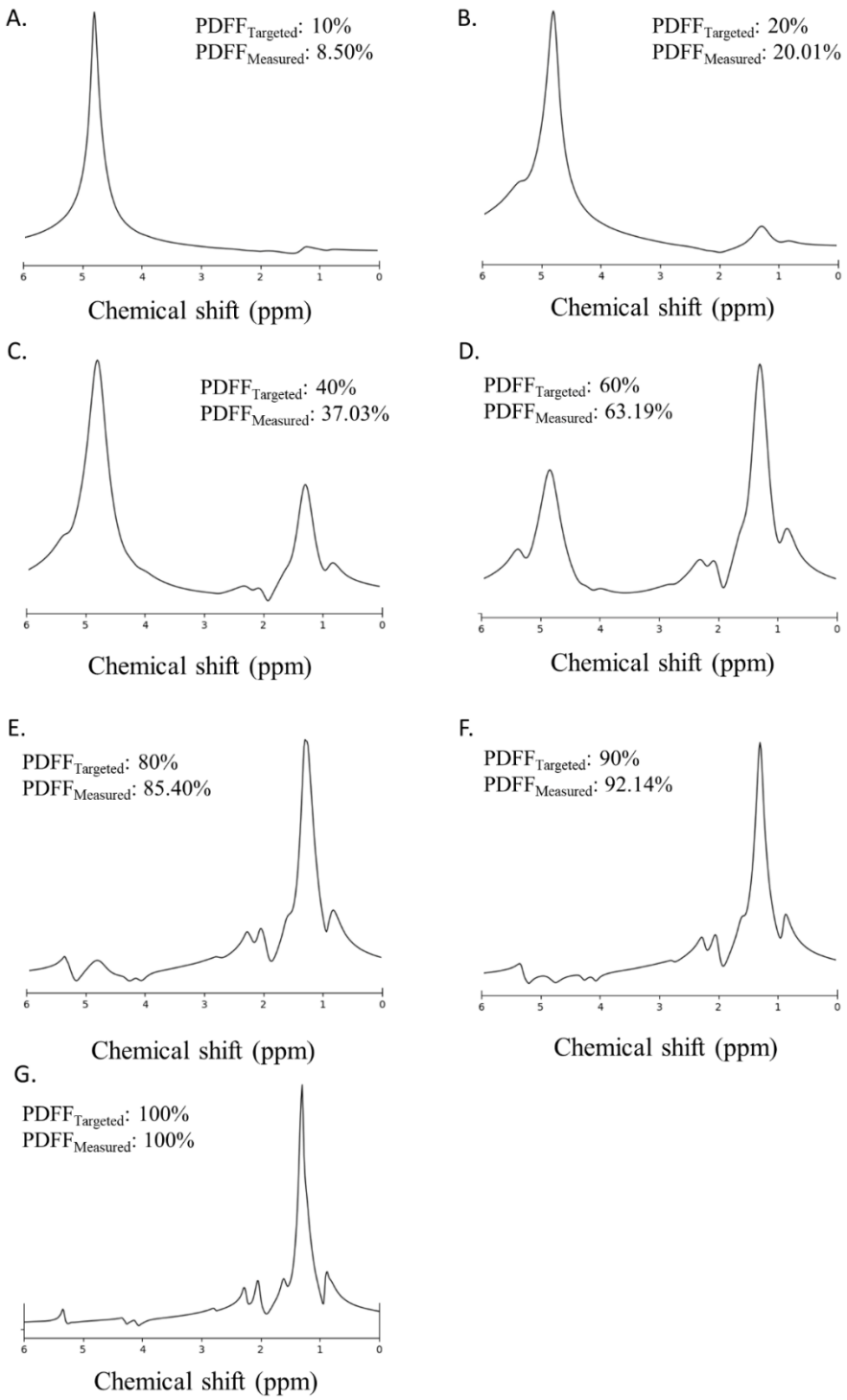

Supportive Information Figure S 3-1 : **Spectra reference for the quantification of proton-density fat fraction (PDFF) of the phantoms using non-localized FID of individual vials.** Targeted and measured PDFF values are reported for each spectrum. They were acquired using a non-localized FID with 2048 points, TR=8000ms, 4 averaging, bandwidth=10 kHz for each phantom vials.

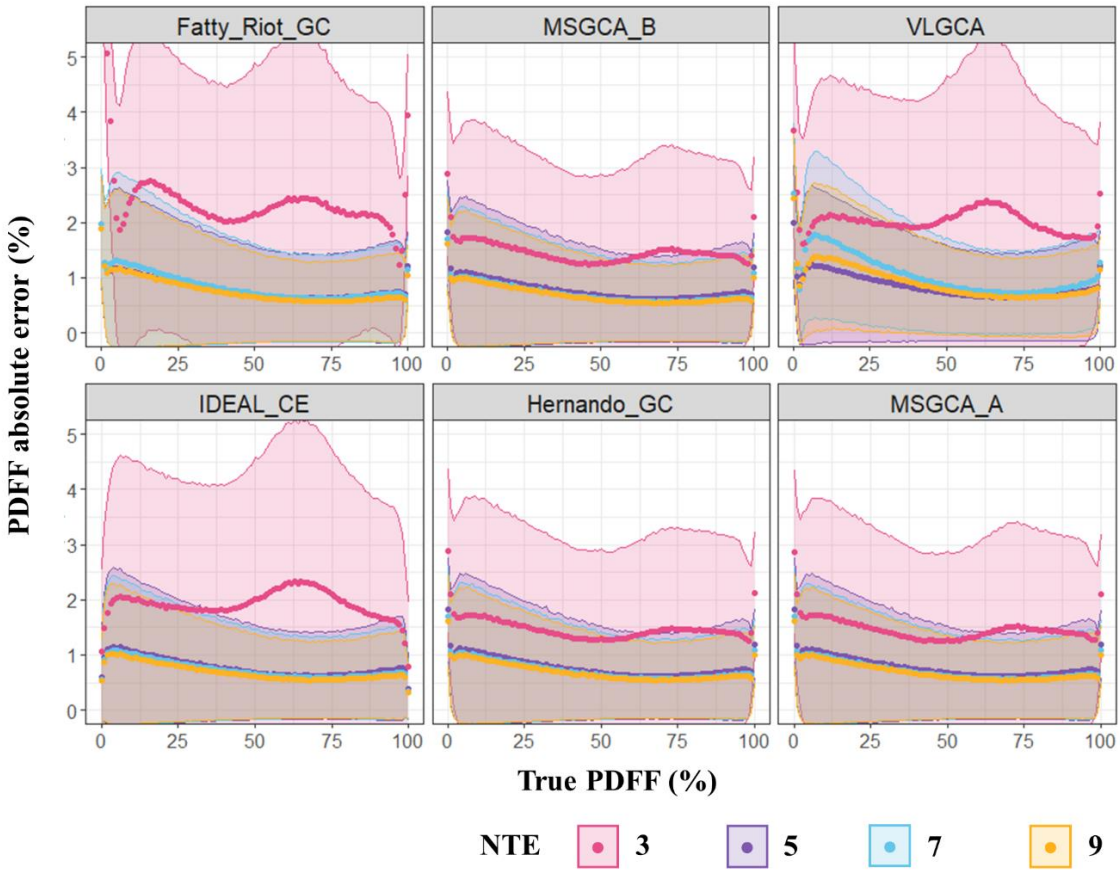

Supportive Information Figure S 3-2 : Absolute error for the PDFF quantification of simulated datasets, averaged over repetitions, the whole range of B_0 values and with SNR=50 and realistic minimal echo spacing.

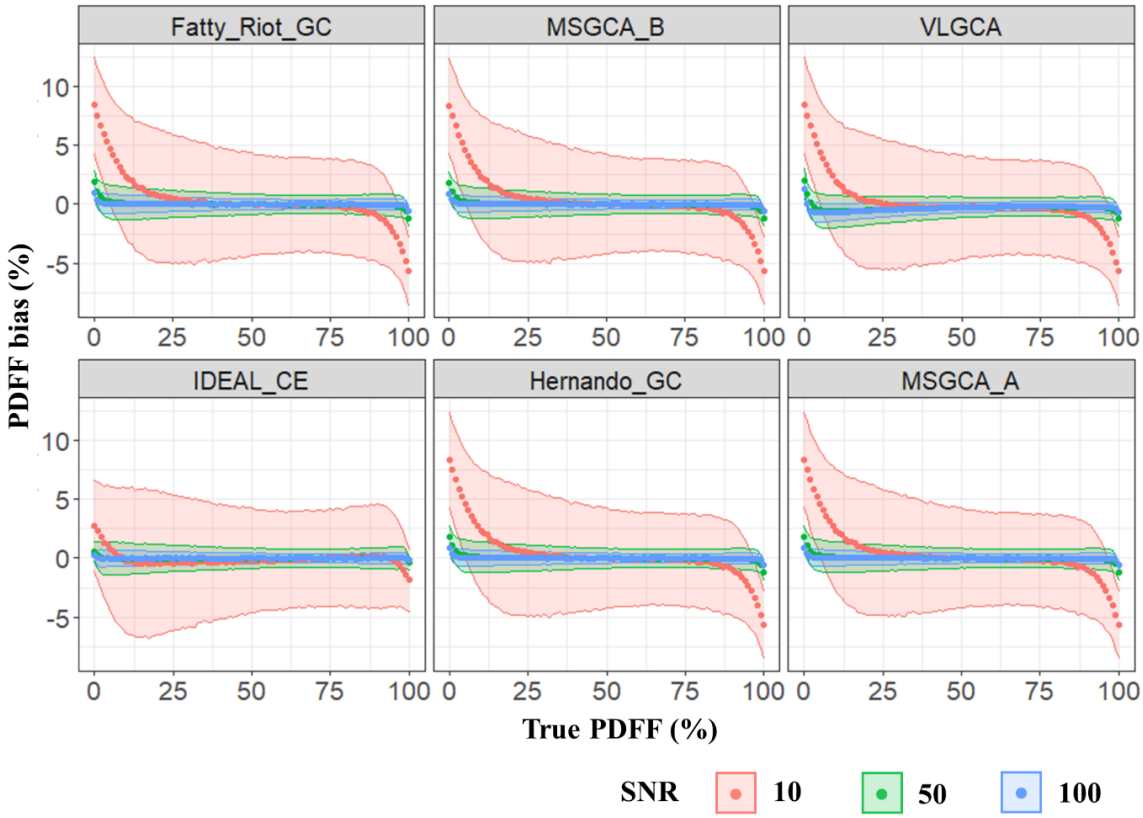

Supportive Information Figure S 3-3 : PDFF bias for the six selected algorithms depending on the input SNR of the simulated datasets with NTE=5 and realistic minimal echo spacing. All algorithms proved highly resilient to low SNR (SNR=10), with limited noise propagation in the eventual PDFF quantification.

Chapter 4 : Ex Vivo EAT characterization using MRS

4.1 Synthesis

Context & motivation

As shown in the previous chapter, the PDFF and R_2* quantification, with a stronger sensitivity from the R_2* values, could be biased due to miscalibration of the a priori multi peak spectrum that models the CSE-MRI signal. Even if a diversity of human fat NMR spectra has been evaluated, the EAT NMR spectrum has not yet been characterized. Thus, the purpose of this study was to explore the NMR signature and fatty acid profile of EAT in ex-vivo human samples.

Methods & results

Nine ex-vivo adipose tissue samples from deceased patients who donated their body to science (3 EAT, 4 VAT, 2 SAT) were acquired at 11.75T using STEAM sequence. Triglyceride model parameters (ndb, nmidb, cl) and fatty acid composition (SFA, MUFA, PUFA) were performed using a homemade Python software after quantification of lipid's peaks relative concentration.

The preliminary results on fatty acid composition suggested that EAT had a lower SFA (31.57±12.61) and higher MUFA (54.97±14.03) compared to common white fat: SAT (SFA: 49.34±4.96, MUFA 43.24±2.01 and VAT (SFA: 40.14±9.33, MUFA 43.49±7.74).

Conclusion, limits & perspectives

In this human ex-vivo study, NMR signature of epicardial adipose tissue has been evaluated. Those preliminary results in terms of triglyceride model and fatty acid composition need further investigation with a higher sample size. A confrontation of these measurements against gas chromatography analysis could also bring a clearer perspective to these results. However, after complete achievement of this study, a more reliable epicardial adipose tissue spectrum calibration could be provided for fat-water imaging and may reduce PDFF and R_2^* quantification bias for this specific fat.

Personal contributions

I conducted a thorough review of established adipose tissues characterizations using gas chromatography (**Table 1-1**) and MRS (**Table 1-3**). This study was very much a teamwork, with multiple aspects: the collaboration with endocrinology department of the AP-HM who collected the ex-vivo samples was crucial, the samples preparation, the protocol optimization and the acquisitions at 11.75T were all performed with the help of Joevin Sourdon and the interactions with Tangi Roussel, who developed the Python software, to develop and tune the spectra processing. I participated in all these steps once the samples were collected and frozen by the endocrinologists' team: I followed all experiments, I then conducted the MRS data processing, including the adaptations of the Python code to obtain desired parameters, and I prepared the tables and corresponding figures.

4.2 Introduction

The CSE-MRI signal model relies on a calibrated multi peak fat spectrum model with known a priori relative amplitudes and chemical shifts corresponding to triglycerides. Our work showed that the selection of fat spectrum reduces PDFF bias estimation and mainly R_2* bias estimation. A diversity of human fat NMR spectra was explored such as subcutaneous(36,37,39,41), bone marrow(38), liver(28,37), brown adipose tissue(42). However, to our knowledge, the epicardial adipose tissue spectra has not been yet characterized in human at the time of this study. The adipose tissue NMR spectrum can be described using a triglyceride model(28) based on only three parameters: number of double bonds (ndb), number of interrupted methylene double bonds (nmidb) and chain length(cl). Fatty acid profile (SFA, PUFA, MUFA) can be calculated from those parameters.

Therefore, the purpose of this study is to explore NMR signature and fatty acid profile of epicardial adipose in a heterogeneous population in order to improve fat spectrum calibration of CSE-MRI signal model.

4.3 Methods

4.3.1 Ex vivo Human samples

Through the collaboration with endocrinologists, instant-frozen adiposes tissues samples were excised from three deceased subjects who donated their body to science. Two were type 2 diabetics (age: 64±4 years; BMI: 31.2±5.5 kg/m^2; male\female:1\2). From each subject, fat samples included a total of four visceral fat (VAT), two subcutaneous fat (SAT) and three epicardial fat (EAT) samples. All samples were instantly frozen upon excision to avoid fat oxidation.

4.3.2 MR and MRS protocol

Spectroscopic measurements were performed on a preclinical 11.75T scanner (Bruker Avance 500 MHz/89 mm wide bore vertical imager, Ettlingen, Germany) using a 5mm diameter coil. Prior to MRS acquisition, the protocol included spatial localizers in at least

2 perpendicular plane cutting through the center of voxel of interest for identification of homogeneous fat volumes within samples in order to avoid air traps and incisions within tissue and an iterative voxel-targeted shimming procedure with the FASTEST-MAP sequence. Single-voxel MRS was performed using the STEAM sequence with voxel size 1 mm3, TE=6, 10, 20, 30, 40, 50 ms. STEAM mixing time (TM) was 20 ms, TR=1.5 s and 20 averages. It also included an outer volume suppression (OVS) preparation with six 1.5 mm-thick saturation bands.

4.3.3 MRS data processing

A home-made Python software(166) was used to post-process raw MRS data. The signal processing included: automatic channel-by-channel signal zero and first order phasing, Single Value Decomposition (SVD) channel recombination, individual spectra frequency realignment and a 5 Hz-damping apodization.

Then, the processed MRS data were quantified using a time-domain fitting algorithm(166) consisting of linear of combination of numerically computed metabolite groups (lipids and water) spectra. The pyGAMMA simulation library(167) was employed to simulate water (4.7 ppm) and lipids modeled with ten gaussian components with their corresponding chemical shifts (**Table 1-2**) using a spin-echo acquisition. The MRS model was fitted to the data using a non-linear least squares optimization algorithm resulting in relative concentration and frequency shift estimation for each peak, and a global linewidth damping and phase shift for each metabolic group. Cramér-Rao Lower Bounds (CRLB) were also estimated considering a noise level measured on the unprocessed unfiltered raw data.

T_2 was estimated for each peak of the metabolic groups on each ex-vivo samples using STEAM spectra at TE= 6, 10, 20, 30, 40, 50 ms. The following equation was used for T2 correction:

$$S_k' = S_k \times \exp(TE/T2_k)$$

where S_k is the relative concentration estimate in the VOI for either water or lipids and S_k' for the corrected relative concentration for a given biomolecule.

After T2 correction of the lipid's peaks relative concentration, the triglyceride model (ndb, nmidb, CL) was estimated using the following constraints: chain length was fixed at cl=17.29 (Hodson et al.(27), **Table 1-1**) and only the 6 most intense lipids peaks

A,B,C,D,E,F were considered for improved robustness. The ndb and nmidb quantified were then translated to fatty acids composition (SFA, UFA MUFA, PUFA).

4.4 Results

Representative spectra with the fitting model of thoracic subcutaneous fat and epicardial fat are shown in **Figure 4-1**. For both spectrum, the ten lipids' peaks are resolved but in epicardial fat there is also a water peak which is broadened compared to lipids group.

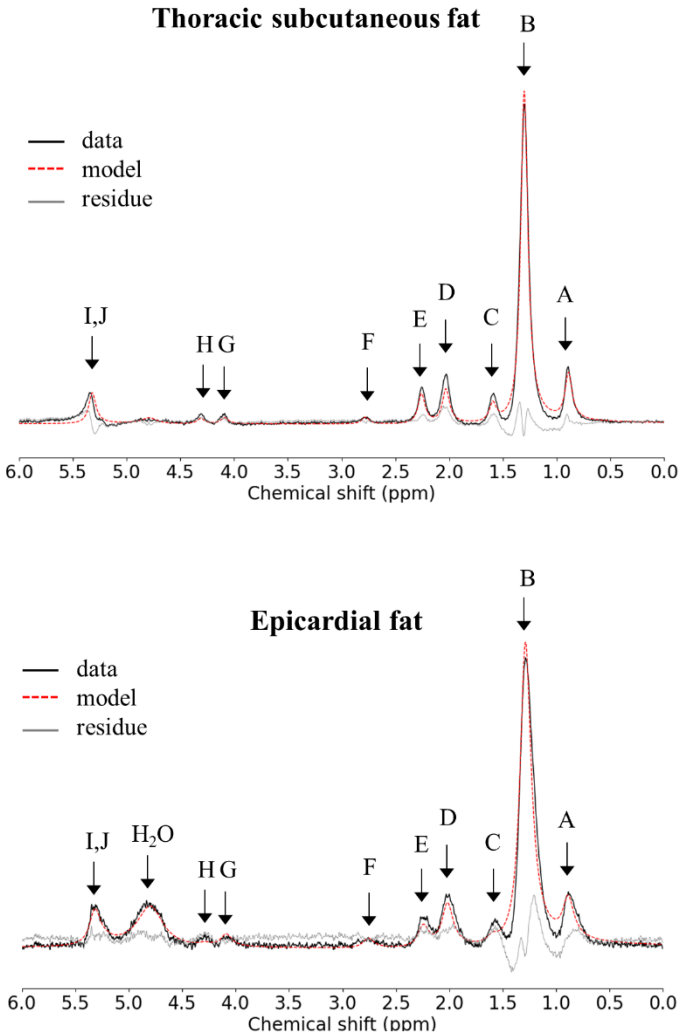

Figure 4-1: Examples of spectra obtained on thoracic subcutaneous fat and epicardial fat of the same subject. Black curves represent the spectra acquired using STEAM sequence. The fitting processing (red) was designed to quantify water (4.7 ppm)

and the lipids model (**Table 1-2**). Residual signal (grey) enables to evaluate the adequacy of the model.

As expected, and shown in **Table 4-1**, the mean T_2 value depends on the lipid peaks but due to insufficient fitting correlation (r^2 <0.90) mean T_2 of G and I lipid peaks were not estimated.

Table 4-1 : Mean and standard deviation of T_2 measured for each lipid peak. Only good fitting correlation (r^2 <0.90) are reported.

Peak		LipA	LipB	LipC	LipD	LipE	LipF	LipG	LipH	LipI	LipJ
T_2 (ms)	mean	43.71	30.51	14.91	25.09	29.31	33.88		9.47		26.49
	sd	8.70	4.86	4.24	3.66	6.69	11.08				2.67
N samples (%)		9/9	9/9	5/9	9/9	9/9	5/9	0/9	1/9	0/9	4/9

Constraint triglyceride model (ndb, nmidb) and fatty acid composition after T_2 correction are summarized in **Table 4-2** for each ex-vivo fat samples. For a same subject, there is large variation of estimation triglyceride parameters among the adipose tissue samples ($ndb_{subject\ 2}$ = 2.37±0.21, $nmidb_{subject\ 2}$=0.51±0.04, $ndb_{subject\ 2}$ = 1.88±0.29, $nmidb_{subject\ 2}$=0.25±0.18). The fatty acid composition may vary according to the type of adipose tissue (EAT, VAT, SAT). Meanwhile, preliminary results suggested that EAT had a lower SFA (31.57±12.61), higher MUFA (54.97±14.03) compared to the other type of adipose tissues (SAT SFA: 49.34±4.96, MUFA 43.24±2.01 and (VAT SFA: 40.14±9.33, MUFA 43.49±7.74) whereas PUFA from EAT (13.45±7.91) ranged between SAT one (7.42±6.97) and VAT one (16.37±1.73).

Table 4-2 : Summary of triglyceride model parameters and fatty acid composition measurements. For stability of the estimation of those parameters, fitting was constrained with cl=17.29 and only A, B, C, D, E and F lipid peaks were considered.

Subject	Adipose tissue	ndb	nmidb	SFA	UFA	MUFA	PUFA
1	VAT	2.6	0.53	31.13	68.87	51.16	17.71
	VAT (perirenal)	2.2	0.46	42.07	57.93	42.66	15.28
	VAT (thoracic)	2.49	0.54	34.98	65.02	47.04	17.98
	EAT	2.19	0.51	44.05	55.95	38.79	17.16
2	VAT	1.86	0.44	52.37	47.63	33.11	14.52
	SAT (abdominal)	2.0	0.37	45.83	54.17	41.82	12.35
	SAT (thoracic)	1.49	0.07	52.85	47.15	44.66	2.49
	EAT	2.18	0.13	31.83	68.17	63.82	4.36
3	EAT	3.0	0.57	18.84	81.16	62.31	18.84

4.5 Discussion

In this ex-vivo study, the MR properties of the human epicardial adipose tissue were explored and compared to visceral and subcutaneous ones.

As shown in **Figure 4-1**, the fitting procedure showed some limitations which could be due the a priori Gaussian lineshape instead of Lorentzian or Voigt one. This may lead to insufficient fitting correlation for T_2 estimation (**Table 4-1**).

For robustness in the estimation of triglyceride model and fatty acid composition, constraints were added with fixed chain length (cl) and limited peak analysis (only six peaks) due to the inconsistency of the results otherwise. Further work must be done for improving the fitting of those triglyceride parameters. A lead would be not to express one parameter in function of the others(168) as it had shown to potentially bias the estimation and hide relevant physiological information(41). Instead, one could impose realistic constrained such as nmidb ≤ ndb and CL, ndb, nmidb are limited in the range of realistic gas chromatography adipose tissue parameter values.

The preliminary results on fatty acid composition suggested that EAT had a lower SFA and higher MUFA compared to SAT and VAT. However, the sample size needs to be extended in order to verify this hypothesis and confirmed with gold-standard gas chromatography evaluation. Another perspective to this work is to characterize adipocyte size of EAT using diffusion weighted MRS(169,170). It has shown to discriminate ex-vivo murine brown from white adipose tissues(171), and it has also been developed for human in-vivo fat characterization at 3T(172).

4.6 Conclusions

In this human ex-vivo study, NMR signature of epicardial adipose tissue has been explored. To the best of our knowledge, this is the first MRS analysis of human epicardial adipose tissue. Those preliminary results in terms of T_2 estimation, triglyceride model and fatty acid composition need further investigation with a higher sample size, and they need to be confronted against gas chromatography analysis. After achievement of this study, a more reliable epicardial adipose tissue spectrum calibration could be provided for fat-water imaging. It may reduce PDFF and R_2^* quantification bias for this unique adipose tissue.

Chapter 5 : In vivo EAT characterization using CSE imaging

5.1 Synthesis

Context & motivation

Cardiac Dixon MRI has the potential to probe cardiac fat overload and alteration by mapping PDFF and R_2*. High-resolution 3D CSE-imaging is required to detect the pericardial fascia, layer separating epicardial fat from paracardial fat, which is better visualize at systolic time. Cardiac Dixon MRI is a challenging due to cardiac and respiratory motion, with in addition at 3T, a rapid phase accrual between water and fat concomitant with inhomogeneous B_0. To overcome this hurdle, we started a collaboration with Matthias Stuber's team at CIBM CHUV-UNIL who have developed a Free-Running framework for high-resolution cardiac imaging with fully respiratory and cardiac self-gating, combined with a multidimensional Compressed Sensing reconstruction at 1.5T.

Aiming for a precise and reliable high-resolution motion and cardiac resolved PDFF and R_2* mapping, only bipolar echoes achieved short enough echo spacing but suffered from distortions between even and odd echoes due to gradients imperfections. Thus, the purpose of this work was to propose a high resolution Free-running cardiac Dixon-MRI at 3T leveraging k-space trajectory correction by gradient impulse response function (GIRF) correction for PDFF and R_2* quantification.

Methods & results

Free-Running cardiac Dixon with 13 echoes (TE1/ΔTE = 1.12/1.07ms) in bipolar mode and 8 echoes (TE1/ΔTE = 1.16/1.96ms) in monopolar mode were acquired at 3T on a fat/water phantom and 10 healthy volunteers and one diabetic patient. Bipolar Free-Running cardiac Dixon were reconstructed with or without GIRF-correction and were compared to monopolar ones in-vitro and in-vivo in different regions of interests.

Without GIRF correction on bipolar Dixon-MRI, blurring and halo effect appeared on even echoes resulting in a non negligeable PDFF bias of 4.90% in-vitro and 23.49% in left ventricles of healthy subjects whereas with GIRF correction, those artifacts disappeared

with a precise PDFF quantification in vitro with mean bias 0.03% and more realistic one in vivo with mean PDFF of 0.78% and 0.84% in left and right ventricles. In monopolar mode, due to large inter-echo, fat-water swaps were present in-vitro and in-vivo with a less precise quantification with mean PDFF of 2.35% and 2.53% in left and right ventricles. Finally, in the healthy volunteers cohort, epicardial fat had a significantly (P <0.0001) lower fat fraction (80.36±7.10%) than the subcutaneous fat (92.49±4.25%).

Conclusion, limits & perspectives

To enable precise high-resolution PDFF and R_2*, Free-Running cardiac Dixon at 3T proved to require bipolar echoes with k-space trajectory correction achieved with the system-specific GIRF. It would have been of interest to explore more in details the k-space trajectory correction by adding the value to correct concomitant gradient effects as it is already done at low-field(173) but also applied it on monopolar Free-Running Dixon MRI. Moreover, this proof-of-concept offers the possibility to investigate epicardial adipose tissue PDFF and R_2* or furthermore, with sufficient echo times, fatty acid composition characterization in metabolic diseases resolved within the full cardiac and respiratory cycles. Moreover, it would facilitate the emergence of automatic volumetric quantification approaches of the cardiac fat.

Personal contributions

To achieve this work, we started during my thesis a collaboration with Matthias Stuber's team at CIBM CHUV-UNIL. To this end, Davide Piccini provided us the Free-Running WIP sequence that could acquire multi-echo spoiled GRE free-running data. Adele L.C Mackowiack shared her multi-echo free-running image reconstruction code (MATLAB). This reconstruction pipeline needed to be updated with the backbone of the more recent reconstruction code provided by Jérôme Yerly, that was not adapted for the multi-echo sequence. I merged, adapted and optimized the overall multi-echo Free-Running reconstruction pipeline to meet our hardware memory constraints and improve the quality of reconstructed images. For the GIRF correction, we also collaborated with Josef Pfeuffer, from Siemens thanks to the support from Thomas Troalen. Josef supplied the calibration sequence, to measure our scanner's GIRF, and the MATLAB code to apply GIRF into a 2D spiral reconstruction. I adapted this code to be applied on 3D non cartesian trajectories and integrated the GIRF correction in the reconstruction pipeline. This

integration represented quite some time since we had to retro-engineer the simulation of the gradient waveforms performed by the sequence. I also acquired and reconstructed in-vitro and in-vivo Free-Running CSE-MRI, conducted the statistical analysis, prepared all the figures.

Submission status

The following chapter is a draft article in preparation for submission in in Journal of Cardiovascular Magnetic Resonance. Before submission, we planned to improve this work on the following aspects :

- Extending the cohort study with more diabetic patients
- Extending the analysis (PDFF/R_2*) between paracardial and epicardial fat
- Exploring cardiac-respiratory status with quantitative maps (R_2*, B_0)

5.2 Introduction

There is a growing interest in probing epicardial adipose tissue (EAT), a metabolic fat surrounding the heart, which has been shown to influence pathophysiological pathways towards cardiovascular degradation in metabolic diseases(18). Chemical shift-encoded (CSE) MRI enables high resolution mapping of fatty depots(141) as well as the quantification of T2* decay. Proton Density Fat Fraction (PDFF) measurements in cardiac MRI help to identify myocardial fatty infiltration and lipomas(174). Meanwhile, T2* mapping received increasing interest in community and consensus statements(175,176) for assessment of hemorrhage(177) and iron deposition(178).

However, 3D CSE-MRI, also referred to as Dixon-MRI, is challenging in the heart due to cardiac and respiratory motion. Most 3D approaches(118,179) have been limited to a motion-free cardiac phase (end-diastole) to minimize cardiac motion artifacts, while navigator gating is used to reduce respiratory motion artifacts. Recently at 1.5T, cine 3D Dixon(119) has been developed with navigator gating. It allowed to facilitate epicardial border delineation. While benefiting from increased field-strength at 3T to boost SNR and fat sensitivity, CSE-MRI remains challenging due to rapid phase accrual between water and fat and the concomitant inhomogeneous B_0 field(180) in the heart. Thus, only single phase CSE-MRI(181) has been proposed at 3T, with a limitation to fat imaging without PDFF quantification due to the use of fewer echo times.

The Free-Running framework is a recent approach for high-resolution cardiac imaging acquiring 3D radial samples with complete respiratory and cardiac self-gating and combined with a multidimensional Compressed Sensing reconstruction(182). It circumvents the need for respiratory navigation by using a self-gated superior-inferior projection, which can also be employed for cardiac-gating. This framework has demonstrated its capacity for motion-resolved high-resolution cardiac MRI, particularly to target demanding coronary imaging(45) or 5D-Flow MRI(183). Considering the preference for the visualization of epicardial fat in systole(184), due to the myocardium pulling the thin fat layer away from the pericardium sack, thus enhancing EAT delineation, we hypothesized that the Free-Running framework lays ground for high-resolution quantitative cardiac Dixon-MRI at 3T. We demonstrate that, at 3T, accurate PDFF quantification of the fat surrounding the heart can only be achieved with bipolar multi-

echo times compared to monopolar echo times. However, bipolar Free-Running Dixon suffered from distortions between odd and even echoes due to gradient imperfections.

Gradient imperfections-related distortions stand as a well-known hurdle in MRI, and in particular in non-Cartesian MRI. Recently, correction using the gradient impulse response function (GIRF)(185,186), which fully characterizes the gradient system temporal response, has emerged and demonstrated its value to correct all kinds of non-Cartesian k-space trajectories(187).

Thus, the Free-Running cardiac Dixon image reconstruction was extended with k-space trajectory correction using GIRF, which enabled high-resolution quantitative cardiac Dixon at 3T.

5.3 Materials and Methods

5.3.1 MRI acquisition

A custom-written prototype 3D radial spoiled gradient echo sequence was implemented with multiple echoes and a phyllotaxis trajectory for integration with the Free-Running framework(182). CSE-MRI data were acquired on a 3T MRI system (Magnetom Vida, equipped with XE gradients, Siemens Healthcare, Erlangen Germany) with the spine coil array and an 18-channel body coil array.

Aiming for a TR of 15ms, which has been shown to suffice for quantitative characterization of abdominal fat, including an accurate T2* value(188), 13 echoes (TE1/ΔTE = 1.12/1.07ms) in bipolar mode and 8 echoes (TE1/ΔTE = 1.16/1.96ms) in monopolar mode were acquired with the following parameters. For a precisely 10 min 38s acquisition, 40014 radial views per echo (13 segments, 3078 Shots) were acquired with FOV=$(220mm)^3$ at isotropic $(1.5mm)^3$ resolution, FA=5°, BW=1510 Hz/px for all echoes.

5.3.2 In vitro: fat water phantom

A homemade fat-water phantom consisting of eight 50mL vials with different fat fractions of peanut oil (0, 8.50, 20.01, 37.03, 63.19, 85.40, 92.14, 100%) was acquired using a 20-channel head coil to validate the methods quantification. The targeted volume percentages of oil were corrected with magnetic resonance spectroscopy, with exact

values of 0, 8.50, 20.01, 37.03, 63.19, 85.40, 92.14, 100%. Spectroscopy data were acquired on a 3T MRI system using a non-localized FID with TR=8000ms for each phantoms vials.

Phantoms vials were aligned along the static magnetic field direction, and iterative shimming was performed prior to the acquisitions. SNR was measured in the vials over a 3D region of interest and defined as the mean signal divided by the standard deviation.

5.3.3 Numerical Simulation

Given chosen acquisition parameters (MONOPOLAR: NTE/TE1/ΔTE= 8/1.16ms/1.96ms, BIPOLAR : NTE/TE1/ΔTE =13/1.12/1.07ms), PDFF and R_2* quantification precisions were evaluated by feeding synthetic CSE-MRI data y to the fat-water separation algorithm modeled as:

$$y = \left(W + F \sum_{m=1}^{m} \alpha_m e^{i\omega_m t} \right) e^{(i(\omega_0+\varphi_0)-R2^*)t} + N(t)$$

with W=(1-PDFF) and F=PDFF corresponding to normalized water and fat absolute signal, ω_0 the off-resonance, $\varphi_0 = 30°$ the initial phase, $R_2^* = 50\ s^{-1}$ the transversal decay, N(t) the complex gaussian noise (with SNR=10 or 50) and α_m, $e^{i\omega_m}$ the relative amplitudes and frequency offsets of a subcutaneous fat spectrum respectively. The virtual CSE-MRI data were synthesized as volumes using an open-source toolbox(ref) with: along the x-axis, PDFF 0:1:100%, along the y-axis, uniformly distributed B_0 -200:4:200Hz, and the z-axis consisted in 100 repetitions. Synthetic volumes were normalized based on 99% of the maximum of the first echo. To avoid border effects due to spatial regularization, a five pixels padding was added for each CSE-MRI volume.

5.3.4 Study Population

Ten healthy volunteers (age: 36±12 years; BMI: 22.9±1.7 kg/m2; male\female: 8\2) along with one diabetic patient (age=60;BMI=38.05 kg/m2 male\female: 0\1) were recruited in this study after informed consent.

5.3.1 GIRF measurement

The system-specific Gradient system Impulse Response Function (GIRF) was measured using the 2-offcentered slices method on a spherical phantom placed at isocenter

(189,190). The Free-Running sequence gradients waveforms (**Figure 5-1.A**) were corrected using multiplication in the frequency domain between the GIRF. Temporal integration provided the actual k-space trajectory(**Figure 5-1.B**).

5.3.2 Image Reconstruction and Quantitative fat-water mapping

Cardiac and respiratory motion signals were extracted from the first echo of the superior-inferior projections(182). Data were binned in 4 respiratory phases and 100ms-wide cardiac phases. The 6D binned k-space data were reconstructed using the Free-Running compressed sensing framework(182). Based on 3D radial Nyquist criteria, individual Free-Running Dixon data were accelerated by a factor R=26 for 8 cardiac phases and 4 respiratory state.

Complex images from each bin were processed for fat-water separation using Iterative Decomposition of water and fat with Echo Asymmetry and Least square Estimation (IDEAL) method with constrained extension(70). Computations were performed in MATLAB R2019b with a computer equipped with a GPUs (Nvidia Quadro RTX 6000, 24Gb) and 48 CPUs (Intel Xeon Gold 5220R, 2.20Ghz).

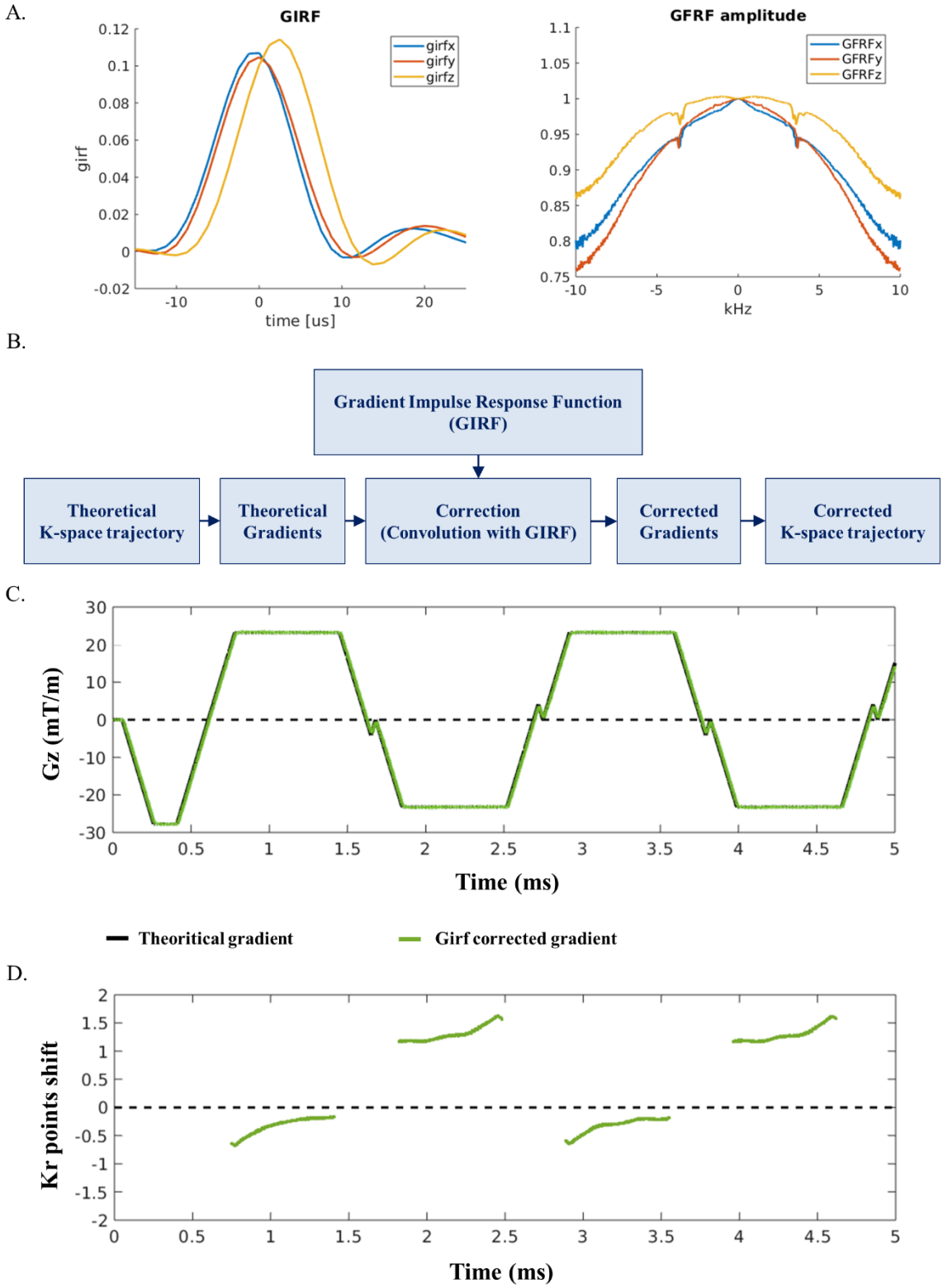

Figure 5-1 : Trajectory correction using system-specific gradient impulse response function (GIRF) : (A) Measurement of the GIRF and the magnitude of its Fourier transform (GFRF) ; (B) K-space trajectory correction pipeline (C) applied for the first four echoes in bipolar mode. (D) Converting distorted gradients into k-

space trajectory showed up a mean shift superior to 1 for even echoes. GIRF-corrected trajectory prevents this error at the image reconstruction level.

5.3.3 Evaluation metrics and statistical analysis

Difference between monopolar and bipolar acquisitions were evaluated in-silico and in-vitro using standard metrics (bias, precision) on PDFF maps. For in-vivo evaluation of the performances of the proposed correction, different regions of interests (ROI) were manually segmented on CSE-MRI using im3Dtools v3.0(191) in MATLAB: Right(RV) and Left(LV) ventricles, septum, liver, bone marrow, subcutaneous (SAT), epicardial and paracardial (PAT) adipose tissue.

Statistical analysis was conducted using R (version 3.6.3) (134). The metrics' distribution normality was assessed using the Shapiro-Wilk test. Paired Wilcoxon signed rank and Wilcoxon rank sum tests were used to investigate significant differences for each quantitative parameters between monopolar mode and bipolar one with or without correction.

5.4 Results

5.4.1 GIRF measurement results

Figure 5-1.A depicts the GIRF and the magnitude of its Fourier transform (Gradient Frequency Response Function) at low-frequency in all three axes. The magnitude GFRF revealed the mechanical resonances of the gradients coils between 3.3khz and 4kHz and a decreasing loss transfer function at high frequencies for all axes, impeding fast gradients switching such as in bipolar echo mode. Moreover, gradient response function is also depending of the axis. Indeed, the GIRF reveals a 2.5 µs delay in z direction whereas in frequency domain x,y gradient direction had a lower transfer function than the z one, indicating anisotropic eddy-current effects.

The GIRF correction revealed subtle oscillations on gradient waveforms (**Figure 5-1**.C) and a mean shift of sampled point in k-space trajectory of 1.28 and -0.34 for even echoes and odd ones respectively (**Figure 5-1**.D). Odd echoes were less impacted thanks to a sequence-level calibration for the 1st echo and balanced errors between odd and even gradients.

5.4.2 Echo spacing scheme

At 3T, despite a high bandwidth and modest matrix size, monopolar echoes (n=8) were unable to reach an echo spacing (ΔTE=1.96ms) shorter than the required in-phase/out-of-phase 1.24ms delay (green markers in **Figure 5-2**). Only bipolar echoes (n=13) achieved short-enough echo spacing (ΔTE=1.07ms).

However, in bipolar mode without correction strong artifacts, including strong signal modulation over the image and signal losses in certain regions as well as blurring of details, appeared between odd and even echoes (**Figure 5-2**). After GIRF trajectory correction, artifacts disappeared on CSE-MRI images, providing consistent visualization throughout echo times.

5.4.3 Numerical simulations

As shown in **Error! Reference source not found.**.A, with a SNR=50, PDFF and R_2* q uantification is accurate with both 13 echo times or 8 echo times, with a mean PDFF and R_2* bias less than 0.01% and 0.01 s^{-1} respectively. However, with a lower SNR of 10, fat-water swaps are present for PDFF>85% in monopolar mode whereas PDFF quantification is still precise for bipolar mode with a mean PDFF bias of 0.03%. Expectedly, PDFF absolute error significantly (P <0.0001) decreased with 13 echoes compare to 8 echoes from 0.7 % to 0.49% and from 3.84 % to 2.38% for SNR=50 and 10 respectively. Meanwhile, **Error! Reference source not found.**.B revealed that R_2* quantification was d ependent of PDFF with more imprecision in the 50% to 80% range with a maximum absolute error of 3.95 /19.81 s^{-1} with 8 echoes compared to 2.47/12.39 s^{-1} with 13 echoes at SNR=50/10 respectively.

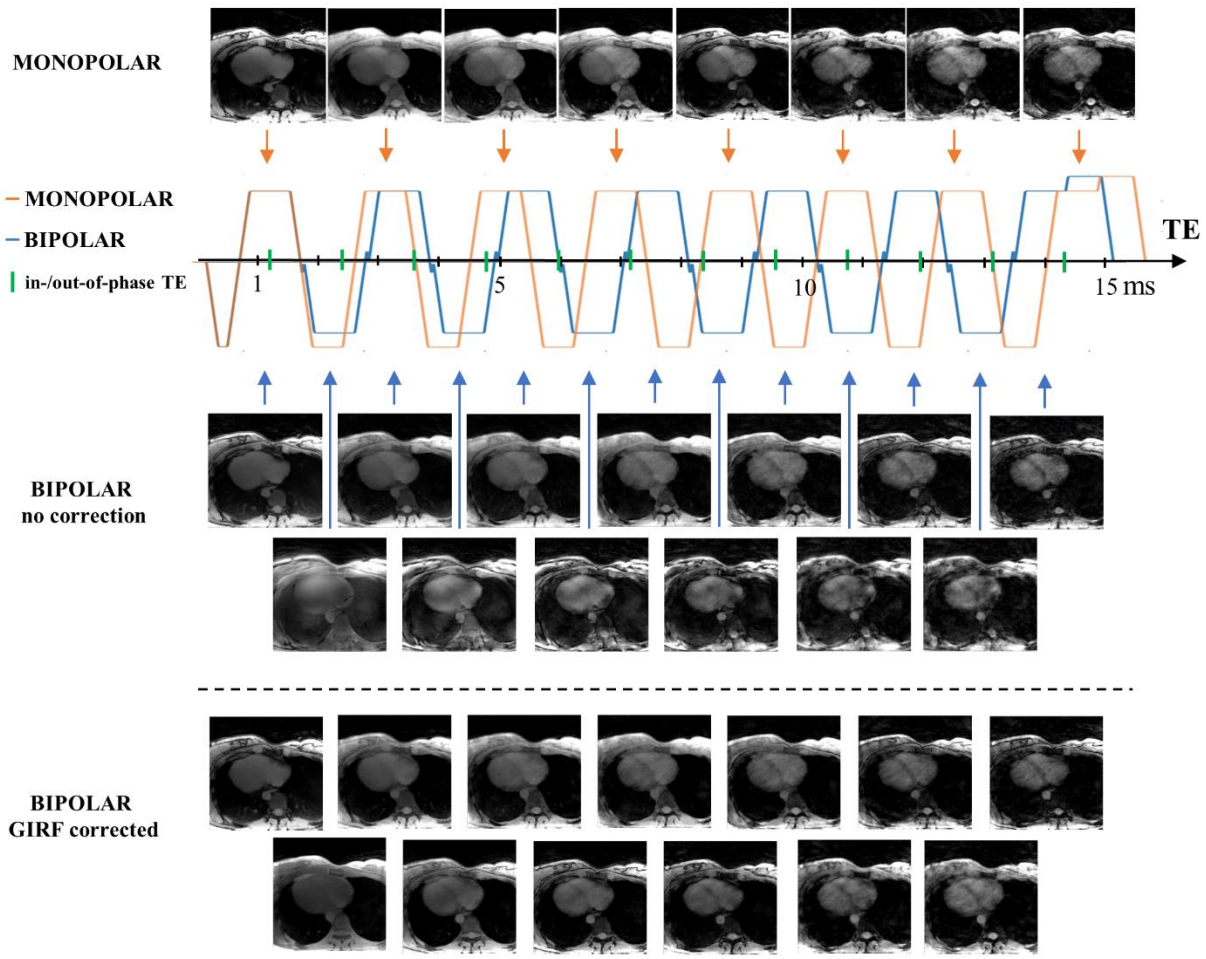

Figure 5-2 : Free-running Dixon-MRI echo times repartition depending on the multi-echo scheme, before and after GIRF correction. Monopolar echo spacing was longer than the fat-water in-phase/out-of-phase delay at 3T. In bipolar mode without correction, strong artifacts appeared on even echo images but after GIRF correction image quality was restored.

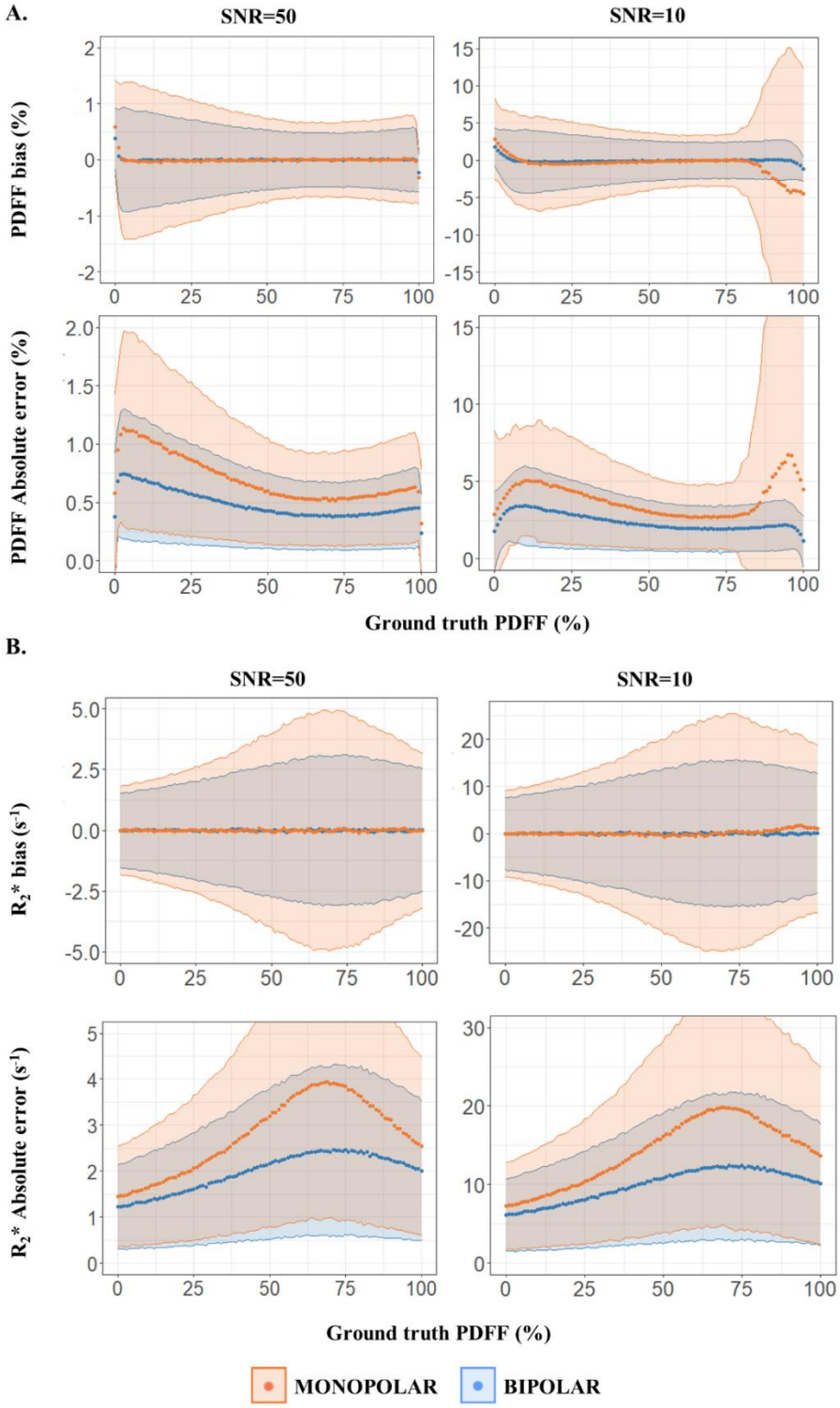

Figure 5-3 : Comparison of PDFF (A.) and R_2* (B.) bias and absolute error between 8 echoes in monopolar compared to 13 echoes in bipolar over synthetic CSE-MRI volumes with SNR=50 and 10. Mean and standard deviation PDFF and R_2* bias and absolute error were averaged along the B_0 off-resonance and repetition axes.

5.4.4 In-vitro experiments

Experimental SNR measured in the phantom varied across vials between a minimum of 10 and a maximum of 50. Confirming simulation results, fat/water swaps are presents in vials with PDFF > 85% for monopolar mode. Corrected bipolar mode provided more reliable results with a mean bias of -0.36±1.90% compared to monopolar mode with -5.25±13.07%. Without correction, bipolar mode PDFF maps suffered from non negligeable bias (4.90±4.36%).

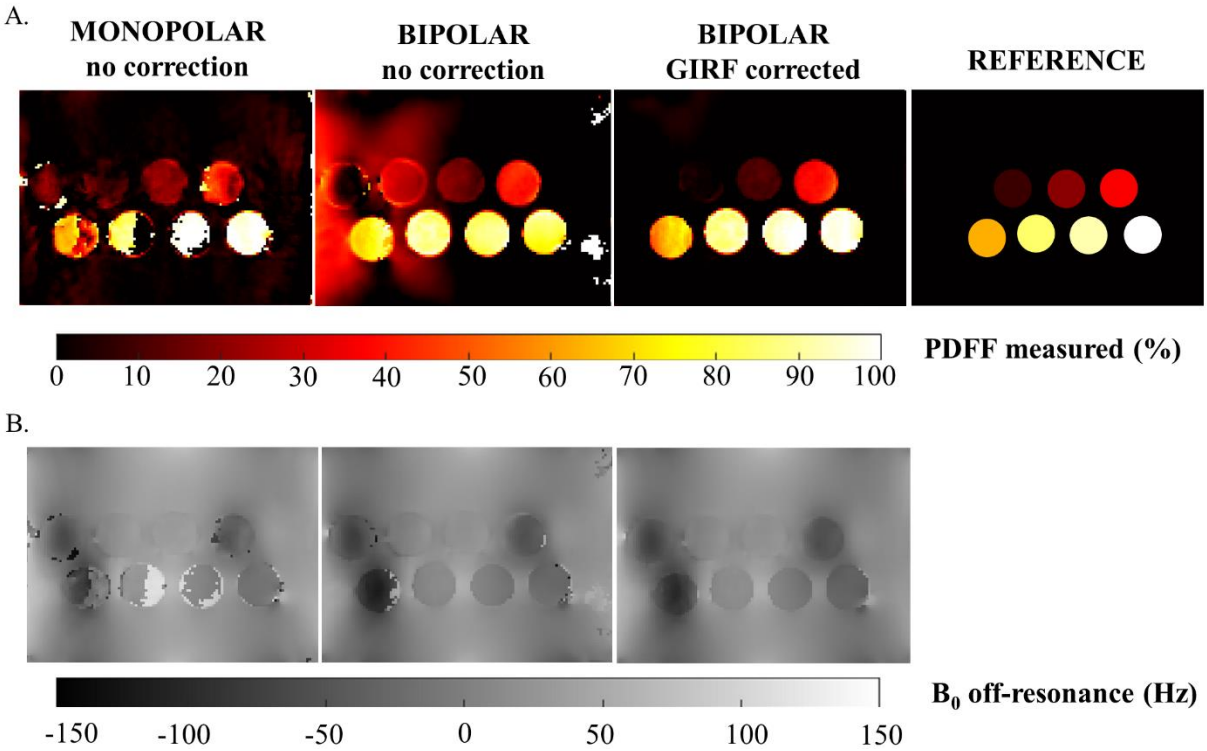

Figure 5-4: PDFF (A.) and B_0 off-resonance (B.) measurements from in-vitro experiments with monopolar and bipolar with or without GIRF correction.

5.4.1 In-vivo experiments

Without GIRF correction, in vivo fat and water images were incorrectly reconstructed with blurring at the apex and around the atria, massive swaps between fat and water (**Figure 5-5**). It would resulted in non-realistic quantitative maps (B_0 offset, R_2* and PDFF) all along the cardiac (**Figure 5-6**) and respiratory cycle (**Figure 5-7**). On contrary with GIRF correction, fat water swaps disappeared and fat content is not overestimated in the heart no matter the cardiac and respiratory states. Besides, quantitative maps

obtained with the monopolar acquisition still suffered of non-realistic values causing bias in PDFF and R_2* quantification.

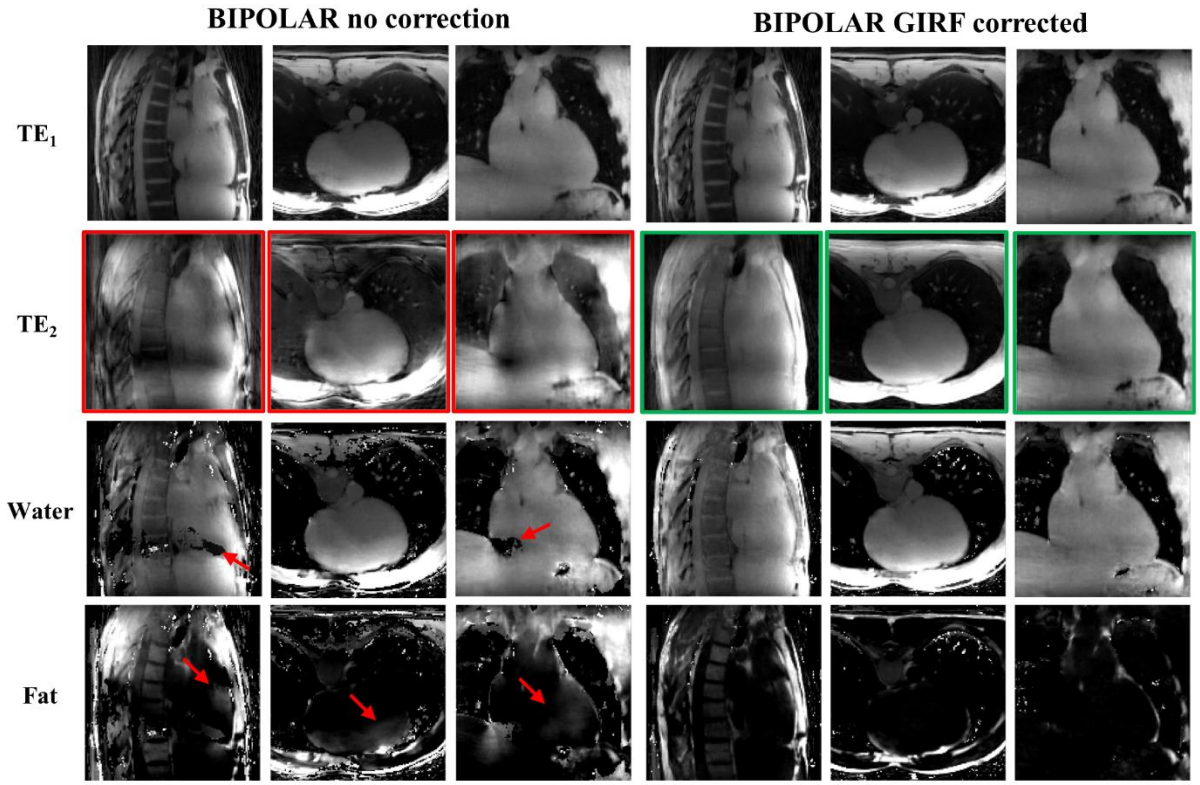

Figure 5-5 : Impact of GIRF correction on free-running bipolar Dixon-MRI on in-vivo data. Artifacted even echoes (2nd echo presented only) are highlighted in red. Radial artifacts were reduced in GIRF-corrected images, corresponding to an almost in-phase image in vivo.

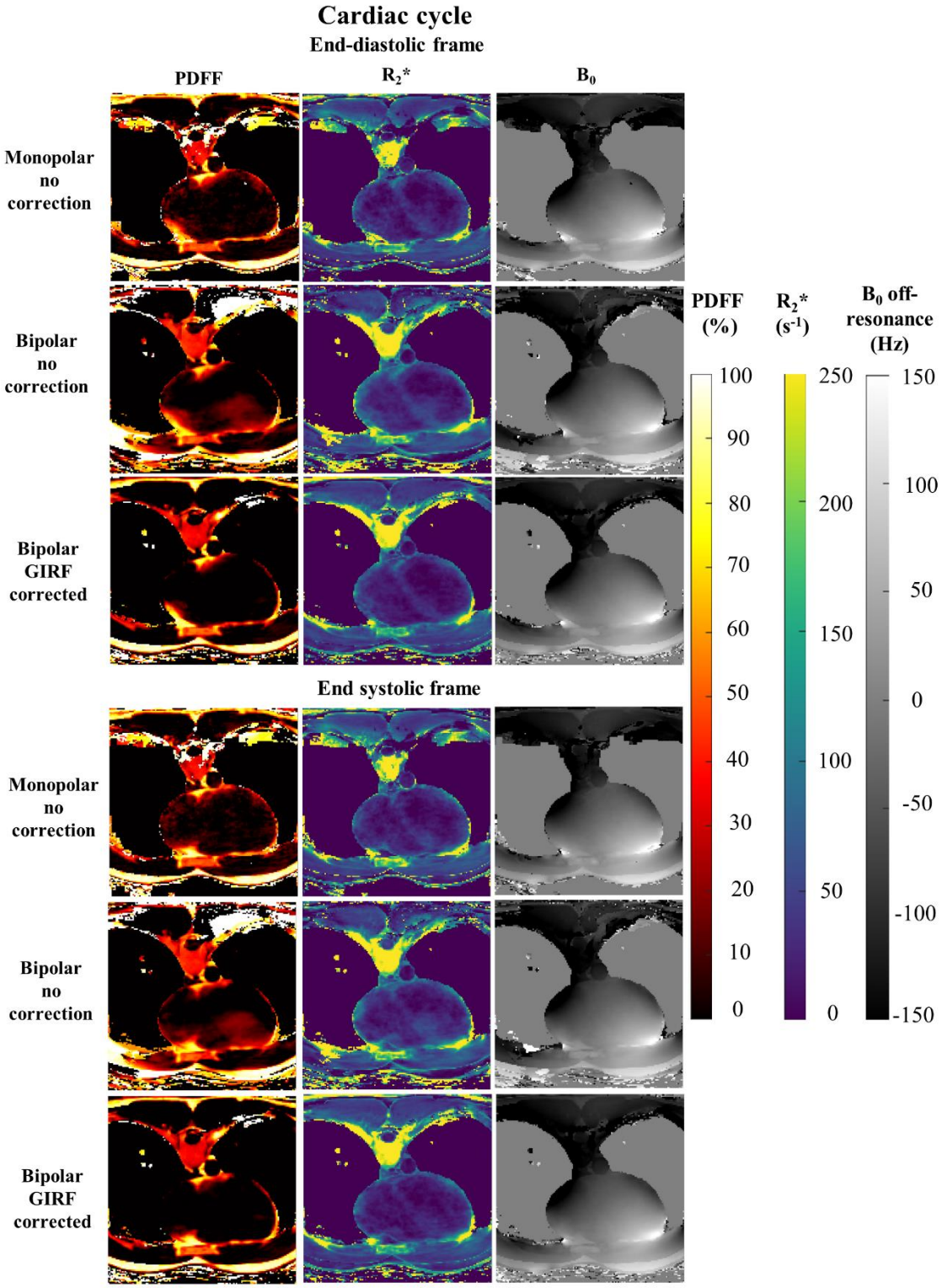

Figure 5-6 : Across the different phases of the cardiac, quantitative PDFF and R_2*, B_0 off-resonance maps in axial view resulting from monopolar, bipolar with or without GIRF correction. Inadequate monopolar echo spacing as well as uncorrected bipolar data led to spurious PDFF overestimation with fat-water swaps.

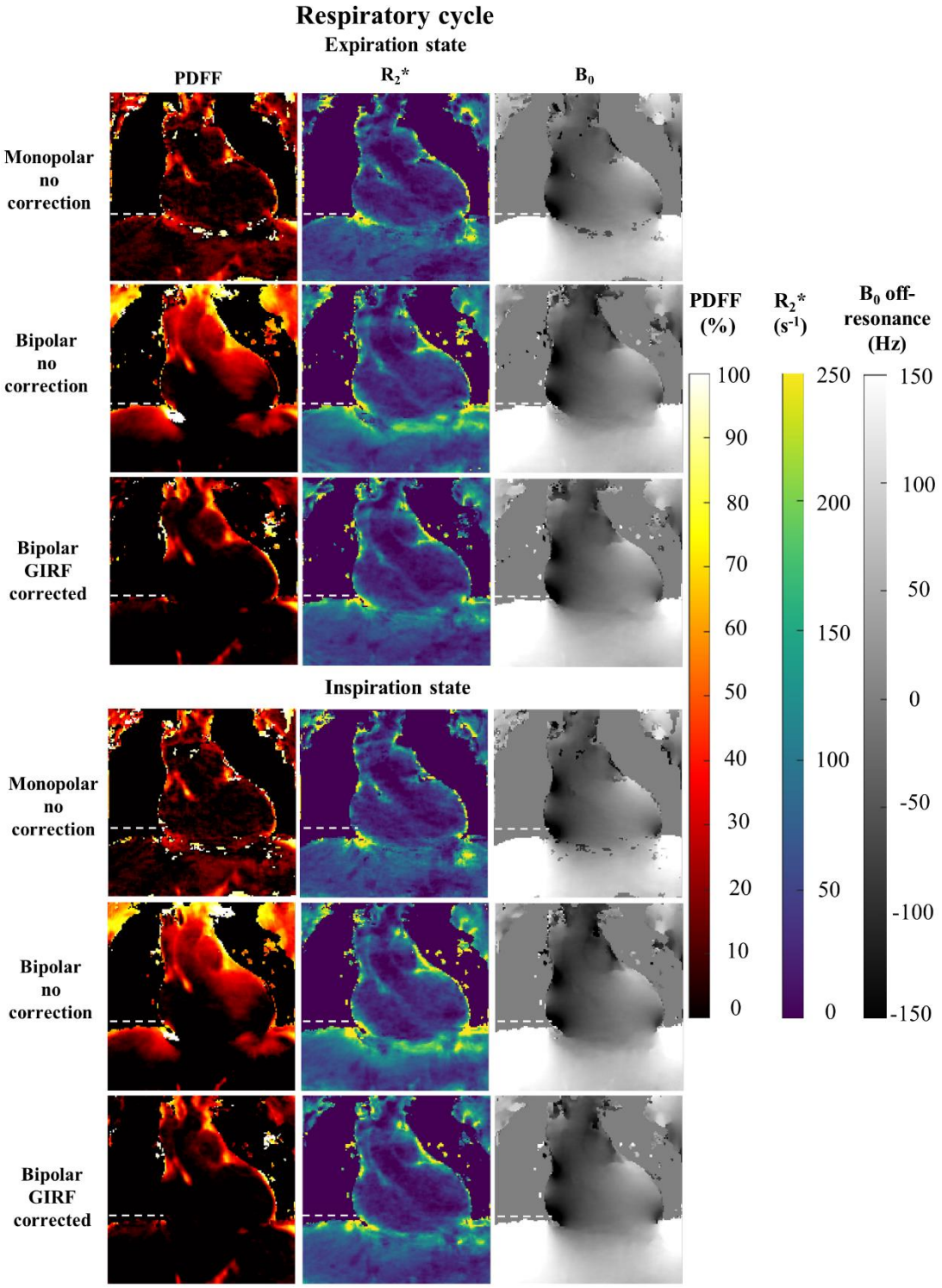

Figure 5-7 : Across the different respiratory states, Quantitative PDFF and R_2*, B_0 off-resonance maps in coronal view resulting from monopolar, bipolar with or without GIRF correction. The dotted white line represents the diaphragm level at expiration state.

Therefore, for instance with non-corrected bipolar, fat content is overestimated in tissues with negligible expected adiposity: mean PDFF of 23.49% and 17.52% was measured in the left and right ventricles respectively (**Figure 5-8**). On contrary with correction, mean PDFF in those ROIs were more realistic with a PDFF lower than 1% (LV: 0.78% RV : 0.84%) whereas in monopolar mode it was superior to 2% (LV:2.35 RV:2.53).

In the healthy population, epicardial fat have a significantly(P <0.0001) lower fat fraction than the subcutaneous fat (PDFF EAT : 80.36±7.10% and PDFF SAT=92.49±4.25% in bipolar). Only present within two healthy volunteers, paracardial fat PDFF (92.49±3.34%) tended to be superior to EAT PDFF. Bipolar GIRF corrected PDFF values are more precise and homogenous across cardiac and respiratory cycle compared to the monopolar one with a significantly(P <0.0001) lower standard deviation (sd PDFF=1.23%, sd PDFF=2.70% monopolar).

The preliminary results with the diabetic patient suggested that she had also a lower fat fraction of EAT (86.35±5.00%) compared to the subcutaneous fat (96.34±3.06%) or paracardial fat (92.48±2.90%) (**Figure 5-9**).

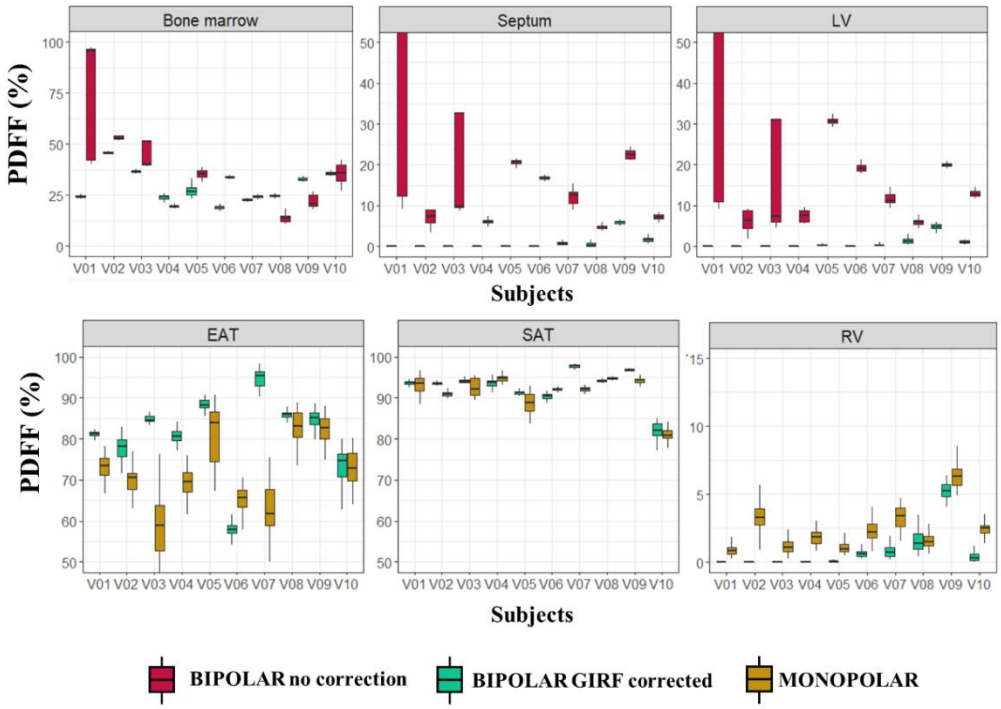

Figure 5-8: PDFF measurements over different regions of interests across the volunteers resulting from bipolar with or without GIRF correction and monopolar

echoes. Boxplots showed the consistency of PDFF measurements along cardiac and respiratory cycle.

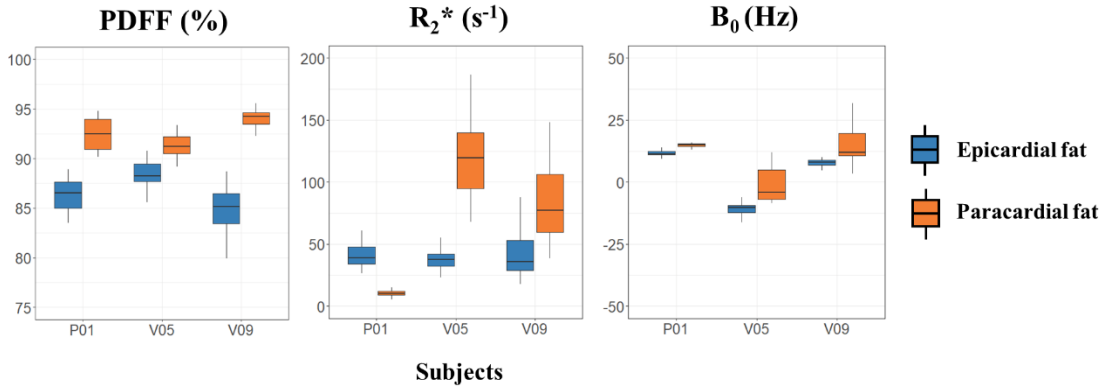

Figure 5-9 : PDFF, R_2*, B_0 off resonance measurements in epicardial and paracardial fat across patients and healthy volunteers.

5.5 Discussion

We demonstrated in this study the value of Free-Running cardiac Dixon at 3T for high-resolution high-precision 3D quantitative cardiac fat and water imaging. However, the full potential of Free-Running Dixon at 3T could only be achieved with bipolar echoes, which required a correction with the system-specific GIRF to prevent radial-trajectory image artifacts.

In monopolar mode, large inter-echo times (1.96ms), superior to in/out phase echo spacing, led to fat-water swaps in low SNR regions in-silico, which were confirmed in-vitro in vials superior to 85% of fat fraction. As shown in **Figure 5-4.B**, B_0 field map estimation error could cause those swaps. In contrary, with thirteen bipolar echoes obtained in a 15ms single TR with ΔTE=1.07ms, reliable PDFF measurement were obtained in simulation and in vitro.

Epicardial adipose tissue overload has been established as a biomarker of Coronary Heart Disease (CHD). Its volumetric quantification using high resolution 3D Dixon has been already proposed in the past at 1.5T(119) and 7T(192). Our approach distinguished from those works by targeting a precise PDFF quantification of EAT leveraging 13 echoes, allowing a differentiation of this unique adipose tissue from its neighbour paracardial fat(**Figure 5-9**). Quantitative PDFF might offers refine insights in the characterization of

EAT, possibly determining EAT 'colour' of adipose tissue (between brown, beige or white) as brown adipose tissue has been shown to have a lower PDFF than white adipose tissue(193,194). Further investigation leveraging the 13 echoes could also provide valuable FAC characterization(36,195).

Free-Running cardiac Dixon also provides with the full cardiac and respiratory cycles, which offers multiple benefits: 1/ to study epicardial fat, systole is often preferred since pericardium is thicker and better separate EAT from paracardial fat, 2/ the respiratory phase with minimal B_0 inhomogeneity can be chosen for analysis, limiting local signal loss and phase accumulation and 3/ variations of R_2* along the cardiac cycle hold interest, in the myocardium to detect ischemia(196), but also between right and left ventricular blood pools to probe cardio-respiratory status(197).

While high resolution 3D Dixon acquisition are not included in routine cardiovascular MRI protocols, this particular acquisition might be motivated in several applications as stated above. For example, a rapid automatic 2D evaluation of EAT on routine MRI cardiac images has already been proposed(198) and could inform of EAT overload to motivate a finer 3D quantitative PDFF assessment in certain cardio-metabolic diseases.

Although different strategies could have been used for correcting k-space trajectory(89,199), starting simply with constant and linear corrective factors, we opted for the GIRF method(187) which have proved to provide a more robust and precise correction. Beyond gradient imperfections, non-Cartesian k-space trajectories are also sensitive to gradient concomitant field effects and static field inhomogeneities. Concomitant fields were considered minor at 3T, but they could be corrected in addition to GIRF(173). And due to the very short individual readout duration (~1ms), static field inhomogeneities have a minor impact on the trajectory, although a correction(200) embedded in the non-uniform FFT could also be integrated in the Free-Running framework.

A major limitation of this work remains the elongated reconstruction time. Indeed, due to large amount of data (more than 20Gb) for each acquisition, each echo has been reconstructed independently with a computation time of 3h 20 min per echo using GPU. Fortunately, technical advances in image reconstruction hold hope for massively reducing this time.

Due to high susceptibility-induced field of the lung, B_0 inhomogeneities field map had large variations influencing R_2* quantification (**Figure 5-6**,**Figure 5-7**,**Figure 5-9**). To

compensate this confounding factor, it would be of interest to integrate a priori information of the scanner magnetic field distribution(76,164) to improve the robustness of the B_0 field map estimation and correct R_2* quantification(201).

5.6 Conclusions

This study aims at providing precise high-resolution PDFF and R_2* quantification, achieved using Free-Running cardiac Dixon at 3T. Bipolar echoes proved to significantly outperform monopolar echo mode, but required k-space trajectory correction using the gradient system specific GIRF characterization. It enabled to investigate epicardial adipose tissue PDFF and R_2*, showing a significantly lower fat fraction (80.36±7.10%) compared to subcutaneous fat (92.49±4.25%) in the healthy cohort.

General Conclusion and Discussion

Motivated by the growing interest of epicardial fat imaging to assess its role in cardiovascular degradation in metabolic diseases, the problematic of this thesis was to develop epicardial fat MRI to quantify and characterize this unique adipose tissue. Indeed, while epicardial adipose tissue plays a cardio-protective role in healthy subjects, it shifts towards an inflammatory substrate under pathophysiological conditions, notably in diabetes, promoting the development of cardiovascular diseases. Therefore, the ability to access in-vivo information of epicardial fat has the potential to bring fundamental value to the diagnosis of cardio-metabolic risks.

Cardiac MRI appears as a method of choice owing to its evaluation of heart's anatomy and function, generation of different contrasts with quantitative information, and non-invasive feature allowing multiple explorations. However, epicardial adipose tissue is often overlooked in cardiac MRI.

In this context, this thesis was built upon three pillars: 1/ the understanding of the needs from clinicians to include EAT in their diagnosis, 2/ the acknowledgement of technical and practical hurdles to be lifted to facilitate the consideration of EAT in cardiac MRI and 3/ the push for innovative metrics to further probe EAT, leveraging cardiac MRI.

1/ First, I conducted a thorough review on epicardial adipose tissue fat from the perspective of its physiology, acknowledging its features as a fatty tissue and its implications in cardiovascular risks. Upon the identification of biomarkers of EAT (quantity and color feature) regarding its pathophysiological role in cardiovascular diseases, I investigated in depth how EAT can be imaged in radiology and how these biomarkers are characterized and analyzed.

Second, we considered the evaluation of accumulation of EAT to be essential in routine cardiac MRI. That is why we developed, using deep learning approaches, a rapid and automatic quantification of EAT on standard cardiac images (four-chamber cine). To be clinically relevant, this tool was validated over a heterogeneous database including healthy subjects, type-2 diabetic patients and non-diabetic obese patients. And to facilitate its integration, we implemented the network as a 'one-click' plugin in an open-

source software FSLeyes. Although we showed this area measurement enables to relatively detect overload of EAT, a precise volumetric quantification remains desired.

Third, the proof of concept of 1.5 mm^3 isotropic Free-Running Dixon-MRI was developed and evaluated during this thesis, allowing to meet these expectations. This new acquisition lays ground to automatic 3D quantification of EAT in cardiac MRI, albeit at the cost of a 10-min long dedicated acquisition. Moreover, the recent clinical literature points towards the EAT quantity not being the sole biomarkers of interest, but also the EAT endocrine activity (pro-inflammatory, pro-fibrosis) that contributes to the development of cardiovascular risk. From a macroscopic view, the color feature (white, beige, brown) and the fatty acid composition of EAT may also inform of the healthiness of subjects. Quantitative biomarkers of adiposity (PDFF) and iron overload (R_2*) have been shown to discriminate, in supraclavicular zone, brown from white adipose tissues(193,194). As EAT is a unique adipose tissue of varying "color", the high precision imaging of those quantitative biomarkers was our guiding principle in order to detect subtitle modifications. For this reason, we have worked for a high-resolution, precise and reliable quantitative maps (PDFF and R_2*) resolved along cardiac and respiratory cycles to probe EAT. In addition, we developed a bi-language (MATLAB and Python) open-source toolbox during this thesis to standardize the comparison between the state-of-the-art of fat-water signal separation algorithms, eventually to elect the optimal algorithm(70) that ensure clinical precision.

Recently, in-vivo MRI based methods that estimated fatty acid composition had raised interests from the research and clinical community. Indeed, it may offer a better understanding of the role of EAT FAC in CVD. Thus, in collaboration with the endocrinology department of the AP-HM, we began an analysis of ex-vivo human EAT samples to explore its NMR signature and fatty acids composition profile. Moreover, the thirteen echoes of our Free-Running Dixon offer the possibility of further characterization of EAT with imaging of fatty acid composition.

In perspective of fully clinical integration, this work would greatly benefit from an online reconstruction and direct evaluation on the scanner, using Siemens' WIP FIRE for instance or to be adapted in a Free-Running multi-tasking framework(202).

2/ We believe the first obstacle for EAT imaging and quantification is the requirement of high spatial resolution due to anatomical constraints. Indeed, EAT is irregularly distributed around the heart with a sinuous curvature and it is separated from its

neighbor paracardial fat only by the ~2mm thick pericardial fascia. Thereby, in cardiac MRI, none of the current approaches for a rapid and automatic quantification are really specific to EAT, measuring only cardiac fat as any bulk fat tissue. In contrary, we tackled the challenge by considering the better visualization of pericardium, which is less affected by partial volume effects, on four-chamber cine and using the temporal information to provide a rapid and automatic quantification of EAT area leveraging deep learning approaches. Our study also confirmed that the peak-systole provided a more robust visualization and segmentation of EAT.

To allow refine MRI of EAT, technical barriers were then to achieve high resolution, 3D and quantitative imaging that is also robust to cardiac/respiratory motion and, preferably, can be resolved during the peak-systole. However, a thorough review on Dixon techniques had shown that most acquisitions were triggered in end-diastolic frame and compromised between resolution and number of echoes times, which directly influenced precision of quantitative biomarkers. To overcome these barriers, we started a collaboration Matthias Stuber's team at CIBM CHUV-UNIL for adapting the Free-Running bSSFP framework towards Free-Running Dixon, enabling high-resolution images, fully cardiac and respiratory resolved. Together, we demonstrated this proof-of concept by achieving high-resolution (1.5 mm^3 isotropic) PDFF and R_2* mapping. Arguably, some might think that the full stack short-axis cine, included in a standard cardiac MRI protocol, would have been a simpler alternative for volumetric quantification, as it has been already used previously(47,48,124). However, with a slice thickness superior to 5 mm, and the partial volume effect in the short axis view that penalizes pericardial fascia visualization, standard cine appeared to us that it was less suitable for a robust high-resolution automatic and precise quantification, even considering super-resolution images processing(203).

In addition to high-spatial resolution necessity, the second obstacle for EAT imaging and characterization is the requirement of precise measurement which is essential for reliability, reproducible research and clinical integration. The difficulty to overcome these combined hurdles had led EAT imaging in cardiac MRI to be only focus on the quantity measurement. Indeed, as mentioned above Dixon methods may obtain high resolution EAT imaging but at the cost of insufficient precision for PDFF and R_2* quantification. In this thesis, we went beyond to achieve a high-spatial resolution precise and reliable PDFF and R_2* quantification of EAT. Several steps were needed to reach this goal :

- the election of the 'optimal' fat-water separation algorithm
- assessment of PDFF and R_2* bias due to fat spectrum model miscalibration
- Identification and exploration of ex-vivo epicardial adipose tissue
- sufficient echo numbers (13) and short echo spacing (ΔTE = 1.07ms) only achievable using bipolar acquisition leveraging by GIRF correction

3/ To leverage these technical barriers, original and innovative tracks were followed throughout this thesis. Indeed, in cardiac MRI, segmentation algorithms of EAT are only based on a single-frame(52,53) whereas our deep learning approach thanks to 3D convolution layer took into account the temporal information which is a key indication used by the expert for manual segmentation.

We also looked at innovative metrics to probe EAT. Indeed, PDFF and R_2* biomarkers have shown to distinguish BAT from WAT(193,194) and could be a measurement to identify color feature of adipose tissue. Then, we focused our research to permit a precise measurement of those parameters. Instead of selecting a random state of the art fat-water algorithm which would have been sufficient to obtain those quantitative maps, we conducted a standardized benchmark of those methods, which have not been done since a decade, to elect the most precise and reliable approach. We went further by assessing the influence of the choice of multi-peak fat spectrum inherent to fat-water model on PDFF and R_2* quantification.

Even with the optimal fat/water separation algorithm and the most adapted fat spectrum model, Dixon-MRI acquisition and reconstruction still have to be optimized to tackle the challenge of cardiac and respiratory motion, rapid phase accrual between fat and water. Only high-spatial resolution bipolar Free-Running Dixon framework overcome those technical barriers. Using an innovative trajectory correction based on gradient impulse response function (GIRF), bipolar Free-Running cardiac Dixon has proved to provide reliable and precise PDFF and R_2* quantification.

We also began to explore in-vivo fatty acid composition of EAT as possible new metrics for EAT analysis by providing a Free-Running bipolar acquisition with possibly a sufficient number of echoes (13) and short enough echo spacing (ΔTE = 1.07ms) as FAC imaging has been already done in similar conditions (36,59,188,204).

New emerging biomarkers could complete the evaluation of EAT in terms of adipocyte size using diffusion weighted MRS(172) or microstructure with intermolecular multiple quantum coherences(205,206).

To conclude, MRI EAT quantitative imaging represents a real potential for in-vivo characterization of the physio-pathological processes induced by EAT in cardiovascular diseases and offers the possibility to assess EAT as a therapeutic target. Indeed, the non-invasive evaluation of EAT browning (12) after therapeutic or nutritional intervention is an emerging topic of research.

Bibliography

1. Shirani J, Berezowski K, Roberts WC. Quantitative measurement of normal and excessive (cor adiposum) subepicardial adipose tissue, its clinical significance, and its effect on electrocardiographic QRS voltage. Am J Cardiol. 1995 Aug;76(5):414–8.
2. Corradi D, Maestri R, Callegari S, Pastori P, Goldoni M, Luong TV, et al. The ventricular epicardial fat is related to the myocardial mass in normal, ischemic and hypertrophic hearts. Cardiovasc Pathol. 2004 Nov;13(6):313–6.
3. Rabkin SW. Epicardial fat: properties, function and relationship to obesity. Obes Rev. 2007 May;8(3):253–61.
4. Marchington JM, Mattacks CA, Pond CM. Adipose tissue in the mammalian heart and pericardium: Structure, foetal development and biochemical properties. Comp Biochem Physiol Part B Comp Biochem. 1989 Jan;94(2):225–32.
5. Marchington JM, Pond CM. Site-specific properties of pericardial and epicardial adipose tissue: the effects of insulin and high-fat feeding on lipogenesis and the incorporation of fatty acids in vitro. Int J Obes. 1990 Dec;14(12):1013–22.
6. Prati F. Eccentric atherosclerotic plaques with positive remodelling have a pericardial distribution: a permissive role of epicardial fat? A three-dimensional intravascular ultrasound study of left anterior descending artery lesions. Eur Heart J. 2003 Feb;24(4):329–36.
7. Sacks HS, Fain JN, Holman B, Cheema P, Chary A, Parks F, et al. Uncoupling Protein-1 and Related Messenger Ribonucleic Acids in Human Epicardial and Other Adipose Tissues: Epicardial Fat Functioning as Brown Fat. J Clin Endocrinol Metab. 2009 Sep 1;94(9):3611–5.
8. Antonopoulos AS, Antoniades C. The role of epicardial adipose tissue in cardiac biology: classic concepts and emerging roles. J Physiol. 2017 15;595(12):3907–17.
9. Coelho M, Oliveira T, Fernandes R. State of the art paper Biochemistry of adipose tissue: an endocrine organ. Arch Med Sci. 2013;2:191–200.
10. Nedergaard J, Golozoubova V, Matthias A, Asadi A, Jacobsson A, Cannon B. UCP1: the only protein able to mediate adaptive non-shivering thermogenesis and metabolic inefficiency. Biochim Biophys Acta BBA - Bioenerg. 2001 Mar;1504(1):82–106.

11. Pfeifer A, Hoffmann LS. Brown, Beige, and White: The New Color Code of Fat and Its Pharmacological Implications. Annu Rev Pharmacol Toxicol. 2015 Jan 6;55(1):207–27.
12. Doukbi E, Soghomonian A, Sengenès C, Ahmed S, Ancel P, Dutour A, et al. Browning Epicardial Adipose Tissue: Friend or Foe? Cells. 2022 Mar 14;11(6):991.
13. Langheim S, Dreas L, Veschini L, Maisano F, Foglieni C, Ferrarello S, et al. Increased expression and secretion of resistin in epicardial adipose tissue of patients with acute coronary syndrome. Am J Physiol-Heart Circ Physiol. 2010 Mar;298(3):H746–53.
14. Dutour A, Achard V, Sell H, Naour N, Collart F, Gaborit B, et al. Secretory Type II Phospholipase A2 Is Produced and Secreted by Epicardial Adipose Tissue and Overexpressed in Patients with Coronary Artery Disease. J Clin Endocrinol Metab. 2010 Feb 1;95(2):963–7.
15. Thanassoulis G, Massaro JM, O'Donnell CJ, Hoffmann U, Levy D, Ellinor PT, et al. Pericardial Fat Is Associated With Prevalent Atrial Fibrillation: The Framingham Heart Study. Circ Arrhythm Electrophysiol. 2010 Aug;3(4):345–50.
16. Al Chekakie MO, Welles CC, Metoyer R, Ibrahim A, Shapira AR, Cytron J, et al. Pericardial Fat Is Independently Associated With Human Atrial Fibrillation. J Am Coll Cardiol. 2010 Aug;56(10):784–8.
17. Butcovan D, Mocanu V, Timofte DV, Costan VV, Danila R, Veselin AP, et al. Macrophage Accumulation and Angiogenesis in Epicardial Adipose Tissue in Cardiac Patients with or without Chronic Heart Failure. Appl Sci. 2020 Aug 25;10(17):5871.
18. Gaborit B, Sengenes C, Ancel P, Jacquier A, Dutour A. Role of Epicardial Adipose Tissue in Health and Disease: A Matter of Fat? In: Terjung R, editor. Comprehensive Physiology [Internet]. Hoboken, NJ, USA: John Wiley & Sons, Inc.; 2017 [cited 2021 Jan 12]. p. 1051–82. Available from: http://doi.wiley.com/10.1002/cphy.c160034
19. Cheng KH, Chu CS, Lee KT, Lin TH, Hsieh CC, Chiu CC, et al. Adipocytokines and proinflammatory mediators from abdominal and epicardial adipose tissue in patients with coronary artery disease. Int J Obes. 2008 Feb;32(2):268–74.
20. Venteclef N, Guglielmi V, Balse E, Gaborit B, Cotillard A, Atassi F, et al. Human epicardial adipose tissue induces fibrosis of the atrial myocardium through the secretion of adipo-fibrokines. Eur Heart J. 2015 Apr 1;36(13):795–805.

21. Suffee N, Moore-Morris T, Jagla B, Mougenot N, Dilanian G, Berthet M, et al. Reactivation of the Epicardium at the Origin of Myocardial Fibro-Fatty Infiltration During the Atrial Cardiomyopathy. Circ Res. 2020 May 8;126(10):1330–42.
22. Salgado-Somoza A, Teijeira-Fernández E, Rubio J, Couso E, González-Juanatey JR, Eiras S. Coronary artery disease is associated with higher epicardial Retinol-binding protein 4 (RBP4) and lower glucose transporter (GLUT) 4 levels in epicardial and subcutaneous adipose tissue: Epicardial fat and RBP4. Clin Endocrinol (Oxf). 2012 Jan;76(1):51–8.
23. Bambace C, Sepe A, Zoico E, Telesca M, Olioso D, Venturi S, et al. Inflammatory profile in subcutaneous and epicardial adipose tissue in men with and without diabetes. Heart Vessels. 2014 Jan;29(1):42–8.
24. Mahajan R, Nelson A, Pathak RK, Middeldorp ME, Wong CX, Twomey DJ, et al. Electroanatomical Remodeling of the Atria in Obesity. JACC Clin Electrophysiol. 2018 Dec;4(12):1529–40.
25. Jing L, Binkley CM, Suever JD, Umasankar N, Haggerty CM, Rich J, et al. Cardiac remodeling and dysfunction in childhood obesity: a cardiovascular magnetic resonance study. J Cardiovasc Magn Reson. 2016 Dec;18(1):28.
26. Mahabadi AA, Berg MH, Lehmann N, Kälsch H, Bauer M, Kara K, et al. Association of Epicardial Fat With Cardiovascular Risk Factors and Incident Myocardial Infarction in the General Population. J Am Coll Cardiol. 2013 Apr;61(13):1388–95.
27. Hodson L, Skeaff CM, Fielding BA. Fatty acid composition of adipose tissue and blood in humans and its use as a biomarker of dietary intake. Prog Lipid Res. 2008 Sep;47(5):348–80.
28. Hamilton G, Yokoo T, Bydder M, Cruite I, Schroeder ME, Sirlin CB, et al. In vivo characterization of the liver fat ^{1}H MR spectrum. NMR Biomed. 2011 Aug;24(7):784–90.
29. Pezeshkian M, Noori M, Najjarpour-Jabbari H, Abolfathi A, Darabi M, Darabi M, et al. Fatty acid composition of epicardial and subcutaneous human adipose tissue. Metab Syndr Relat Disord. 2009 Apr;7(2):125–31.
30. Pezeshkian M, Mahtabipour MR. Epicardial and subcutaneous adipose tissue Fatty acids profiles in diabetic and non-diabetic patients candidate for coronary artery bypass graft. BioImpacts BI. 2013;3(2):83–9.

31. Field CJ, Angel A, Clandinin MT. Relationship of diet to the fatty acid composition of human adipose tissue structural and stored lipids. Am J Clin Nutr. 1985 Dec;42(6):1206–20.
32. Garaulet M, Hernandez-Morante JJ, Lujan J, Tebar FJ, Zamora S. Relationship between fat cell size and number and fatty acid composition in adipose tissue from different fat depots in overweight/obese humans. Int J Obes. 2006 Jun;30(6):899–905.
33. Lundbom J, Hakkarainen A, Fielding B, Söderlund S, Westerbacka J, Taskinen MR, et al. Characterizing human adipose tissue lipids by long echo time 1H-MRS in vivo at 1.5 Tesla: validation by gas chromatography. NMR Biomed. 2010 Jun;23(5):466–72.
34. Hjelmgaard K, Eschen RB, Schmidt EB, Andreasen JJ, Lundbye-Christensen S. Fatty Acid Composition in Various Types of Cardiac Adipose Tissues and Its Relation to the Fatty Acid Content of Atrial Tissue. Nutrients. 2018 Oct 15;10(10).
35. Nemeth A, Segrestin B, Leporq B, Seyssel K, Faraz K, Sauvinet V, et al. 3D Chemical Shift-Encoded MRI for Volume and Composition Quantification of Abdominal Adipose Tissue During an Overfeeding Protocol in Healthy Volunteers. J Magn Reson Imaging. 2019 Jun;49(6):1587–99.
36. Trinh L, Peterson P, Leander P, Brorson H, Månsson S. In vivo comparison of MRI-based and MRS-based quantification of adipose tissue fatty acid composition against gas chromatography. Magn Reson Med. 2020 Nov;84(5):2484–94.
37. Lundbom J, Hakkarainen A, Söderlund S, Westerbacka J, Lundbom N, Taskinen MR. Long-TE 1H MRS suggests that liver fat is more saturated than subcutaneous and visceral fat. NMR Biomed. 2011 Apr;24(3):238–45.
38. Ren J, Dimitrov I, Sherry AD, Malloy CR. Composition of adipose tissue and marrow fat in humans by ^{1}H NMR at 7 Tesla. J Lipid Res. 2008 Sep;49(9):2055–62.
39. Peterson P, Månsson S. Simultaneous quantification of fat content and fatty acid composition using MR imaging. Magn Reson Med. 2013 Mar 1;69(3):688–97.
40. Hamilton G, Schlein AN, Middleton MS, Hooker CA, Wolfson T, Gamst AC, et al. In vivo triglyceride composition of abdominal adipose tissue measured by ^{1}H MRS at 3T: ^{1}H MRS Adipose Triglyceride Composition. J Magn Reson Imaging. 2017 May;45(5):1455–63.
41. Nemeth A, Segrestin B, Leporq B, Coum A, Gambarota G, Seyssel K, et al. Comparison of MRI-derived vs. traditional estimations of fatty acid composition from MR spectroscopy signals. NMR Biomed. 2018 Sep;31(9):e3991.

42. Ouwerkerk R, Hamimi A, Matta J, Abd-Elmoniem KZ, Eary JF, Abdul Sater Z, et al. Proton MR Spectroscopy Measurements of White and Brown Adipose Tissue in Healthy Humans: Relaxation Parameters and Unsaturated Fatty Acids. Radiology. 2021 May;299(2):396–406.
43. Hakumäki JM, Kauppinen RA. 1H NMR visible lipids in the life and death of cells. Trends Biochem Sci. 2000 Aug;25(8):357–62.
44. Strobel K, van den Hoff J, Pietzsch J. Localized proton magnetic resonance spectroscopy of lipids in adipose tissue at high spatial resolution in mice in vivo. J Lipid Res. 2008 Feb;49(2):473–80.
45. Bastiaansen JAM, Piccini D, Di Sopra L, Roy CW, Heerfordt J, Edelman RR, et al. Natively fat-suppressed 5D whole-heart MRI with a radial free-running fast-interrupted steady-state (FISS) sequence at 1.5T and 3T. Magn Reson Med. 2020 Jan;83(1):45–55.
46. Gaborit B, Kober F, Jacquier A, Moro PJ, Cuisset T, Boullu S, et al. Assessment of epicardial fat volume and myocardial triglyceride content in severely obese subjects: relationship to metabolic profile, cardiac function and visceral fat. Int J Obes 2005. 2012 Mar;36(3):422–30.
47. Gaborit B, Jacquier A, Kober F, Abdesselam I, Cuisset T, Boullu-Ciocca S, et al. Effects of Bariatric Surgery on Cardiac Ectopic Fat. J Am Coll Cardiol. 2012 Oct;60(15):1381–9.
48. Gaborit B, Ancel P, Abdullah AE, Maurice F, Abdesselam I, Calen A, et al. Effect of empagliflozin on ectopic fat stores and myocardial energetics in type 2 diabetes: the EMPACEF study. Cardiovasc Diabetol. 2021 Dec;20(1):57.
49. Nyman K, Granér M, Pentikäinen MO, Lundbom J, Hakkarainen A, Sirén R, et al. Cardiac steatosis and left ventricular function in men with metabolic syndrome. J Cardiovasc Magn Reson. 2013;15(1):103.
50. Nakanishi K, Fukuda S, Tanaka A, Otsuka K, Taguchi H, Shimada K. Relationships Between Periventricular Epicardial Adipose Tissue Accumulation, Coronary Microcirculation, and Left Ventricular Diastolic Dysfunction. Can J Cardiol. 2017 Nov;33(11):1489–97.
51. Rado SD, Lorbeer R, Gatidis S, Machann J, Storz C, Nikolaou K, et al. MRI-based assessment and characterization of epicardial and paracardial fat depots in the

context of impaired glucose metabolism and subclinical left-ventricular alterations. Br J Radiol. 2019 Apr;92(1096):20180562.

52. Cristobal-Huerta A, Torrado-Carvajal A, Malpica N, Luaces M, Hernandez-Tamames JA. Automated quantification of epicardial adipose tissue in cardiac magnetic resonance imaging. In: 2015 37th Annual International Conference of the IEEE Engineering in Medicine and Biology Society (EMBC) [Internet]. Milan: IEEE; 2015 [cited 2021 Jan 15]. p. 7308–11. Available from: http://ieeexplore.ieee.org/document/7320079/
53. Fulton MR, Givan AH, Fernandez-del-Valle M, Klingensmith JD. Segmentation of epicardial adipose tissue in cardiac MRI using deep learning. In: Gimi BS, Krol A, editors. Medical Imaging 2020: Biomedical Applications in Molecular, Structural, and Functional Imaging [Internet]. Houston, United States: SPIE; 2020 [cited 2021 Jan 15]. p. 25. Available from: https://www.spiedigitallibrary.org/conference-proceedings-of-spie/11317/2550013/Segmentation-of-epicardial-adipose-tissue-in-cardiac-MRI-using-deep/10.1117/12.2550013.full
54. Bley TA, Wieben O, François CJ, Brittain JH, Reeder SB. Fat and water magnetic resonance imaging: Fat and Water MRI. J Magn Reson Imaging. 2010 Jan;31(1):4–18.
55. Dixon WT. Simple proton spectroscopic imaging. Radiology. 1984 Oct;153(1):189–94.
56. Reeder SB, Pineda AR, Wen Z, Shimakawa A, Yu H, Brittain JH, et al. Iterative decomposition of water and fat with echo asymmetry and least-squares estimation (IDEAL): Application with fast spin-echo imaging. Magn Reson Med. 2005 Sep;54(3):636–44.
57. Leporq B, Ratiney H, Pilleul F, Beuf O. Liver fat volume fraction quantification with fat and water T1 and T2* estimation and accounting for NMR multiple components in patients with chronic liver disease at 1.5 and 3.0 T. Eur Radiol. 2013 Aug;23(8):2175–86.
58. Zhong X, Nickel MD, Kannengiesser SAR, Dale BM, Kiefer B, Bashir MR. Liver fat quantification using a multi-step adaptive fitting approach with multi-echo GRE imaging. Magn Reson Med. 2014 Nov;72(5):1353–65.
59. Leporq B, Lambert SA, Ronot M, Vilgrain V, Van Beers BE. Quantification of the triglyceride fatty acid composition with 3.0 T MRI. NMR Biomed. 2014 Oct;27(10):1211–21.

60. Leporq B, Lambert SA, Ronot M, Boucenna I, Colinart P, Cauchy F, et al. Hepatic fat fraction and visceral adipose tissue fatty acid composition in mice: Quantification with 7.0T MRI: Quantification of Fat and Fatty Acid Composition in Mice with 7.0T MRI. Magn Reson Med. 2016 Aug;76(2):510–8.
61. Triay Bagur A, Hutton C, Irving B, Gyngell ML, Robson MD, Brady M. Magnitude-intrinsic water–fat ambiguity can be resolved with multipeak fat modeling and a multipoint search method. Magn Reson Med. 2019 Jul;82(1):460–75.
62. Romu T, Dahlström N, Leinhard OD, Borga M. Robust water fat separated dual-echo MRI by phase-sensitive reconstruction: Robust Water Fat Separated Dual-Echo MRI by Phase-Sensitive Reconstruction. Magn Reson Med. 2017 Sep;78(3):1208–16.
63. Siracusano G, La Corte A, Gaeta M, Finocchio G. A data-oriented self-calibration and robust chemical-shift encoding by using clusterization (OSCAR): Theory, optimization and clinical validation in neuromuscular disorders. Magn Reson Imaging. 2018 Jan;45:84–96.
64. Yu H, Reeder SB, Shimakawa A, McKenzie CA, Brittain JH. Robust multipoint water-fat separation using fat likelihood analysis: FLAME: Fat Likelihood Analysis for Multiecho Signals. Magn Reson Med. 2012 Apr;67(4):1065–76.
65. Soliman AS, Yuan J, Vigen KK, White JA, Peters TM, McKenzie CA. Max-IDEAL: A max-flow based approach for IDEAL water/fat separation: A Max-Flow Approach for IDEAL Water/Fat Separation. Magn Reson Med. 2014 Aug;72(2):510–21.
66. Liu J, Drangova M. Method for B0 off-resonance mapping by non-iterative correction of phase-errors (B0-NICE): B0 Mapping with Multiecho Data. Magn Reson Med. 2015 Oct;74(4):1177–88.
67. Wang D, Zwart NR, Li Z, Schär M, Pipe JG. Analytical three-point Dixon method: With applications for spiral water–fat imaging. Magn Reson Med. 2016 Feb;75(2):627–38.
68. Zhang T, Chen Y, Bao S, Alley MT, Pauly JM, Hargreaves BA, et al. Resolving phase ambiguity in dual-echo dixon imaging using a projected power method. Magn Reson Med. 2017 May;77(5):2066–76.
69. Cheng C, Zou C, Liang C, Liu X, Zheng H. Fat-water separation using a region-growing algorithm with self-feeding phasor estimation: Self-Feeding Phasor Estimation for Fat-Water Separation. Magn Reson Med. 2017 Jun;77(6):2390–401.
70. Bydder M, Ghodrati V, Gao Y, Robson MD, Yang Y, Hu P. Constraints in estimating the proton density fat fraction. Magn Reson Imaging. 2020 Feb;66:1–8.

71. Peng H, Zou C, Cheng C, Tie C, Qiao Y, Wan Q, et al. Fat-water separation based on Transition REgion Extraction (TREE). Magn Reson Med. 2019 Jul;82(1):436–48.
72. Berglund J, Kullberg J. Three-dimensional water/fat separation and T2* estimation based on whole-image optimization-Application in breathhold liver imaging at 1.5 T. Magn Reson Med. 2012 Jun;67(6):1684–93.
73. Cui C, Wu X, Newell JD, Jacob M. Fat water decomposition using globally optimal surface estimation (GOOSE) algorithm. Magn Reson Med. 2015 Mar;73(3):1289–99.
74. Stinson EG, Trzasko JD, Fletcher JG, Riederer SJ. Dual echo Dixon imaging with a constrained phase signal model and graph cuts reconstruction. Magn Reson Med. 2017 Dec;78(6):2203–15.
75. Berglund J, Skorpil M. Multi-scale graph-cut algorithm for efficient water-fat separation: Multi-Scale Graph-Cut Water/Fat Separation. Magn Reson Med. 2017 Sep;78(3):941–9.
76. Diefenbach MN, Ruschke S, Eggers H, Meineke J, Rummeny EJ, Karampinos DC. Improving chemical shift encoding-based water-fat separation based on a detailed consideration of magnetic field contributions. Magn Reson Med. 2018 Sep;80(3):990–1004.
77. Cui C, Shah A, Wu X, Jacob M. A rapid 3D fat–water decomposition method using globally optimal surface estimation (R-GOOSE). Magn Reson Med. 2018 Apr;79(4):2401–7.
78. Andersson J, Ahlström H, Kullberg J. Water-fat separation incorporating spatial smoothing is robust to noise. Magn Reson Imaging. 2018 Jul;50:78–83.
79. Boehm C, Diefenbach MN, Makowski MR, Karampinos DC. Improved body quantitative susceptibility mapping by using a variable-layer single-min-cut graph-cut for field-mapping. Magn Reson Med. 2021 Mar;85(3):1697–712.
80. Cho J, Park H. Robust water–fat separation for multi-echo gradient-recalled echo sequence using convolutional neural network. Magn Reson Med. 2019 Jul;82(1):476–84.
81. Andersson J, Ahlström H, Kullberg J. Separation of water and fat signal in whole-body gradient echo scans using convolutional neural networks. Magn Reson Med. 2019 Sep;82(3):1177–86.

82. Goldfarb JW, Craft J, Cao JJ. Water-fat separation and parameter mapping in cardiac MRI via deep learning with a convolutional neural network: MR Water-Fat Separation. J Magn Reson Imaging. 2019 Aug;50(2):655–65.
83. Jafari R, Spincemaille P, Zhang J, Nguyen TD, Luo X, Cho J, et al. Deep neural network for water/fat separation: Supervised training, unsupervised training, and no training. Magn Reson Med. 2021 Apr;85(4):2263–77.
84. Liu K, Li X, Li Z, Chen Y, Xiong H, Chen F, et al. Robust water–fat separation based on deep learning model exploring multi-echo nature of mGRE. Magn Reson Med. 2021 May;85(5):2828–41.
85. Hernando D, Liang ZP, Kellman P. Chemical shift-based water/fat separation: A comparison of signal models: Comparison of Water/Fat Signal Models. Magn Reson Med. 2010 Sep;64(3):811–22.
86. Hu HH, Börnert P, Hernando D, Kellman P, Ma J, Reeder S, et al. ISMRM workshop on fat-water separation: Insights, applications and progress in MRI. Magn Reson Med. 2012 Aug;68(2):378–88.
87. Tsao J, Jiang Y. Hierarchical IDEAL: Fast, robust, and multiresolution separation of multiple chemical species from multiple echo times. Magn Reson Med. 2013 Jul;70(1):155–9.
88. Lamy J. mrsd: a toolkit to generate MR sequence diagrams [Internet]. Github. [cited 2022 Jun 19]. Available from: https://github.com/lamyj/mrsd
89. Yu H, Shimakawa A, McKenzie CA, Lu W, Reeder SB, Hinks RS, et al. Phase and amplitude correction for multi-echo water-fat separation with bipolar acquisitions. J Magn Reson Imaging. 2010 May;31(5):1264–71.
90. Shahzad R, Bos D, Metz C, Rossi A, Kirişli H, van der Lugt A, et al. Automatic quantification of epicardial fat volume on non-enhanced cardiac CT scans using a multi-atlas segmentation approach: Automatic epicardial fat volume quantification. Med Phys. 2013 Aug 12;40(9):091910.
91. Ding X, Terzopoulos D, Diaz-Zamudio M, Berman DS, Slomka PJ, Dey D. Automated pericardium delineation and epicardial fat volume quantification from noncontrast CT: Automated epicardial fat volume quantification from noncontrast CT. Med Phys. 2015 Aug 5;42(9):5015–26.

92. Commandeur F, Goeller M, Betancur J, Cadet S, Doris M, Chen X, et al. Deep Learning for Quantification of Epicardial and Thoracic Adipose Tissue From Non-Contrast CT. IEEE Trans Med Imaging. 2018 Aug;37(8):1835–46.
93. Commandeur F, Goeller M, Razipour A, Cadet S, Hell MM, Kwiecinski J, et al. Fully Automated CT Quantification of Epicardial Adipose Tissue by Deep Learning: A Multicenter Study. Radiol Artif Intell. 2019 Nov 1;1(6):e190045.
94. Zhang Q, Zhou J, Zhang B, Jia W, Wu E. Automatic Epicardial Fat Segmentation and Quantification of CT Scans Using Dual U-Nets With a Morphological Processing Layer. IEEE Access. 2020;8:128032–41.
95. Ronneberger O, Fischer P, Brox T. U-Net: Convolutional Networks for Biomedical Image Segmentation. In: Navab N, Hornegger J, Wells WM, Frangi AF, editors. Medical Image Computing and Computer-Assisted Intervention – MICCAI 2015 [Internet]. Cham: Springer International Publishing; 2015 [cited 2020 Aug 26]. p. 234–41. (Lecture Notes in Computer Science; vol. 9351). Available from: http://link.springer.com/10.1007/978-3-319-24574-4_28
96. Long J, Shelhamer E, Darrell T. Fully convolutional networks for semantic segmentation. In: 2015 IEEE Conference on Computer Vision and Pattern Recognition (CVPR) [Internet]. Boston, MA, USA: IEEE; 2015 [cited 2022 Jun 22]. p. 3431–40. Available from: http://ieeexplore.ieee.org/document/7298965/
97. Szegedy C, Wei Liu, Yangqing Jia, Sermanet P, Reed S, Anguelov D, et al. Going deeper with convolutions. In: 2015 IEEE Conference on Computer Vision and Pattern Recognition (CVPR) [Internet]. Boston, MA, USA: IEEE; 2015 [cited 2022 Jun 22]. p. 1–9. Available from: http://ieeexplore.ieee.org/document/7298594/
98. Kingma DP, Ba J. Adam: A Method for Stochastic Optimization. ArXiv14126980 Cs [Internet]. 2017 Jan 29 [cited 2020 Nov 23]; Available from: http://arxiv.org/abs/1412.6980
99. Rumelhart DE, Hinton GE, Williams RJ. Learning representations by back-propagating errors. Nature. 1986 Oct;323(6088):533–6.
100. Shi X, Chen Z, Wang H, Yeung DY, Wong W kin, Woo W chun. Convolutional LSTM Network: A Machine Learning Approach for Precipitation Nowcasting. ArXiv150604214 Cs [Internet]. 2015 Sep 19 [cited 2021 Nov 22]; Available from: http://arxiv.org/abs/1506.04214

101. Sudlow C, Gallacher J, Allen N, Beral V, Burton P, Danesh J, et al. UK Biobank: An Open Access Resource for Identifying the Causes of a Wide Range of Complex Diseases of Middle and Old Age. PLOS Med. 2015 Mar 31;12(3):e1001779.
102. Pérez-García F, Sparks R, Ourselin S. TorchIO: A Python library for efficient loading, preprocessing, augmentation and patch-based sampling of medical images in deep learning. Comput Methods Programs Biomed. 2021 Sep;208:106236.
103. Fournel J, Bartoli A, Bendahan D, Guye M, Bernard M, Rauseo E, et al. Medical image segmentation automatic quality control: A multi-dimensional approach. Med Image Anal. 2021 Dec;74:102213.
104. Mahabadi AA, Lehmann N, Kälsch H, Robens T, Bauer M, Dykun I, et al. Association of Epicardial Adipose Tissue With Progression of Coronary Artery Calcification Is More Pronounced in the Early Phase of Atherosclerosis. JACC Cardiovasc Imaging. 2014 Sep;7(9):909–16.
105. Ding J, Hsu FC, Harris TB, Liu Y, Kritchevsky SB, Szklo M, et al. The association of pericardial fat with incident coronary heart disease: the Multi-Ethnic Study of Atherosclerosis (MESA). Am J Clin Nutr. 2009 Sep 1;90(3):499–504.
106. Iacobellis G. Epicardial and Pericardial Fat: Close, but Very Different. Obesity. 2009 Apr;17(4):625–625.
107. Nakanishi K, Fukuda S, Tanaka A, Otsuka K, Jissho S, Taguchi H, et al. Persistent epicardial adipose tissue accumulation is associated with coronary plaque vulnerability and future acute coronary syndrome in non-obese subjects with coronary artery disease. Atherosclerosis. 2014 Nov;237(1):353–60.
108. Rosito GA, Massaro JM, Hoffmann U, Ruberg FL, Mahabadi AA, Vasan RS, et al. Pericardial Fat, Visceral Abdominal Fat, Cardiovascular Disease Risk Factors, and Vascular Calcification in a Community-Based Sample: The Framingham Heart Study. Circulation. 2008 Feb 5;117(5):605–13.
109. Dabbah S, Komarov H, Marmor A, Assy N. Epicardial fat, rather than pericardial fat, is independently associated with diastolic filling in subjects without apparent heart disease. Nutr Metab Cardiovasc Dis. 2014 Aug;24(8):877–82.
110. Iacobellis G, Secchi F, Capitanio G, Basilico S, Schiaffino S, Boveri S, et al. Epicardial Fat Inflammation in severe COVID-19. Obesity. 2020 Aug 30;oby.23019.

111. Grodecki K, Lin A, Razipour A, Cadet S, McElhinney PA, Chan C, et al. Epicardial adipose tissue is associated with extent of pneumonia and adverse outcomes in patients with COVID-19. Metabolism. 2021 Feb;115:154436.
112. Mahabadi AA, Rassaf T. Thoracic adipose tissue density as a novel marker of increased cardiovascular risk. Atherosclerosis. 2018 Dec;279:91–2.
113. Iacobellis G, Assael F, Ribaudo MC, Zappaterreno A, Alessi G, Di Mario U, et al. Epicardial Fat from Echocardiography: A New Method for Visceral Adipose Tissue Prediction. Obes Res. 2003 Feb;11(2):304–10.
114. Dey D, Suzuki Y, Suzuki S, Ohba M, Slomka PJ, Polk D, et al. Automated Quantitation of Pericardiac Fat From Noncontrast CT: Invest Radiol. 2008 Feb;43(2):145–53.
115. Nichols JH, Samy B, Nasir K, Fox CS, Schulze PC, Bamberg F, et al. Volumetric measurement of pericardial adipose tissue from contrast-enhanced coronary computed tomography angiography: A reproducibility study. J Cardiovasc Comput Tomogr. 2008 Sep;2(5):288–95.
116. Kramer CM, Barkhausen J, Bucciarelli-Ducci C, Flamm SD, Kim RJ, Nagel E. Standardized cardiovascular magnetic resonance imaging (CMR) protocols: 2020 update. J Cardiovasc Magn Reson. 2020 Dec;22(1):17.
117. Flüchter S, Haghi D, Dinter D, Heberlein W, Kühl HP, Neff W, et al. Volumetric Assessment of Epicardial Adipose Tissue With Cardiovascular Magnetic Resonance Imaging*. Obesity. 2007 Apr;15(4):870–8.
118. Homsi R, Meier-Schroers M, Gieseke J, Dabir D, Luetkens JA, Kuetting DL, et al. 3D-Dixon MRI based volumetry of peri- and epicardial fat. Int J Cardiovasc Imaging. 2016 Feb;32(2):291–9.
119. Henningsson M, Brundin M, Scheffel T, Edin C, Viola F, Carlhäll CJ. Quantification of epicardial fat using 3D cine Dixon MRI. BMC Med Imaging. 2020 Dec;20(1):80.
120. Chetrit M, Xu B, Kwon DH, Ramchand J, Rodriguez RE, Tan CD, et al. Imaging-Guided Therapies for Pericardial Diseases. JACC Cardiovasc Imaging. 2020 Jun;13(6):1422–37.
121. Bard A, Raisi-Estabragh Z, Ardissino M, Lee AM, Pugliese F, Dey D, et al. Automated Quality-Controlled Cardiovascular Magnetic Resonance Pericardial Fat Quantification Using a Convolutional Neural Network in the UK Biobank. Front Cardiovasc Med. 2021 Jul 7;8:677574.

122. Granér M, Siren R, Nyman K, Lundbom J, Hakkarainen A, Pentikäinen MO, et al. Cardiac Steatosis Associates With Visceral Obesity in Nondiabetic Obese Men. J Clin Endocrinol Metab. 2013 Mar 1;98(3):1189–97.
123. Perseghin G, Lattuada G, De Cobelli F, Esposito A, Belloni E, Ntali G, et al. Increased mediastinal fat and impaired left ventricular energy metabolism in young men with newly found fatty liver. Hepatology. 2007 Oct 22;47(1):51–8.
124. Gaborit B, Kober F, Jacquier A, Moro PJ, Flavian A, Quilici J, et al. Epicardial Fat Volume Is Associated With Coronary Microvascular Response in Healthy Subjects: A Pilot Study. Obesity. 2012 Jun;20(6):1200–5.
125. Dutour A, Abdesselam I, Ancel P, Kober F, Mrad G, Darmon P, et al. Exenatide decreases liver fat content and epicardial adipose tissue in patients with obesity and type 2 diabetes: a prospective randomized clinical trial using magnetic resonance imaging and spectroscopy. Diabetes Obes Metab. 2016 Sep;18(9):882–91.
126. Tustison NJ, Avants BB, Cook PA, Yuanjie Zheng, Egan A, Yushkevich PA, et al. N4ITK: Improved N3 Bias Correction. IEEE Trans Med Imaging. 2010 Jun;29(6):1310–20.
127. McCarthy, Paul. FSLeyes v.0.31 [Internet]. 2019 [cited 2020 Oct 2]. Available from: https://doi.org/10.5281/zenodo.3403671
128. Ogier A, Sdika M, Foure A, Le Troter A, Bendahan D. Individual muscle segmentation in MR images: A 3D propagation through 2D non-linear registration approaches. In: 2017 39th Annual International Conference of the IEEE Engineering in Medicine and Biology Society (EMBC) [Internet]. Seogwipo: IEEE; 2017 [cited 2021 Mar 8]. p. 317–20. Available from: https://ieeexplore.ieee.org/document/8036826/
129. Bai W, Sinclair M, Tarroni G, Oktay O, Rajchl M, Vaillant G, et al. Automated cardiovascular magnetic resonance image analysis with fully convolutional networks. J Cardiovasc Magn Reson. 2018 Dec;20(1):65.
130. Zheng Q, Delingette H, Duchateau N, Ayache N. 3-D Consistent and Robust Segmentation of Cardiac Images by Deep Learning With Spatial Propagation. IEEE Trans Med Imaging. 2018 Sep;37(9):2137–48.
131. Baumgartner CF, Koch LM, Pollefeys M, Konukoglu E. An Exploration of 2D and 3D Deep Learning Techniques for Cardiac MR Image Segmentation. ArXiv170904496 Cs [Internet]. 2017 Oct 10 [cited 2020 Jun 29]; Available from: http://arxiv.org/abs/1709.04496

132. Isensee F, Jaeger PF, Full PM, Wolf I, Engelhardt S, Maier-Hein KH. Automatic Cardiac Disease Assessment on cine-MRI via Time-Series Segmentation and Domain Specific Features. In: Pop M, Sermesant M, Jodoin PM, Lalande A, Zhuang X, Yang G, et al., editors. Statistical Atlases and Computational Models of the Heart ACDC and MMWHS Challenges [Internet]. Cham: Springer International Publishing; 2018 [cited 2020 Oct 2]. p. 120–9. (Lecture Notes in Computer Science; vol. 10663). Available from: http://link.springer.com/10.1007/978-3-319-75541-0_13
133. Bai W. ukbb_cardiac [Internet]. [cited 2020 Dec 1]. Available from: https://github.com/baiwenjia/ukbb_cardiac
134. R Core Team. R: A Language and Environment for Statistical Computing [Internet]. Vienna, Austria: R Foundation for Statistical Computing; 2020. Available from: https://www.R-project.org/
135. Foldyna B, Zeleznik R, Eslami P, Mayrhofer T, Ferencik M, Bittner DO, et al. Epicardial Adipose Tissue in Patients With Stable Chest Pain. JACC Cardiovasc Imaging. 2020 Oct;13(10):2273–5.
136. Chaitanya K, Karani N, Baumgartner CF, Becker A, Donati O, Konukoglu E. Semi-supervised and Task-Driven Data Augmentation. In: Chung ACS, Gee JC, Yushkevich PA, Bao S, editors. Information Processing in Medical Imaging [Internet]. Cham: Springer International Publishing; 2019 [cited 2021 Sep 20]. p. 29–41. (Lecture Notes in Computer Science; vol. 11492). Available from: http://link.springer.com/10.1007/978-3-030-20351-1_3
137. Bull RK, Edwards PD, Dixon AK. CT dimensions of the normal pericardium. Br J Radiol. 1998 Sep;71(849):923–5.
138. Bogaert J, Francone M. Cardiovascular magnetic resonance in pericardial diseases. J Cardiovasc Magn Reson. 2009 Dec;11(1):14.
139. Poudel RPK, Lamata P, Montana G. Recurrent Fully Convolutional Neural Networks for Multi-slice MRI Cardiac Segmentation. ArXiv160803974 Cs Stat [Internet]. 2016 Aug 13 [cited 2020 Nov 27]; Available from: http://arxiv.org/abs/1608.03974
140. Huttenlocher DP, Klanderman GA, Rucklidge WJ. Comparing images using the Hausdorff distance. IEEE Trans Pattern Anal Mach Intell. 1993 Sep;15(9):850–63.
141. Reeder SB, Hu HH, Sirlin CB. Proton density fat-fraction: A standardized mr-based biomarker of tissue fat concentration. J Magn Reson Imaging. 2012 Nov;36(5):1011–4.

142. Starekova J, Reeder SB. Liver fat quantification: where do we stand? Abdom Radiol. 2020 Nov;45(11):3386–99.
143. Bainbridge A, Bray TJP, Sengupta R, Hall-Craggs MA. Practical Approaches to Bone Marrow Fat Fraction Quantification Across Magnetic Resonance Imaging Platforms. J Magn Reson Imaging. 2020 Jul;52(1):298–306.
144. Department of Radiology, Hacettepe University School of Medicine, Ankara, Turkey, Idilman IS. Proton density fat fraction: magnetic resonance imaging applications beyond the liver. Diagn Interv Radiol. 2022 Jan 28;28(1):83–91.
145. Wood JC. Guidelines for quantifying iron overload. Hematology. 2014 Dec 5;2014(1):210–5.
146. Triadyaksa P, Oudkerk M, Sijens PE. Cardiac T_2 * mapping: Techniques and clinical applications. J Magn Reson Imaging. 2020 Nov;52(5):1340–51.
147. Baker M. 1,500 scientists lift the lid on reproducibility. Nature. 2016 May 26;533(7604):452–4.
148. Sullivan DC, Obuchowski NA, Kessler LG, Raunig DL, Gatsonis C, Huang EP, et al. Metrology Standards for Quantitative Imaging Biomarkers. Radiology. 2015 Dec;277(3):813–25.
149. Weingärtner S, Desmond KL, Obuchowski NA, Baessler B, Zhang Y, Biondetti E, et al. Development, validation, qualification, and dissemination of quantitative MR methods: Overview and recommendations by the ISMRM quantitative MR study group. Magn Reson Med. 2021 Nov 26;mrm.29084.
150. Hernando D, Sharma SD, Aliyari Ghasabeh M, Alvis BD, Arora SS, Hamilton G, et al. Multisite, multivendor validation of the accuracy and reproducibility of proton-density fat-fraction quantification at 1.5T and 3T using a fat-water phantom: Proton-Density Fat-Fraction Quantification at 1.5T and 3T. Magn Reson Med. 2017 Apr;77(4):1516–24.
151. Diefenbach MN, Liu C, Karampinos DC. Generalized parameter estimation in multi-echo gradient-echo-based chemical species separation. Quant Imaging Med Surg. 2020 Mar;10(3):554–67.
152. Hernando D, Kellman P, Haldar JP, Liang ZP. Robust water/fat separation in the presence of large field inhomogeneities using a graph cut algorithm. Magn Reson Med. 2009;NA-NA.

153. Matakos A, Balter JM, Cao Y. A Robust Method for Estimating B0 Inhomogeneity Field in the Liver by Mitigating Fat Signals and Phase-Wrapping. Tomography. 2017 Jun 1;3(2):79–88.
154. Pineda AR, Reeder SB, Wen Z, Pelc NJ. Cramér-Rao bounds for three-point decomposition of water and fat. Magn Reson Med. 2005 Sep;54(3):625–35.
155. Yu H, Shimakawa A, McKenzie CA, Brodsky E, Brittain JH, Reeder SB. Multiecho water-fat separation and simultaneous R2* estimation with multifrequency fat spectrum modeling. Magn Reson Med. 2008 Nov;60(5):1122–34.
156. Reeder SB, Robson PM, Yu H, Shimakawa A, Hines CD, McKenzie CA, et al. Quantification of hepatic steatosis with MRI: The effects of accurate fat spectral modeling. J Magn Reson Imaging. 2009 Jun;29(6):1332–9.
157. Wang X, Hernando D, Reeder SB. Sensitivity of chemical shift-encoded fat quantification to calibration of fat MR spectrum. Magn Reson Med. 2016 Feb;75(2):845–51.
158. Peterson P, Trinh L, Månsson S. Quantitative ^{1}H MRI and MRS of fatty acid composition. Magn Reson Med. 2021 Jan;85(1):49–67.
159. Hines CDG, Yu H, Shimakawa A, McKenzie CA, Brittain JH, Reeder SB. T_1 independent, T_2* corrected MRI with accurate spectral modeling for quantification of fat: Validation in a fat-water-SPIO phantom. J Magn Reson Imaging. 2009 Nov;30(5):1215–22.
160. Bush EC, Gifford A, Coolbaugh CL, Towse TF, Damon BM, Welch EB. Fat-Water Phantoms for Magnetic Resonance Imaging Validation: A Flexible and Scalable Protocol. J Vis Exp. 2018 Sep 7;(139):57704.
161. Clarke WT, Stagg CJ, Jbabdi S. FSL-MRS: An end-to-end spectroscopy analysis package. Magn Reson Med. 2021 Jun;85(6):2950–64.
162. Breuer FA, Blaimer M, Mueller MF, Seiberlich N, Heidemann RM, Griswold MA, et al. Controlled aliasing in volumetric parallel imaging (2D CAIPIRINHA). Magn Reson Med. 2006 Mar;55(3):549–56.
163. Reeder SB, Bice EK, Yu H, Hernando D, Pineda AR. On the performance of T2* correction methods for quantification of hepatic fat content. Magn Reson Med. 2012 Feb;67(2):389–404.

164. Sharma SD, Artz NS, Hernando D, Horng DE, Reeder SB. Improving chemical shift encoded water–fat separation using object-based information of the magnetic field inhomogeneity. Magn Reson Med. 2015;73(2):597–604.
165. Chan KS, Marques JP. SEPIA—Susceptibility mapping pipeline tool for phase images. NeuroImage. 2021 Feb 15;227:117611.
166. Roussel T, Le Fur Y, Guye M, Viout P, Ranjeva J, Callot V. Respiratory-triggered quantitative MR spectroscopy of the human cervical spinal cord at 7 T. Magn Reson Med. 2022 Jun;87(6):2600–12.
167. Smith SA, Levante TO, Meier BH, Ernst RR. Computer Simulations in Magnetic Resonance. An Object-Oriented Programming Approach. J Magn Reson A. 1994 Jan;106(1):75–105.
168. Bydder M, Girard O, Hamilton G. Mapping the double bonds in triglycerides. Magn Reson Imaging. 2011 Oct;29(8):1041–6.
169. Nicolay K, Braun KPJ, Graaf RA de, Dijkhuizen RM, Kruiskamp MJ. Diffusion NMR spectroscopy. NMR Biomed. 2001 Apr;14(2):94–111.
170. Ronen I, Valette J. Diffusion-Weighted Magnetic Resonance Spectroscopy. In: Harris RK, Wasylishen RL, editors. eMagRes [Internet]. Chichester, UK: John Wiley & Sons, Ltd; 2015 [cited 2022 Jun 12]. p. 733–50. Available from: http://doi.wiley.com/10.1002/9780470034590.emrstm1471
171. Verma SK, Nagashima K, Yaligar J, Michael N, Lee SS, Xianfeng T, et al. Differentiating brown and white adipose tissues by high-resolution diffusion NMR spectroscopy. J Lipid Res. 2017 Jan;58(1):289–98.
172. Weidlich D, Honecker J, Gmach O, Wu M, Burgkart R, Ruschke S, et al. Measuring large lipid droplet sizes by probing restricted lipid diffusion effects with diffusion-weighted MRS at 3T. Magn Reson Med. 2019 Jun;81(6):3427–39.
173. Lee NG, Ramasawmy R, Lim Y, Campbell-Washburn AE, Nayak KS. MaxGIRF : Image reconstruction incorporating concomitant field and gradient impulse response function effects. Magn Reson Med. 2022 Apr 21;mrm.29232.
174. Kellman P, Hernando D, Shah S, Zuehlsdorff S, Jerecic R, Mancini C, et al. Multiecho dixon fat and water separation method for detecting fibrofatty infiltration in the myocardium: Fibrofatty Infiltration in Myocardium. Magn Reson Med. 2009 Jan;61(1):215–21.

175. Messroghli DR, Moon JC, Ferreira VM, Grosse-Wortmann L, He T, Kellman P, et al. Clinical recommendations for cardiovascular magnetic resonance mapping of T1, T2, T2* and extracellular volume: A consensus statement by the Society for Cardiovascular Magnetic Resonance (SCMR) endorsed by the European Association for Cardiovascular Imaging (EACVI). J Cardiovasc Magn Reson. 2017 Dec;19(1):75.
176. Leiner T, Bogaert J, Friedrich MG, Mohiaddin R, Muthurangu V, Myerson S, et al. SCMR Position Paper (2020) on clinical indications for cardiovascular magnetic resonance. J Cardiovasc Magn Reson. 2020 Dec;22(1):76.
177. Zia MI, Ghugre NR, Connelly KA, Strauss BH, Sparkes JD, Dick AJ, et al. Characterizing Myocardial Edema and Hemorrhage Using Quantitative T2 and T2* Mapping at Multiple Time Intervals Post ST-Segment Elevation Myocardial Infarction. Circ Cardiovasc Imaging. 2012 Sep;5(5):566–72.
178. Anderson L. Cardiovascular T2-star (T2*) magnetic resonance for the early diagnosis of myocardial iron overload. Eur Heart J. 2001 Dec 1;22(23):2171–9.
179. Börnert P, Koken P, Nehrke K, Eggers H, Ostendorf P. Water/fat-resolved whole-heart Dixon coronary MRA: An initial comparison: Whole-Heart Dixon Coronary MRA. Magn Reson Med. 2014 Jan;71(1):156–63.
180. Rajiah P, Bolen MA. Cardiovascular MR Imaging at 3 T: Opportunities, Challenges, and Solutions. RadioGraphics. 2014 Oct;34(6):1612–35.
181. Munoz C, Cruz G, Neji R, Botnar RM, Prieto C. Motion corrected water/fat whole-heart coronary MR angiography with 100% respiratory efficiency. Magn Reson Med. 2019 Aug;82(2):732–42.
182. Di Sopra L, Piccini D, Coppo S, Stuber M, Yerly J. An automated approach to fully self-gated free-running cardiac and respiratory motion-resolved 5D whole-heart MRI. Magn Reson Med. 2019 Dec;82(6):2118–32.
183. Ma LE, Yerly J, Piccini D, Di Sopra L, Roy CW, Carr JC, et al. 5D Flow MRI: A Fully Self-gated, Free-running Framework for Cardiac and Respiratory Motion–resolved 3D Hemodynamics. Radiol Cardiothorac Imaging. 2020 Dec 1;2(6):e200219.
184. Secchi F, Asteria C, Monti CB, Malavazos AE, Capra D, Alì M, et al. Quantification of epicardial adipose tissue in obese patients using an open-bore MR scanner. Eur Radiol Exp. 2022 Dec;6(1):25.

185. Addy NO, Wu HH, Nishimura DG. Simple method for MR gradient system characterization and k-space trajectory estimation. Magn Reson Med. 2012 Jul;68(1):120–9.
186. Vannesjo SJ, Haeberlin M, Kasper L, Pavan M, Wilm BJ, Barmet C, et al. Gradient system characterization by impulse response measurements with a dynamic field camera: Gradient System Characterization with a Dynamic Field Camera. Magn Reson Med. 2013 Feb;69(2):583–93.
187. Kronthaler S, Rahmer J, Börnert P, Makowski MR, Schwaiger BJ, Gersing AS, et al. Trajectory correction based on the gradient impulse response function improves high-resolution UTE imaging of the musculoskeletal system. Magn Reson Med. 2021 Apr;85(4):2001–15.
188. Schneider M, Janas G, Lugauer F, Hoppe E, Nickel D, Dale BM, et al. Accurate fatty acid composition estimation of adipose tissue in the abdomen based on bipolar multi-echo MRI. Magn Reson Med. 2019 Apr;81(4):2330–46.
189. Campbell-Washburn AE, Xue H, Lederman RJ, Faranesh AZ, Hansen MS. Real-time distortion correction of spiral and echo planar images using the gradient system impulse response function: Real-Time Distortion Correction Framework for Fast Imaging. Magn Reson Med. 2016 Jun;75(6):2278–85.
190. Berzl,M.,Pfeuffer,J. et al. Improved spiral trajectory correction using the gradient impulse response function (GIRF). ISMRM 2017,933. 933rd ed.
191. Duval T, Rapacchi S. imtool3D v3.0 [Internet]. [cited 2022 Jan 11]. Available from: https://github.com/tanguyduval/imtool3D_td
192. Dietrich S, Aigner CS, Mayer J, Kolbitsch C, Schulz-Menger J, Schaeffter T, et al. Motion-compensated fat-water imaging for 3D cardiac MRI at ultra-high fields. Magn Reson Med. 2022 Jun;87(6):2621–36.
193. Hu HH, Hines CDG, Smith DL, Reeder SB. Variations in T(2)* and fat content of murine brown and white adipose tissues by chemical-shift MRI. Magn Reson Imaging. 2012 Apr;30(3):323–9.
194. Franz D, Diefenbach MN, Treibel F, Weidlich D, Syväri J, Ruschke S, et al. Differentiating supraclavicular from gluteal adipose tissue based on simultaneous PDFF and T_2 * mapping using a 20-echo gradient-echo acquisition: PDFF and T_2 * Mapping Using 20-Echo GRE. J Magn Reson Imaging. 2019 Aug;50(2):424–34.

195. Echols J, Shah S, Epstein F. Fatty Acid Composition MRI of Human Epicardial Adipose Tissue. In London, UK; 2022. p. Poster. (2022 ISMRM-ESMRMB & ISMRT 31st Annual Meeting, 07-12 May).
196. Tsaftaris SA, Zhou X, Tang R, Li D, Dharmakumar R. Detecting Myocardial Ischemia at Rest With Cardiac Phase–Resolved Blood Oxygen Level–Dependent Cardiovascular Magnetic Resonance. Circ Cardiovasc Imaging. 2013 Mar;6(2):311–9.
197. Wen Y, Nguyen TD, Liu Z, Spincemaille P, Zhou D, Dimov A, et al. Cardiac quantitative susceptibility mapping (QSM) for heart chamber oxygenation: Cardiac QSM for Heart Chamber Oxygenation. Magn Reson Med. 2018 Mar;79(3):1545–52.
198. Daudé P, Ancel P, Confort Gouny S, Jacquier A, Kober F, Dutour A, et al. Deep-Learning Segmentation of Epicardial Adipose Tissue Using Four-Chamber Cardiac Magnetic Resonance Imaging. Diagnostics. 2022 Jan 6;12(1):126.
199. Li J, Chang S, Liu T, Jiang H, Dong F, Pei M, et al. Phase-corrected bipolar gradients in multi-echo gradient-echo sequences for quantitative susceptibility mapping. Magn Reson Mater Phys Biol Med. 2015 Aug;28(4):347–55.
200. Sutton BP, Noll DC, Fessler JA. Fast, iterative image reconstruction for MRI in the presence of field inhomogeneities. IEEE Trans Med Imaging. 2003 Feb;22(2):178–88.
201. Hernando D, Vigen KK, Shimakawa A, Reeder SB. R 2* mapping in the presence of macroscopic B0 field variations. Magn Reson Med. 2012 Sep;68(3):830–40.
202. Christodoulou AG, Shaw JL, Nguyen C, Yang Q, Xie Y, Wang N, et al. Magnetic resonance multitasking for motion-resolved quantitative cardiovascular imaging. Nat Biomed Eng. 2018 Apr;2(4):215–26.
203. Oktay O, Bai W, Lee M, Guerrero R, Kamnitsas K, Caballero J, et al. Multi-input Cardiac Image Super-Resolution Using Convolutional Neural Networks. In: Ourselin S, Joskowicz L, Sabuncu MR, Unal G, Wells W, editors. Medical Image Computing and Computer-Assisted Intervention - MICCAI 2016 [Internet]. Cham: Springer International Publishing; 2016 [cited 2022 Jul 6]. p. 246–54. (Lecture Notes in Computer Science; vol. 9902). Available from: https://link.springer.com/10.1007/978-3-319-46726-9_29

204. Berglund J, Ahlström H, Kullberg J. Model-based mapping of fat unsaturation and chain length by chemical shift imaging-phantom validation and in vivo feasibility. Magn Reson Med. 2012 Dec;68(6):1815–27.
205. Branca RT, Warren WS. In vivo brown adipose tissue detection and characterization using water-lipid intermolecular zero-quantum coherences. Magn Reson Med. 2011 Feb;65(2):313–9.
206. Bao J, Cui X, Cai S, Zhong J, Cai C, Chen Z. Brown adipose tissue mapping in rats with combined intermolecular double-quantum coherence and Dixon water-fat MRI: MAPPING BAT AT THE CELLULAR LEVEL. NMR Biomed. 2013 Dec;26(12):1663–71.

List of Abbreviations and Symbols

4-Ch cine	four-chamber cine
BAT	Brown Adipose Tissue
BeAT	Beige Adipose Tissue
BMI	Body Mass Index
bSSFP	balanced steady-state free precession
BW	Bandwidth
CAD	Coronary Artery Disease
CAIPIRINHA	Controlled Aliasing in Parallel Imaging Results in Higher Acceleration
CCT	Cardiac Computed Tomography
CHD	Coronary Heart Disease
cl	Chain length
CMR	Cardiovascular Magnetic Resonance
CNN	Convolutional Neural Network
COVID	Coronavirus disease
CRLB	Cramér-Rao Lower Bounds
CSE	Chemical Shift Encoded
CSI	Chemical Shift Imaging
CVD	Cardiovascular disease
ΔTE	echo time spacing
DSC	Dice similarity coefficient
EAT	Epicardial Adipose Tissue
EAT+PAT	pericardial adipose tissue
ECG	Electrocardiogram
FA	Flip Angle
FAC	Fatty Acid Composition
FBG	Fasting Plasma Glucose
FCN	Fully Convolutional Networks
FFA	Free Fatty Acids
FID	Free Induction Decay
FOV	Field Of View
GC	Gas chromatography
GFRF	Gradient Frequency Response Function
GIRF	Gradient Impulse Response Function
GRAPPA	GeneRalized Autocalibrating Partial Parallel Acquisition
GRE	Gradient echo
HV	Heart ventricles
IDEAL	Iterative Decomposition of water and fat with Echo Asymmetry and Least square estimation

IL	Interleukin
LOA	Limits Of Agreement
ConvLSTM	Convolutional Long Short-Term Memory
ReLU	Rectified Linear Unit
LV	Left Ventricle
MITI	Mission for Transversal and Interdisciplinary Initiatives
MR	Magnetic Resonance
MRI	Magnetic Resonance Imaging
MRS	Magnetic Resonance Spectroscopy
MSD	Mean Surface Distance
MUFA	Monounsaturated fatty acid
NAFLD	Non Alcoholic Fatty Liver Disease
ndb	Number of double bonds
NLSQ	Non Linear Least Squares
nmidb	Number of methylene-interrupted double bonds
NMR	Nuclear Magnetic Resonance
NTE	Number of echo times
OVS	Outer Volume Suppression
PAT	Paracardial adipose tissue
PDFF	Proton Density Fat Fraction
PPV	Positive predicted value
PRESS	Point-resolved spectroscopy
PUFA	Polyunsaturated fatty acid
QFA	Relative abundance of each fatty acid
QIBA	Quantitative Imaging Biomarkers Assessment group
QSM	Quantitative Susceptibility Mapping
RF	Radiofrequency
ROI	Region-of-interest
RSE	Absolute relative surface error
RV	Right Ventricle
SAT	Subcutaneous adipose tissue
SD	Standard deviation
SFA	Saturated fatty acid
SNR	Signal noise ratio
STEAM	Stimulated echo acquisition mode
STIR	Short-TI Inversion Recovery
SVD	Single value decomposition
TE	Echo time
TI	Inversion time
TM	Mixing time
TNF	Tumor necrosis factors
TR	Repetition time
T2D	Type 2 diabetes
UCP-1	Uncoupling protein-1

UFA	Unsaturated fatty acid
VAT	Visceral adipose tissue
VOI	Voxel of interest
WAT	White adipose tissue
WHO	World Health Organization
WOS	Web of science

List of Figures

Figure 0-1 Résultats représentatifs de la segmentation pour chaque population définie par quartile d'EAT. Les flèches blanches indiquent les divergences entre les segmentations manuelle et automatique. 16

Figure 0-2 : Comparaison du biais PDFF (A) et R_2*. (B) de chaque algorithme sur des volumes synthétiques d'IRM-CSE avec NTE=7 et SNR=100. GOOSE et B0-NICE (en carré rouge) n'ont pas été étudiés plus avant en raison de résultats très biaisés. 20

Figure 0-3: Exemples de spectres obtenus du même sujet avec la graisse sous-cutanée thoracique et la graisse épicardique. Les courbes noires représentent les spectres acquis avec la séquence STEAM. Le courbe d'ajustement (rouge) a été conçu pour quantifier l'eau (4,7 ppm) et le modèle des lipides. Le signal résiduel (gris) permet d'évaluer l'adéquation du modèle. 23

Figure 0-4 Au cours des différents états respiratoires, les cartes quantitatives de PDFF et R_2*, B_0 hors-résonance en vue coronale résultant de la correction monopolaire, bipolaire avec ou sans GIRF. La ligne blanche pointillée représente le niveau du diaphragme à l'état d'expiration. 26

Figure 1-1 : The anatomy of epicardial adipose tissue (EAT). Epicardial fat, or EAT, is the only adipose tissue that has access to the myocardium. Since it is a metabolically active organ, it can deposit deleterious hormones in the coronary arteries. The separation between epicardial and paracardial fat is very subtle. 30

Figure 1-2 : The classic concepts about the role of epicardial adipose tissue in heart physiology. Adapted from (8) 31

Figure 1-3 : Type of adipose tissue. Epicardial adipose tissue is deemed beige fat, with its characteristics varying between a predominant white or brown fat. 32

Figure 1-4 : Schematic example of a triglyceride molecule structure. From top to bottom, it consists of a palmitic acid (16:0), an oleic acid (18:1n-9) and an α-linoleic acid (18:3n-3). Its triglyceride model profile is ndb=4, nmidb=2 and cl=17.33. Extracted from Wikipedia 34

Figure 1-5 : Schematic illustration of a triglyceride molecule (top) and the corresponding MR spectrum (bottom). The letters refer to the peak assignments in **Table 1-2**..... 36

Figure 1-6 : Epicardial fat imaging during a standard cardiac exam. On short-axis (A.), four chamber (B.),and two-chamber (C.) cine sequence. EAT appears as hyperintense whereas on Short-TI Inversion Recovery (STIR), it is hided..... 40

Figure 1-7 : Epicardial fat imaging during a cardiac cycle using short-axis cine (A) or four-chamber cine (B)...... 41

Figure 1-8: Multi-echo gradient echo (GRE) MRI sequence diagram using monopolar(A) and bipolar (B) readout gradients. RF: radiofrequency, α: flip angle, G_{slice} : slice select gradient, G_{phase} : phase encoding gradient, $G_{readout}$: frequency encoding gradient, TE_1: first echo time, ΔTE: echo time spacing, TR: repetition time. MR sequence diagrams were generated using the mrsd toolkit(88)..... 46

Figure 1-9 : Architecture of the Fully Convolutional Network U-Net. 48

Figure 1-10: Outline of the different functional layers present in the U-net : the convolutional layer with activation function (A), the down-sampling layer(B), the up-sampling layer (C). Highlighted regions show the calculation process of each layer. 49

Figure 2-1.Overview of the study design 55

Figure 2-2. Networks' optimized architecture. The two networks evaluated in this study: U-Net and fully-convolutional network (FCNB) architectures included a first 3D convolution layer to allow multiple cardiac frames as input. Following 2D convolution layers encoded images from 48 features up to 768 features. Eventually, the decoder targeted 3 labels for segmentation in the central input frame: epicardial adipose tissue (EAT), paracardial adipose tissue (PAT) and heart ventricles (HV) 58

Figure 2-3. Comparison of reference total epicardial fat volume and proposed EAT area measured on four-chamber cine. EAT area was measured in end-systolic or end-diastolic frame across the 100 subjects' database. The three cohorts merged for the database were identified by markers color..... 62

Figure 2-4. Representative segmentation results for each population defined by quartile of EAT area. Images were cropped around the heart for visualization. White arrows point out discrepancies between manual and automatic segmentations. As detailed in the methods, only periventricular EAT was segmented..... 65

Figure 2-5. Quartile classification results from EAT area estimated from networks segmentation against classification from manual EAT area. Only segmentations from preferred systolic frames were shown here. 66

Figure 3-1 : Influence of triglyceride parameters (Cl, ndb, nmidb) on synthetic magnitude CSE-MRI signal at PDFF 90% and $T2*$=20 ms at 3T. Synthetic magnitude CSE-MRI were synthesized based on SAT fat spectrum (Cl=17.29, nmidb=0.58, ndb=2.69) with realistic variation of one parameter (A. Cl, B. nmidb, C. ndb) while the others are fixed. 74

Figure 3-2 : PDFF was measured by Fatty-Riot-GC and Hernando-GC over synthetic CSE-MRI volumes with SNR=50 at 3 and 7 echoes. PDFF maps were averaged along repetition axis and separated according to the echo spacing scheme (IDEAL, IN-/OUT-OF-PHASE, MINIMAL). Fat-water swaps were visible at 3T with Fatty-Riot-GC while bias appeared on the PDFF map processed by Hernando-GC due to $B0$ inhomogeneities. With 7 echoes, both algorithms provided more reliable quantitative maps. 85

Figure 3-3 : Comparison of PDFF (A) and $R2*$ (B) bias of each algorithm over synthetic CSE-MRI volumes with NTE=7 and SNR=100. Mean and standard deviation PDFF and $R2*$ bias were averaged along the $B0$ off-resonance and repetition axes and separated (in color) according to the echo spacing schemes. GOOSE and B0-NICE (in red square) where not further investigated due to highly bias results. 86

Figure 3-4 : A. PDFF measurement from in-vitro experiments using MSGCA-A, Fatty-Riot-GC and IDEAL-CE with NTE=3 and NTE=7 and in-/out-of-phase echo spacing. B. Comparison of PDFF bias of each algorithm in phantoms. Mean and standard deviation PDFF bias were averaged along the $B0$ off-resonance and repetition axes and separated according to the echo spacing schemes (in colour) and echo number (in line style). For clarity, only standard deviation of PDFF bias for NTE=7 have been plotted. 88

Figure 3-5 : PDFF and $R2*$ quantification of Fatty-Riot-GC,IDEAL-CE and MSGCA-A over challenging in-vivo datasets at 3T. PDFF overestimation was observed using MSGCA-A and Fatty-Riot-GC as shown by white arrows where fat is not expected inside the bladder or the neck. 89

Figure 3-6 : Influence of fat spectrum models on PDFF and $R2*$ quantification with IDEAL-CE, MSGCA-A : A. Synthetic magnitude CSE-MRI signal at PDFF 100% and $T2*$=20 ms with different spectrum depicted in the literature or acquired for this

study.B. PDFF and $R2*$ bias when synthetic CSE-volume are processed with either the same spectrum (peanut oil) or with the ISMRM challenge one at 3T with 9 echoes and realistic minimal echo-spacing. PDFF, $R2*$ measurement when in vitro experiment (.C) or in in vivo (.D) were processed with peanut oil spectrum at 3T with 9 echoes with a minimal echo spacing scheme and the difference ΔPDFF, $\Delta R2*$ resulted when those data were processed with the ISMRM challenge spectrum. .. 91

Figure 4-1: Examples of spectra obtained on thoracic subcutaneous fat and epicardial fat of the same subject. Black curves represent the spectra acquired using STEAM sequence. The fitting processing (red) was designed to quantify water (4.7 ppm) and the lipids model (**Table 1-2**). Residual signal (grey) enables to evaluate the adequacy of the model. 105

Figure 5-1 : Trajectory correction using system-specific gradient impulse response function (GIRF) : (A) Measurement of the GIRF and the magnitude of its Fourier transform (GFRF) ; (B) K-space trajectory correction pipeline (C) applied for the first four echoes in bipolar mode. (D) Converting distorted gradients into k-space trajectory showed up a mean shift superior to 1 for even echoes. GIRF-corrected trajectory prevents this error at the image reconstruction level. 117

Figure 5-2 : Free-running Dixon-MRI echo times repartition depending on the multi-echo scheme, before and after GIRF correction. Monopolar echo spacing was longer than the fat-water in-phase/out-of-phase delay at 3T. In bipolar mode without correction, strong artifacts appeared on even echo images but after GIRF correction image quality was restored. 120

Figure 5-3 : Comparison of PDFF (A.) and R_2* (B.) bias and absolute error between 8 echoes in monopolar compared to 13 echoes in bipolar over synthetic CSE-MRI volumes with SNR=50 and 10. Mean and standard deviation PDFF and R_2* bias and absolute error were averaged along the $B0$ off-resonance and repetition axes. 121

Figure 5-4: PDFF (A.) and B_0 off-resonance (B.) measurements from in-vitro experiments with monopolar and bipolar with or without GIRF correction. 122

Figure 5-5 : Impact of GIRF correction on free-running bipolar Dixon-MRI on in-vivo data. Artifacted even echoes (2nd echo presented only) are highlighted in red. Radial artifacts were reduced in GIRF-corrected images, corresponding to an almost in-phase image in vivo. 123

Figure 5-6 : Across the different phases of the cardiac, quantitative PDFF and R_2*, B_0 off-resonance maps in axial view resulting from monopolar, bipolar with or without GIRF correction. Inadequate monopolar echo spacing as well as uncorrected bipolar data led to spurious PDFF overestimation with fat-water swaps. 124

Figure 5-7 : Across the different respiratory states, Quantitative PDFF and R_2*, B_0 off-resonance maps in coronal view resulting from monopolar, bipolar with or without GIRF correction. The dotted white line represents the diaphragm level at expiration state. 125

Figure 5-8: PDFF measurements over different regions of interests across the volunteers resulting from bipolar with or without GIRF correction and monopolar echoes. Boxplots showed the consistency of PDFF measurements along cardiac and respiratory cycle. 126

Figure 5-9 : PDFF, R_2*, B_0 off resonance measurements in epicardial and paracardial fat across patients and healthy volunteers. 127

List of Tables

Table 1-1 : Summary of fatty acids composition and triglyceride model parameters of different human adipose tissue estimated using gas chromatography. 35

Table 1-2 : Peak assignments and their corresponding chemical shift and theoretical amplitude expressed using the triglyceride model parameters (number of double bonds (ndb), number of methylene-interrupted double bonds (nmidb) and the chain length (cl)). The hydrogen atoms of interest are written in bold text..... 37

Table 1-3 : Summary of fatty acids composition and triglyceride model parameters of different human adipose tissue estimated using MRS. 38

Table 1-4 : Imaging modalities to quantify epicardial adipose tissue. 39

Table 1-5 : Summary of fat and water signal separation algorithms published since 2012 ISMRM fat-water MRI Workshop. 44

Table 2-1. Study population clinical characteristics. 60

Table 2-2 : Mean values and standard deviations of segmentation results on the test set. 63

Table 2-3. DSC, MSD, RSE metrics evaluated per quartile (Q1-Q4) of EAT area for U-Net and FCNB. 64

Table 3-1 : Summary of evaluated state-of-the-art open-source Fat-Water reconstruction algorithms with specific features, corresponding references and code repository links. 79

Table 4-1 : Mean and standard deviation of T_2 measured for each lipid peak. Only good fitting correlation (r^2 <0.90) are reported..... 107

Table 4-2 : Summary of triglyceride model parameters and fatty acid composition measurements. For stability of the estimation of those parameters, fitting was constrained with cl=17.29 and only A, B, C, D, E and F lipid peaks were considered. 107